# 2

## Vol. 76

# *Hemijska industrija*

### Časopis Saveza hemijskih inženjera Srbije

# *Chemical Industry*
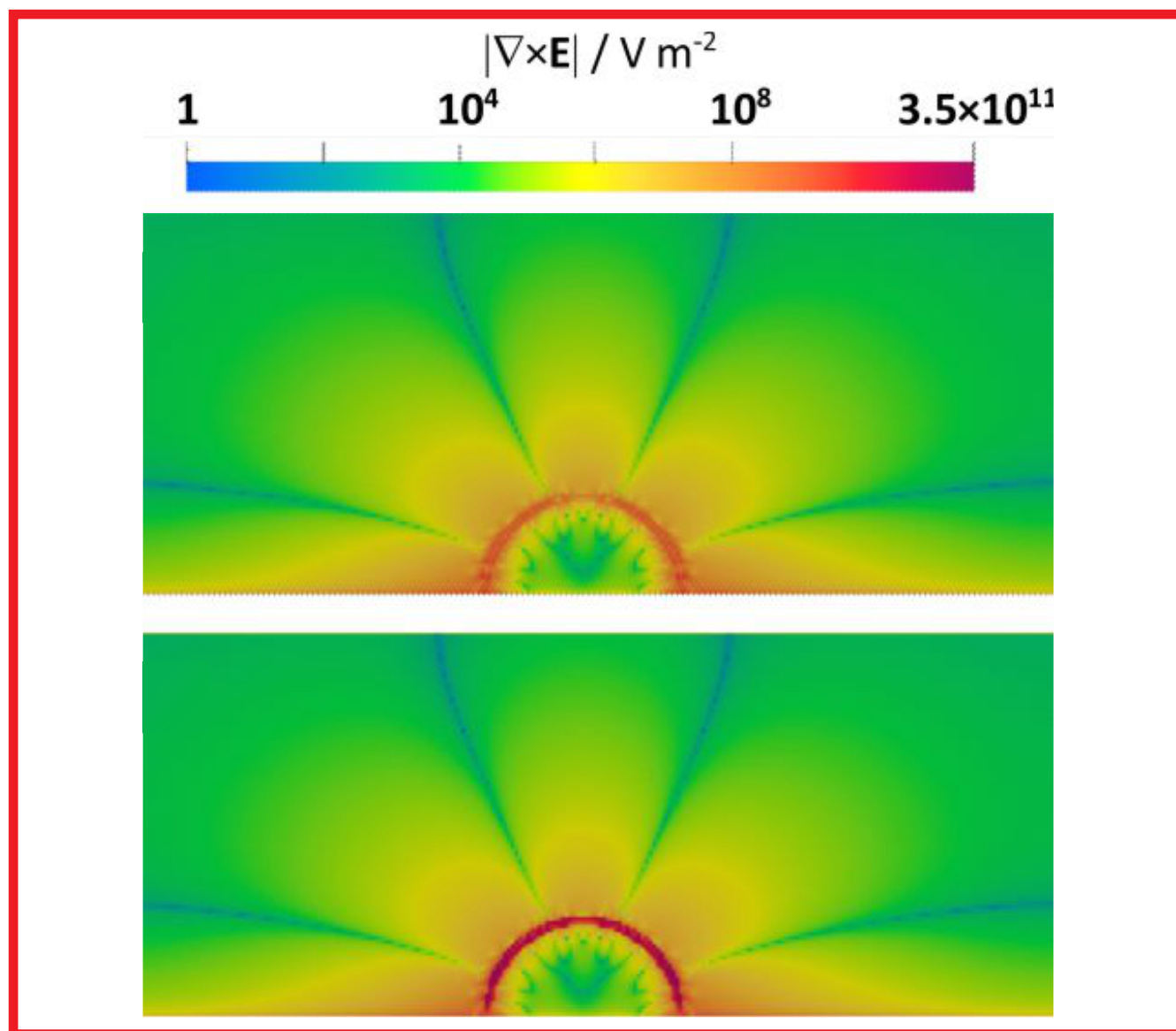
# Aktivnosti Saveza hemijskih inženjera Srbije pomažu:

**MINISTARSTVO PROSVETE,
NAUKE I TEHNOLOŠKOG RAZVOJA
REPUBLIKE SRBIJE**

Tehnološko-metalurški fakultet
Univerziteta u Beogradu, Beograd

Institut za tehnologiju nuklearnih i
drugih mineralnih sirovina, Beograd

Hemijski fakutet Univerziteta u
Beogradu, Beograd

Prirodno-matematički fakultet
Univerziteta u Novom Sadu, Novi Sad

Institut za opštu i fizičku hemiju,
Beograd

Tehnološki fakultet
Univerziteta u Novom Sadu, Novi Sad

NU Institut za hemiju, tehnologiju i metalurgiju
Univerziteta u Beogradu, Beograd

Institut IMS, Beograd

Tehnološki fakultet
Univerziteta u Nišu, Leskovac

Fakultet tehničkih nauka,
Kosovska Mitrovica

## SADRŽAJ/CONTENTS

# Investigation of electrohydrodynamic calculations

**Stefan A. Bošković[1], Aleksandar Karač[2], Slobodan B. Vrhovac[3], Aleksandar Belić[3] and Branko Bugarski[4]**

[1]*Innovation Center of the Faculty of Technology and Metallurgy in Belgrade, Belgrade, Serbia*
[2]*Polytechnic Faculty, University of Zenica, Zenica, Bosnia and Herzegovina*
[3]*University of Belgrade, Institute of Physics Belgrade, Belgrade, Serbia*
[4]*University of Belgrade, Faculty of Technology and Metallurgy, Belgrade, Serbia*

*Abstract*

A perfect dielectric model was incorporated into the OpenFOAM® software and used for investigation and, possibly, improvements of electrohydrodynamic calculations. Two different sets of numerical simulations were analyzed, in which two different fluids were present. The first set was one-dimensional, while in the second, a drop of one fluid was surrounded by the other fluid. It is shown that oscillations and possible artificial generation of a curl of the electric field strength can be observed at applying certain expressions or calculation strategies, which can be thus abandoned. Usage of dynamic meshes, at least those present in the used software, and of limiters for the gradient of the electric field strength can lead to large numerical errors. It is also shown that usage of certain cell face values could improve the results. An electric Courant number was derived by dimensional analysis, and it could be suggested for future calculations. Conclusions made in this paper are expected to be transferable to other more complicated models.

*Keywords:* electrohydrodynamics; OpenFOAM®; perfect dielectric model; electric Courant number.

*Available on-line at the Journal web address: http://www.ache.org.rs/HI/*

## 1. INTRODUCTION

The part of physics that tries to explain motion of a liquid in a presence of an electric field is called electrohydrodynamics (EHD) [1]. The relevant literature, ranging from books (*e.g.* [2]) to scientific articles, can be found for maybe a century or so. There is a decent number of processes that use the electric field to influence fluids [3,4], such as electrocoalescence [5], electrospraying [6] and solvent extraction. Furthermore, for example, the electrospray process is used in mass spectrometry [7], inkjet printing [8], encapsulations [9], *etc*. Despite the fact that both theoretical concepts and practical applications exist, numerical implementations of those theories are still surprisingly limited in the number [10].

In previous experimental [11-15] and theoretical [16] works, the electric field was used in the electrostatic extrusion process for obtaining small diameter particles by affecting the size of droplets that form at the end of a needle. In order to aid the experimental design and improve efficiency and cost-effectiveness of modeling involved processes, it is needed to develop fast, efficient and precise calculation methodologies. The software platform OpenFOAM® (OpenFOAM Foundation, UK) was found to be suitable for this purpose and was used in the present work.

The general approach to EHD calculations is to take into account both polarization of molecules and ohmic conduction in considered fluids [1]. Fluids in which only polarization effects are present are called perfect dielectric fluids [1]. The perfect dielectric model (*e.g.* [17,18]) is suitable as a starting point for numerical calculations because of its simplicity and possibilities for simple adjustments of starting numerical parameters. Other more complicated models can be later added by expanding the present numerical approach. It could be also noted that it is questionable whether fluids should be treated as perfect dielectrics or as perfect conductors (see *e.g.* [19,20]).

The standard set-up for testing quality, stability and efficiency of the perfect dielectric model is to consider a drop of one fluid surrounded by another fluid in presence of electric field causing a deformation of the drop, as in [17]. To address this benchmark calculation, in the present study Computational Fluid Dynamics (CFD), implemented in the OpenFOAM® (version 8) software, was used. This software uses the Finite Volume Method (FVM) [21] and the Volume of Fluid (VoF) method [22], while the interface reconstruction can be carried out by, for example, the Interface Compression (IC) scheme (*e.g.* [23]). This paper reports on the results obtained by expanding an already present solver in the software (termed interFoam) for two immiscible and incompressible fluids and constant temperature, which uses the VoF method.

The paper is organized as follows: first the mathematical model comprising different expressions for the dielectric force and other parameters is presented, after which a set of the most promising expressions is determined, including the one-dimensional set-up and the set-up with a drop. The obtained results are appropriately discussed in order to investigate possible improvements to EHD calculations.

## 2. MATHEMATICAL MODEL

Since the FVM and VoF methods were used in the starting solver, they were also used in the present model. Implementation of the Navier-Stokes equation that is used in the starting solver (*cf.* [24]) was expanded by adding electric forces:

$$\frac{\partial(\rho \mathbf{U})}{\partial t} + \nabla \cdot (\rho \mathbf{U}\mathbf{U}) - \nabla \cdot (\mu \nabla \mathbf{U}) = \rho \mathbf{g} - \nabla p + \mathbf{F}_s + \mathbf{F}_C + \mathbf{F}_{oel} \tag{1}$$

where $\rho$ is the density, $\mathbf{U}$ is the velocity vector, $t$ is the time, $\mu$ is the dynamic viscosity, $\mathbf{g}$ is the gravitational acceleration, $p$ is the pressure, $\mathbf{F}_s$ is the surface tension force, $\mathbf{F}_C$ is the Coulombic force, and $\mathbf{F}_{oel}$ are other electric forces. Implementation of $\mathbf{F}_s$ that was already present in the starting solver was not modified (see *e.g.* [25]). For $\mathbf{F}_{oel}$, either an expression for the dielectric force ($\mathbf{F}_{diel}$), or the sum of expressions for the electrostrictive ($\mathbf{F}_{els}$) and the dielectric force could be used. This corresponds to the Korteweg-Helmholtz approach [26]. For the perfect dielectric model, $\mathbf{F}_C$ is a zero vector, but straightforwardness of transition into other more complicated models can be seen by its inclusion. In this investigation, $\mathbf{F}_{els}$ was neglected. The expansion was carried out in a way so that in a single time step calculation of newly added variables is finished just before calculation of the velocity and the pressure field is started.

Equations that are used for the dielectric and the electrostrictive forces are derived in literature based on the Maxwell stress tensor ($\mathbf{T}_e$) (*e.g.* [19]). The equation that is used for this tensor should be somewhat simplified for the perfect dielectric model (*cf.* [19]; *cf.* [1]):

$$\mathbf{T}_e = -\frac{1}{2}\varepsilon |\mathbf{E}|^2 \mathbf{I} + \frac{1}{2}\rho\left(\frac{\partial \varepsilon}{\partial \rho}\right)_T |\mathbf{E}|^2 \mathbf{I} \tag{2}$$

where $\varepsilon$ is the electric permittivity, $\mathbf{E}$ is the electric field strength, $\mathbf{I}$ is the identity tensor, and $T$ is the temperature. Equations for electric forces are derived in literature by applying the divergence operator to $\mathbf{T}_e$ [1].

### 2. 1. Calculation of the dielectric force

Five expressions were used (separately) for defining the dielectric force.

One of the options was to use the divergence operator built in the software, that is the following equation was used (*cf.* [1]):

$$\mathbf{F}_{diel} = \nabla \cdot \left(-\frac{1}{2}\varepsilon |\mathbf{E}|^2 \mathbf{I}\right) \tag{3}$$

It was also possible to use the equation that is derived after applying the divergence operator (*cf.* [1]), that is the following equation [27,18] (*cf.* [25]):

$$\mathbf{F}_{diel} = -\frac{1}{2}|\mathbf{E}|^2 \nabla \varepsilon \tag{4}$$

A variant of the previous equation that uses cell face values was also investigated:

$$\mathbf{F_{diel}} = R\left( -\frac{1}{2}\left( |\mathbf{E}|^2 \right)_f \left[ \mathbf{n}_f \cdot (\nabla \varepsilon)_f \right] |\mathbf{S}_f| \right) \tag{5}$$

where $R$ is the reconstruction function (see below), **n** is the normal unit vector, **S** is the surface area vector, subscript f denotes the cell face.

As another option, the expression without the electric field strength was used:

$$\mathbf{F_{diel}} = R\left( -\frac{1}{2}\left| \mathbf{n}_f \cdot (\nabla \phi)_f \right|^2 \left[ \mathbf{n}_f \cdot (\nabla \varepsilon)_f \right] |\mathbf{S}_f| \right) \tag{6}$$

where $\phi$ is the electric potential.

The last option was to use the expression that incorporates the electric permittivity (*cf.* [10]):

$$\mathbf{F_{diel}} = \frac{R\left\{ -\frac{1}{2}\left| \varepsilon_f \left( \mathbf{n}_f \cdot (\nabla \phi)_f \right) \right|^2 \left[ \mathbf{n}_f \cdot (\nabla \varepsilon)_f \right] |\mathbf{S}_f| \right\}}{|\varepsilon|^2} \tag{7}$$

## 2. 2. Calculation of the electric field strength

For calculating the electric field strength, at first one of the following equations was used [27]:

$$\mathbf{E} = -\nabla \phi \tag{8}$$

or its variant that uses the cell face values:

$$\mathbf{E} = R\{ -\left[ \mathbf{n}_f \cdot (\nabla \phi)_f \right] |\mathbf{S}_f| \} \tag{9}$$

or the expression that uses the electric permittivity (*cf.* [10]):

$$\mathbf{E} = \frac{R\left\{ -\varepsilon_f \left( \mathbf{n}_f \cdot (\nabla \phi)_f \right) |\mathbf{S}_f| \right\}}{\varepsilon} \tag{10}$$

One equation that could not be directly used is the equation that can be obtained from vector identities (*e.g.* [28]) [1]:

$$\nabla \times \mathbf{E} = 0 \tag{11}$$

However, this equation can be used indirectly, the curl of the electric field strength can be calculated for controlling the simulation quality. If a curl of the electric field strength is noticed, in order to reduce the numerical error, it was assumed that Helmholtz's vector decomposition (*e.g.* [29]) can be used, so that:

$$\mathbf{E} = -\nabla \phi + \nabla \times \mathbf{E_A} \tag{12}$$

where $\mathbf{E_A}$ is the artificial solenoidal component of the electric field strength. $\mathbf{E_A}$ was calculated by using the equation:

$$\nabla^2 \mathbf{E_A} = -\nabla \times \mathbf{E} \tag{13}$$

After calculating $\mathbf{E_A}$, it was possible to optionally correct the electric field strength calculated by Eqs. (8)-(10) in the following way:

$$\mathbf{E} = \mathbf{E_{unc}} - \nabla \times \mathbf{E_A} \tag{14}$$

where $\mathbf{E_{unc}}$ is the uncorrected electric field strength.

## 2. 3. Calculation of the electric potential

The electric potential was calculated by using one of the three following ways. The first was to use the equation [17,18]:

$$\nabla \cdot (\varepsilon \nabla \phi) = 0 \tag{15}$$

The second option was to use the expression that incorporates a possible numerical error in the electric field strength calculation:

$$\nabla \cdot (\varepsilon \nabla \phi) = \nabla \cdot (\varepsilon \nabla \times \mathbf{E_A}) \tag{16}$$

Finally, the third approach was to use the following expression:

$$2\nabla \cdot (\varepsilon \nabla \phi) = -\nabla \cdot (\varepsilon \mathbf{E_{unc}}) \tag{17}$$

$\mathbf{E_{unc}}$ should be important in cases where both Eqs. (14) and (17) are used together because there is a possibility that the former would reduce the improvement that could be obtained by the latter. Eq. (17) incorporates the electric field strength, which should remove one term on the left-hand side and after that leave the numerical error (present in itself) on the right hand side of the Eq. (17).

An optional usage of a recursive loop within the same time step was enabled for cases where either **E** or **E$_A$** would otherwise have to be taken from the previous time step.

## 2. 4. Calculations of the other parameters

The electric permittivity was calculated based on the following equation that is usual for the VoF method and by which newly added fluid properties were handled:

$$\varepsilon = \alpha_1\varepsilon_1 + \alpha_2\varepsilon_2 \tag{18}$$

where $\alpha$ is the volume fraction, while subscripts 1 and 2 denote fluid 1 and fluid 2, respectively.

Expressions used for handling of two different fluids that were already present in the starting solver were not modified.

A reconstruction function is a function that reconstructs a cell center value from face values. The reconstruction function built in the OpenFOAM® software was used (*cf.* [30]):

$$R(z_f) = \left(\Sigma_f \mathbf{S}_f \frac{\mathbf{S}_f}{|\mathbf{S}_f|}\right)^{-1} \cdot \left(\Sigma_f z_f \frac{\mathbf{S}_f}{|\mathbf{S}_f|}\right) \tag{19}$$

where $z$ is a variable.

In the starting solver that is already present in the OpenFOAM® software, length of time steps can be determined by using the Courant number (*Co*) and the interface Courant number (*iCo*). It was decided to add a similar number that could be connected to electrical forces. An equation for the electric Courant number (*Co*$_{el}$) can already be found in literature [31], but different equation can be derived by dimensional analysis from the Alfvén-Courant number (*ACo*) (*cf.* [32]):

$$ACo = \frac{\dfrac{|\mathbf{B}|}{\sqrt{\mu_0\rho}}}{\dfrac{\delta x}{\delta t}} \tag{20}$$

where **B** is the magnetic flux density, $\mu_0$ is the vacuum magnetic permeability, $x$ is an axis. It can be seen that:

$$\left[|\mathbf{B}|\sqrt{\frac{1}{\mu_0\rho}}\right]_{SI} = \frac{m}{s} = \left[|\mathbf{E}|\sqrt{\frac{\varepsilon_0}{\rho}}\right]_{SI} \tag{21}$$

After substituting vacuum by a fluid or fluids, the following expression can be derived:

$$Co_{el} = \frac{|\mathbf{E}|\sqrt{\dfrac{\varepsilon}{\rho}}}{\dfrac{\delta x}{\delta t}} \tag{22}$$

An expression for the interface electric Courant number (*iCo*$_{el}$) can also be derived from the electric Courant number and the interface Courant number.

During simulations, time steps were determined by using: the Courant number, the interface Courant number, the electric Courant number, and the interface electric Courant number.

## 3. RESULTS AND DISCUSSION

A system consisting of two fluids with identical densities and kinematic viscosities ($10^3$ kg m$^{-3}$ and $10^{-6}$ m$^2$ s$^{-1}$, respectively), and different electric permittivities ($2\times10^{-8}$ F m$^{-1}$ and $2\times10^{-9}$ F m$^{-1}$ for fluids 1 and 2, respectively) was considered in calculations. The interfacial tension between fluids was given a value equal to 0.1 N m$^{-1}$. In order to remove the effect, which was not of primary interest, the gravity acceleration was neglected. Fluids are situated between two walls with fixed electric potentials ($\phi_{w1}$ at the wall 1, and $\phi_{w2} = 0$ V at the wall 2).

The IC scheme was used for calculating volume fractions. Meshes were static, unless stated otherwise. The computed results were displayed using ParaView (Kitware, USA) (and paraFoam, OpenFOAM®). The target maximum

value was set to 0.1, unless stated otherwise for the Courant number, the interface Courant number, the electric Courant number, and the interface electric Courant number.

The finally obtained set of expressions consisted of Eq. (1) (the Navier-Stokes equation), Eq. (5) or (6) (for the dielectric force), Eq. (8) (for the electric field strength), Eq. (11) (for checking the curl of the electric field strength), Eq. (15) (for the electric potential), Eq. (18) (for the electric permittivity), Eq. (19) (for the reconstruction function), and Eq. (22) (for the electric Courant number).

### 3. 1. One-dimensional analysis

A simple one-dimensional set-up was used for straightforward and quick comparison of expressions for the dielectric force. The wall 2 was located at the bottom at $x = 0$, the wall 1 was located at the top at $x = 1$ mm, while the domain was discretized with 100 cells. A value equal to 150 V was used for $\phi_{w1}$. Fluid 1 was placed at the bottom half of the geometry, while the fluid 2 was in the upper half. The system was simulated for 0.02 s of its proper time.
The electric field strength and the electric potential, used in the simulation, were given by Eqs. (8) and (15), respectively.

3. 1. 1. Comparison of different expressions for the dielectric force

The pressure near the interface that was obtained by using Eqs. (3)-(7) is presented in Figure 1. As can be seen, all of the investigated expressions for the electric force in which only volume fields are used (*i.e.* Eqs. (3) and (4)) caused oscillations in the calculated pressure, indicating numerical instabilities. On the other side, the expressions that use cell face values and their reconstruction yielded stable results, with the exception of Eq. (7), which is the only one in which the reconstruction is not the final step in the calculation because of the later division. If the result obtained by using Eq. (3) is compared to the results obtained by using the other mentioned expressions, it can be seen that the areas with lower and higher pressures even switched their places. Due to this finding, Eqs. (3), (4), and (7) for the dielectric force calculations were disregarded. Also, expressions that use cell face values and their reconstruction without additional steps can be recommended for calculation of the dielectric force.
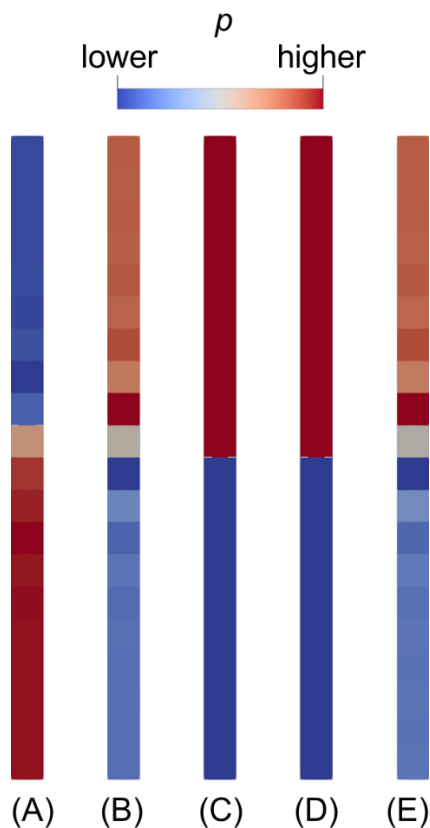


*Figure 1. Pressure near the interface (0.4 to 0.6 mm above the bottom wall) at the end of the simulation using various expressions for the dielectric force: A: Eq. (3); B: Eq. (4); C: Eq. (5); D: Eq. (6); E: Eq. (7). This is a qualitative analysis, boundary values of the pressure were adjusted for every simulation independently.*

### 3. 1. 2. Possible improvements by using the electric Courant number

To demonstrate the influence of the electric Courant number and the interface electric Courant number on the results, the velocity magnitude near the interface when either Eq. (4) or Eq. (6) was used is shown in Figure 2 for two cases:

case 1 – the target maximum value for $Co$, $iCo$, $Co_{el}$, and $iCo_{el}$ was 0.1;

case 2 – the target maximum value for $Co$ and $iCo$ was 0.1, while $Co_{el}$ and $iCo_{el}$ did not influence the time step length.

It could be also worth mentioning that in the second case, the whole simulation was performed in one time step because the simulation end time (*i.e.* 0.02 s) was small enough so not to surpass the target maximum value for $Co$ and $iCo$.

When Eq. (4) was used, the maximum velocity magnitude at the end of the simulation was equal to 0.0690 m s$^{-1}$ for the first case, while it was equal to 0.208 m s$^{-1}$ for the second case. Similarly, when Eq. (6) was used, 7.37×10$^{-11}$ m s$^{-1}$ was obtained for the first case, while 1.52×10$^{-3}$ m s$^{-1}$ was obtained for the second case. The fact that the maximum velocity magnitude was higher when Eq. (4) was used can probably be connected to the previously seen oscillations in the pressure for which it was stated that they indicate numerical instabilities.  Because  it can be said that the velocity magnitude is generally closer to 0 for the case 1, usage of $Co_{el}$ and $iCo_{el}$ for the perfect dielectric model and other models when there is the influence of the electric field could be recommended. Manual time step reduction could also lead to better results. However, it requires several trials, and can lead to a loss of efficiency if overdone.

Certain authors, as [25], use the electric relaxation time for limiting the time step. This approach cannot be used for the perfect dielectric model because the electric conductivity appears in the expression. Also, the Courant number is used for determining the time step instead of the characteristic hydrodynamic time even though it can be found (*e.g.* [1]) and applied to simulations in which there is no electric field, so analogously usage of the electric relaxation time instead of the electric Courant number might not be a suitable option.
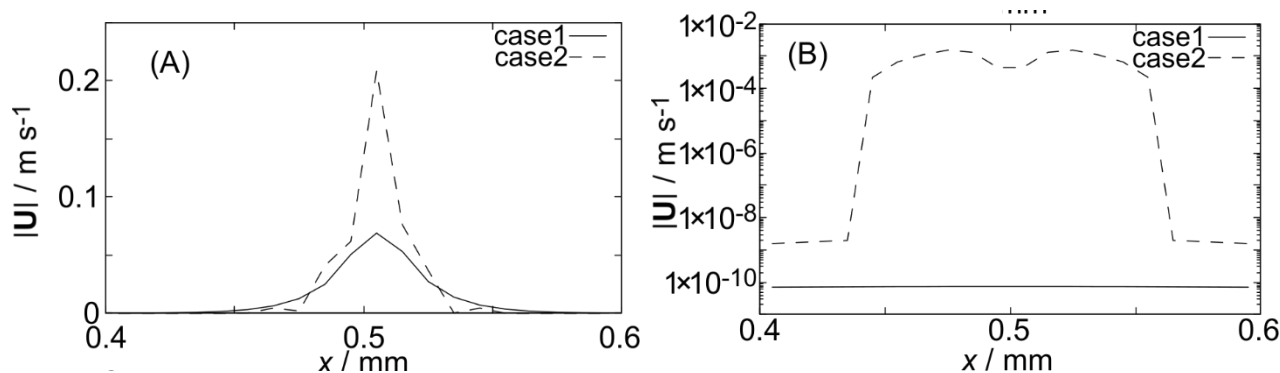


*Figure 2. The velocity magnitude near the interface (0.4 mm to 0.6 mm above the bottom wall) at the end of the simulation for case 1 (with $Co_{el}$ and $iCo_{el}$ influence) and case 2 (without $Co_{el}$ and $iCo_{el}$ influence) when either (A) Eq. (4), or (B) Eq. (6) was used*

### 3. 2. Drop analysis

As the second case study, a drop of fluid 1 submersed in the fluid 2 in an external electric field was analyzed.

For this analysis, axially symmetric geometries were assumed as illustrated in Figure 3. At the center of the symmetry axis was a drop of fluid 1. The starting drop radius ($r_0$) was equal to 2.5×10$^{-5}$ m. On the side opposite to the symmetry axis was the outer surface through which both fluids could exit the geometry, but only the surrounding fluid could enter, and on which the total pressure and the gradient of the electric potential were set to be equal to zero. The distance between the outer surface and the symmetry axis was four times greater than $r_0$. The other two sides were walls at a distance from each other five times greater than the starting drop diameter. Static meshes and the starting mesh for the case in which a dynamic mesh was used consisted of prisms on the symmetry axis and hexahedra. It was decided to use 50 cells per the starting drop diameter. When a dynamic mesh was used, the mesh was refined based on $\alpha_1$, while the refinement level was set to 1 in the OpenFOAM® software.
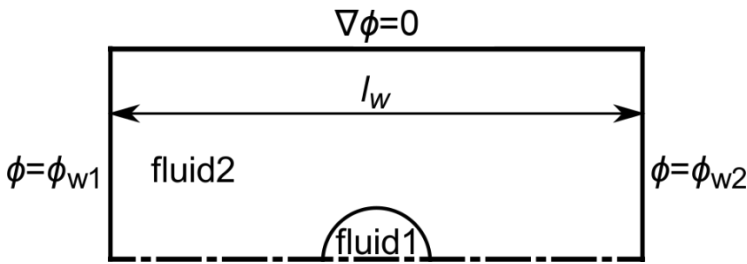
*Figure 3. An illustration of the set-up for the drop analysis*

## 3. 2. 1. Curl of the electric field strength

In order to analyze the precision of the numerical procedure, the curl of the electric field strength was considered in the set-up described above using Eq. (5) for the dielectric force. Appearance of this curl signalizes numerical inaccuracy in the calculation. These inaccuracies could be easily overseen when magnetic field effects are also included. The simulation ended at $10^{-8}$ s, while $\phi_{w1}$ was equal to 125.7 V.

Different expressions for calculating the electric field strength (*i.e.* Eqs. (8)-(10)) can be compared based on the value of its curl. Eq. (15) was used for calculation of the electric potential. The curl of the electric field strength at the end of the simulation is shown in Figure 4. The expressions that use cell face values and their reconstruction for calculation of the electric field strength (*i.e.* Eqs. (9) and (10)) generated very large curl values within the geometry. These values are especially problematic from the point of view of possible future inclusion of magnetic field effects. In contrast, Eq. (8) produced much better results.
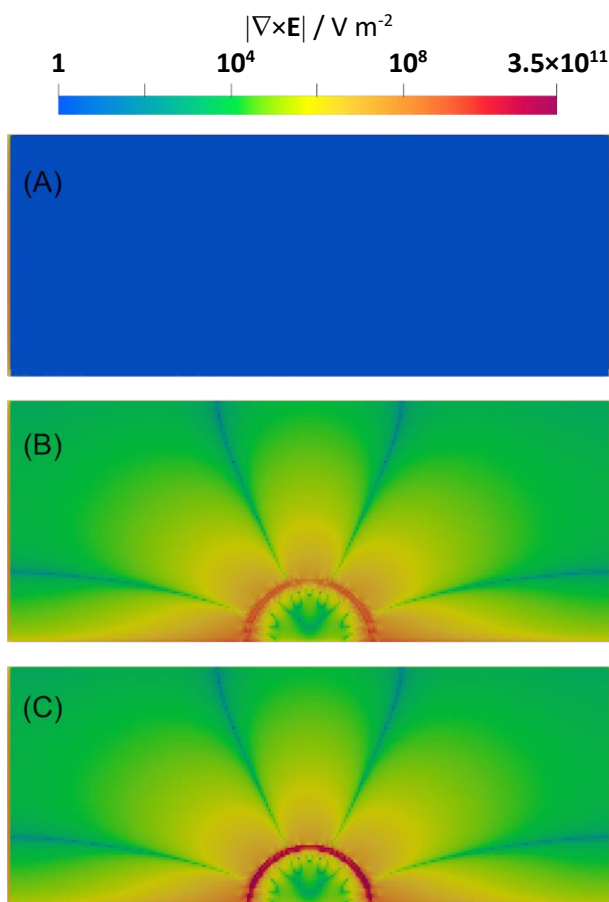


*Figure 4. The magnitude of the curl of the electric field strength (when the color map was set to start from 1) at the end of the simulation with the use of Eq. (15) and A: Eq. (8); B: Eq. (9); C: Eq. (10)*

If Eq. (9) is used, the mentioned curl can somewhat be reduced by using Eqs. (12)-(14) and (16)-(17), but the reduction is too small. At the end of the simulation, the maximum magnitude of the curl of the electric field was reduced from $4.4 \times 10^9$ to $2.5 \times 10^9$ V m$^{-2}$ when Eqs. (13) and (14) with either Eq. (15) or (17) were used, and to $3.3 \times 10^9$ V m$^{-2}$ when Eq. (17) was used. On the other hand, the results did not change when Eqs. (13) and (16) either with or without Eq. (14) were used.

Large values of the curl of the electric field strength were also obtained when a dynamic mesh and Eqs. (8) and (15) were used. In this case, the curl maximum magnitude at the end of the simulation was $1.3 \times 10^{12}$ V m$^{-2}$ within the geometry. These analyses lead to the conclusion that the applicability of dynamic meshes, or at least dynamic meshes in the OpenFOAM® software, could be questionable in cases in which the electric field influences fluids, leading also to questionable results if the calculated curl of the electric field strength is not presented.

If Eqs. (8) and (15) and a cell limiter for the gradient of the electric potential are used, large values of the curl of the electric field strength can be also obtained. At the end of the simulation the maximum curl value was $1.3 \times 10^{11}$ V m$^{-2}$ in the interior. This result indicates that the use of limiters for the gradient of the electric potential could be unacceptable. Also, special attention should be paid if magnetic field effects are included, in which case this problem might not be so easily seen.

Based on these findings, use of Eqs. (8) and (15) for calculations of the electric field strength and the electric potential, respectively, could be recommended, while the use of dynamic meshes and limiters of the gradient of the electric potential is not recommended. Also, calculation of the curl of the electric field strength for the perfect dielectric model and other EHD models should be included because otherwise the results could be questionable.

## 4. CONCLUSIONS

Based on this work several conclusions could be deduced. Inclusion of the calculation of the curl of the electric field strength is recommended, especially if suitability of the model is considered for future inclusion of magnetic field effects. Because of this curl, the expression that uses a value in the cell center could be recommended instead of the ones that use values on the cell faces after analysis, while the applicability of dynamic meshes and limiters of the gradient of the electric field strength was shown to be questionable. Different expressions for calculation of the dielectric force were compared and those that use values on the cell faces showed better results than those that use values in the cell center only. A new electric Courant number was included, in addition to the standard Courant number, in order to improve calculation efficiency and quality of the results, which is expected to be useful in future calculations. It is hoped that inclusion of this new electric Courant number will be valuable in all calculations involving electric fields. By using this work as a basis, a deeper analysis of implementation of the perfect dielectric model and its comparison with the analytical prediction can be performed, which will be the topic of next investigations.

## REFERENCES

[1]   López-Herrera JM, Popinet S, Herrada MA. A charge-conservative approach for simulating electrohydrodynamic two-phase flows using volume-of-fluid. *J Comput Phys*. 2011; 230: 1939-1955 https://dx.doi.org/10.1016/j.jcp.2010.11.042

[2]   Castellanos A, ed. Electrohydrodynamics. Vienna, Austria: Springer-Verlag Wien; 1998 https://dx.doi.org/10.1007/978-3-7091-2522-9

[3]   Bošković S, Bugarski B. Review of electrospray observations and theory. *J Eng Process Manag*. 2018; 10: 41-53 https://dx.doi.org/10.7251/jepm181002041b

[4]   Singh R, Bahga SS, Gupta A. Electrohydrodynamics in leaky dielectric fluids using lattice Boltzmann method. *Eur J Mech B Fluids*. 2019; 74: 167-179 https://dx.doi.org/10.1016/j.euromechflu.2018.11.011

[5]   Shin W-T, Yiacoumi S, Tsouris C. Electric-field effects on interfaces: electrospray and electrocoalescence. *Curr Opin Colloid Interface Sci*. 2004; 9: 249-255 https://dx.doi.org/10.1016/j.cocis.2004.06.006

[6]     Pongrác B, Kim H-H, Negishi N, Machala Z. Influence of water conductivity on particular electrospray modes with dc corona discharge – optical visualization approach. *Eur Phys J D*. 2014; 68: 224 https://dx.doi.org/10.1140/epjd/e2014-50052-4

[7]     Fernandez de la Mora J, Van Berkel GJ, Enke CG, Cole RB, Martinez-Sanchez M, Fenn JB. Electrochemical processes in electrospray ionization mass spectrometry. *J Mass Spectrom*. 2000; 35: 939-952 https://dx.doi.org/10.1002/1096-9888(200008)35:8<939::aid-jms36>3.0.co;2-v

[8]     Notz PK, Basaran OA. Dynamics of Drop Formation in an Electric Field. *J Colloid Interface Sci*. 1999; 213: 218-237 https://dx.doi.org/10.1006/jcis.1999.6136

[9]     Xie J, Wang C-H. Encapsulation of Proteins in Biodegradable Polymeric Microparticles Using Electrospray in the Taylor Cone-Jet Mode. *Biotechnol Bioeng*. 2007; 97: 1278-1290 https://dx.doi.org/10.1002/bit.21334

[10]    Thirumalaisamy R, Natarajan G, Dalal A. Towards an improved conservative approach for simulating electrohydrodynamic two-phase flows using volume-of-fluid. *J Comput Phys*. 2018; 367: 391-398 https://dx.doi.org/10.1016/j.jcp.2018.04.024

[11]    Bugarski B, Smith J, Wu J, Goosen MFA. Methods for animal cell immobilization using electrostatic droplet generation. *Biotechnol Techn*. 1993; 7: 677-682 https://dx.doi.org/10.1007/BF00151869

[12]    Bugarski B, Li Q, Goosen MFA, Poncelet D, Neufeld RJ, Vunjak G. Electrostatic Droplet Generation: Mechanism of Polymer Droplet Formation. *AIChE J*. 1994; 40: 1026-1031 https://dx.doi.org/10.1002/aic.690400613

[13]    Poncelet D, Bugarski B, Amsden BG, Zhu J, Neufeld R, Goosen MFA. A Parallel plate electrostatic droplet generator: parameters affecting microbead size. *Appl Microbiol Biotechnol*. 1994; 42: 251-255 https://dx.doi.org/10.1007/BF00902725

[14]    Poncelet D, Neufeld RJ, Goosen MFA, Burgarski B, Babak V. Formation of microgel beads by electric dispersion of polymer solutions. *AIChE J*. 1999; 45: 2018-2023 https://dx.doi.org/10.1002/aic.690450918

[15]    Manojlovic V, Djonlagic J, Obradovic B, Nedovic V, Bugarski B. Immobilization of cells by electrostatic droplet generation: a model system for potential application in medicine. *Int J Nanomed*. 2006; 1: 163-171 https://dx.doi.org/10.2147/nano.2006.1.2.163

[16]    Poncelet D, Babak VG, Neufeld RJ, Goosen MFA, Burgarski B. Theory of electrostatic dispersion of polymer solutions in the production of microgel beads containing biocatalyst. *Adv Colloid Interface Sci*. 1999; 79: 213-228 https://dx.doi.org/10.1016/S0001-8686(97)00037-7

[17]    Supeene G, Koch CR, Bhattacharjee S. Deformation of a droplet in an electric field: Nonlinear transient response in perfect and leaky dielectric media. *J Colloid Interface Sci*. 2008; 318: 463-476 https://dx.doi.org/10.1016/j.jcis.2007.10.022

[18]    Munoz CN. Computational modelling of electrohydrodynamic atomization. MSc. Thesis, The University of Manchester, Manchester, UK; 2014.

[19]    Reddy MN, Esmaeeli A. The EHD-driven fluid flow and deformation of a liquid jet by a transverse electric field. *Int J Multiphase Flow*. 2009; 35: 1051-1065 https://dx.doi.org/10.1016/j.ijmultiphaseflow.2009.06.008

[20]    Taylor GI. Studies in electrohydrodynamics. I. The circulation produced in a drop by an electric field. *Proc R Soc London, Ser A*. 1966; 291: 159-166 https://dx.doi.org/10.1098/rspa.1966.0086

[21]    Moukalled F, Mangani L, Darwish M. The Finite Volume Method in Computational Fluid Dynamics: An Advanced Introduction with OpenFOAM® and Matlab®. Switzerland: Springer International Publishing Switzerland; 2016 https://dx.doi.org/10.1007/978-3-319-16874-6

[22]    Andersson B, Andersson R, Håkansson L, Mortensen M, Sudiyo R, Van Wachem B, Hellstrom L. Computational Fluid Dynamics for Engineers. Cambridge, UK: Cambridge University Press; 2012. ISBN: 978-1-107-01895-2

[23]    Li X-g, Fritsching U. Spray Transport Fundamentals. In: Henein H, Uhlenwinkel V, Fritsching U, eds. *Metal Sprays and Spray Deposition*. Cham, Switzerland: Springer International Publishing AG; 2017:89-176 https://dx.doi.org/10.1007/978-3-319-52689-8

[24]    Hemida H. OpenFOAM tutorial: Free surface tutorial using interFoam and rasInterFoam. 2008.

[25]    Lima NC. Numerical Studies in Electrohydrodynamics. Ph.D. Thesis, School of Mechanical Engineering of the University of Campinas; 2017.

[26]    Chen C-H. Electrohydrodynamic Stability. In: Ramos A, ed. *Electrokinetics and Electrohydrodynamics in Microsystems*. New York, New York, USA: SpringerWienNewYork; 2011:177-220 https://dx.doi.org/10.1007/978-3-7091-0900-7

[27]    Lastow O, Balachandran W. Numerical simulation of electrohydrodynamic (EHD) atomization. *J Electrostat*. 2006; 64: 850-859 https://dx.doi.org/10.1016/j.elstat.2006.02.006

[28]    Greenshields CJ. OpenFOAM The Open Source CFD Toolbox: Programmer's Guide Version 3.0.1. OpenFOAM Foundation Ltd.; 2015.

[29]    Davidson PA. Turbulence: An Introduction for Scientists and Engineers. New York, USA: Oxford University Press; 2004. ISBN: 0198529481

[30]    Aguerre HJ, Pairetti CI, Venier CM, Márquez Damián S, Nigro NM. An oscillation-free flow solver based on flux reconstruction. *J Comput Phys*. 2018; 365: 135-148 https://dx.doi.org/10.1016/j.jcp.2018.03.033

[31]    Sander S, Gawor S, Fritsching U. Separating polydisperse particles using electrostatic precipitators with wire and spiked-wire discharge electrode design. *Particuology*. 2018; 38: 10-17 https://dx.doi.org/10.1016/j.partic.2017.05.014

[32]    Weber N, Galindo V, Stefani F, Weier T, Wondrak T. Numerical simulation of the Tayler instability in liquid metals. *New J Phys*. 2013; 15: 043034 https://dx.doi.org/10.1088/1367-2630/15/4/043034

# Ispitivanje elektrohidrodinamičkih proračuna

**Stefan A. Bošković[1], Aleksandar Karač[2], Slobodan B. Vrhovac[3], Aleksandar Belić[4] i Branko Bugarski[4]**

[1]*Inovacioni centar Tehnološko-metalurškog fakulteta u Beogradu d.o.o, Beograd, Srbija*
[2]*Politehnički fakultet, Univerzitet u Zenici, Zenica, Bosna i Hercegovina*
[3]*Univerzitet u Beogradu, Institut za fiziku Beograd, Beograd, Srbija*
[4]*Univerzitet u Beogradu, Tehnološko-metalurški fakultet, Beograd, Srbija*

(Naučni rad)

*Izvod*

Model idealnog dielektrika je uključen u programski paket OpenFOAM® (OpenFOAM Foundation, UK) i korišćen za ispitivanje i moguće poboljšavanje elektrohidrodinamičkih proračuna. Analizirana su dva različita seta numeričkih simulacija, u kojima su bila modelovana dva različita fluida. Prvi set je bio jednodimenzionalan dok je u drugom setu kap jednog fluida okružena drugim fluidom. U radu je pokazano da se određeni izrazi ili strategije izračunavanja mogu odbaciti usled pojave oscilacija i mogućeg veštačkog stvaranja rotora jačine električnog polja. Korišćenje pokretnih mreža, barem onih prisutnih u programskom paketu OpenFOAM®, i limitera za gradijent jačine električnog polja mogu dovesti do velikih numeričkih grešaka. Takođe je pokazano da bi korišćenje određenih vrednosti sa površi ćelija moglo poboljšati rezultate. Izraz za električni Kuronov broj je izveden dimenzionom analizom i mogao bi se preporučiti za buduće proračune. Očekuje se da su zaključci iz ovog rada prenosivi na druge, komplikovanije modele.

# Sunflower oil methanolysis over modified CaO catalysts

**Marija R. Miladinović[1], Milica Z. Petković[2], Ivana B. Banković-Ilić[2], Sandra S. Konstantinović[2] and Vlada B. Veljković[2,3]**

[1]*Faculty of Agriculture, University of Niš, Kosančićeva 4, 37000, Kruševac, Serbia*
[2]*Faculty of Technology, University of Niš, Bulevar Oslobodjenja 124, 16000, Leskovac, Serbia*
[3]*The Serbian Academy of Sciences and Arts, Knez Mihailova 35, 11000, Belgrade, Serbia*

*Abstract*

Oil methanolysis over modified CaO catalysts was studied to assess the catalytic performance and to define an appropriate kinetic model. CaO was modified by commercial glycerol and a deep eutectic solvent (DES), choline chloride : glycerol (ChCl : Gly), to obtain catalytically active complexes of CaO and glycerol. The main goal was to investigate the effect of the obtained complexes on the reaction rate and fatty acid methyl ester (FAME) content and to describe the variation of the triacylglycerol (TAG) conversion degree during the reaction time. Fourier transform infrared spectroscopy (FTIR) was applied to confirm the formation of CaO complexes with glycerol or the glycerol-based DES. Different catalyst loadings (0.5, 1, and 5 % of oil weight) and methanol-to-oil molar ratios (6 : 1 and 12 : 1) were applied for investigation of the sunflower oil methanolysis at 60 °C. Two kinetic models were employed yielding the kinetic parameters, which depended on the catalyst loading and the methanol-to-oil molar ratio. Both models showed valid applicability for describing the kinetics of the reactions catalyzed by both complexes (the mean relative percent deviation was lower than 10 %).

*Keywords:* biodiesel; calcium oxide; choline chloride-glycerol; deep eutectic solvents; kinetics.

*Available on-line at the Journal web address: http://www.ache.org.rs/HI/*

## 1. INTRODUCTION

Biodiesel, a mixture of fatty acid methyl (FAMEs) or ethyl (FAEEs) esters is considered a feasible alternative fuel to mineral diesel in engines with internal combustion because of many advantages in its application. It can be used as pure or blended in various ratios with petroleum-derived diesel. Its combustion produces significantly fewer particulates than that of diesel fuel and a lower sulfur emission, while it can be considered a carbon-neutral fuel if produced in a sustainable manner. Usually, the biodiesel production processes involve homogeneously or heterogeneously catalyzed trans-esterification of triacylglycerols (TAGs) sources, such as edible, non-edible, used, and waste vegetable oils or animal fats, and esterification of free fatty acids (FFA) with aliphatic alcohols. Since the reactants are not miscible at room temperature and atmospheric pressure, addition of a co-solvent, such as organic solvents [1], biodiesel itself [2], and ionic liquids (IL) [3] in the reaction mixture increases the solubility of alcohol in the oil phase. The co-solvent use provides a pseudo-homogeneous system [4], especially at lower temperatures when the mass transfer limits the chemical reaction [5].

Solid base catalysts are preferred over homogeneous catalysts in the transesterification reaction for biodiesel production. Despite having several advantages, such as easy separation and recovery, low waste and by-products, avoidance of corrosion, and facilitation of continuous process operation, solid base catalysts can require a complicated preparation procedure involving expensive precursors and exhibit variable quality and short lifetime [6]. For that reason, many studies were aimed at developing stable and active solid catalysts for biodiesel production processes, such as catalysts in nano-form [7]. Among various heterogeneous catalysts, calcium oxide (CaO), as a common base earth metal oxide, is one of the most promising for biodiesel production [8]. Kouzu *et al.* [9,10] pointed out that CaO shows activity only at the beginning of the reaction until the FAME content is below 30 %. As the methanolysis reaction proceeds, the

synthesized by-product glycerol can react with calcium ions from CaO producing a new highly active catalyst, calcium diglyceroxide (glyceroxide), $Ca(C_3H_7O_3)_2$. The CaO-glycerol complex formation provides a hydrophilic-hydrophobic active layer on the surface of CaO allowing easy access of hydrophobic TAG molecules to the active sites, thus increasing the methanolysis reaction rate [11].

The use of ionic liquids and deep eutectic solvents can also significantly improve the biodiesel production processes [12,13]. Presence of a DES, such as ChCl : glycerol, as a co-solvent in homogeneously catalyzed methanolysis of rapeseed oil [14] and waste cooking oil [12], or ethanolysis of palm oil [15,16], increased the biodiesel yield, reduced the side saponification reaction, and improved product separation and purification.

The use of ChCl-based DESs in heterogeneously catalyzed transesterification of vegetable oils has been rarely investigated. A DES prepared from ChCl and glycerol was applied in CaO-catalyzed methanolysis of rapeseed oil as a solvent and an activator of commercial CaO [6]. The presence of DES can eliminate inactive layers consisting of $CaCO_3$ and $Ca(OH)_2$ on the catalyst surface and can facilitate the separation of catalyst from the reaction mixture and enable achievement of a higher biodiesel yield. Troter *et al.* [17] have studied the impact of the ChCl-based DESs, with different amides or polyols as co-solvents, on the yield of ethyl esters obtained from expired sunflower oil using calcined and non-calcined CaO as a catalyst.

It was confirmed in literature that a CaO-glycerol-methanol complex was formed during transesterification, which was the active phase of the catalyst [10]. Furthermore, the catalytic activity of the used catalyst, showed to be higher than that of the fresh catalyst. So far, CaO-glycerol complexes were synthesized by using different methods, such as mixing of CaO with the mixture of methanol and glycerol at temperatures in the range 60-70 °C, followed by separation and washing with methanol or tetrahydrofuran [10,11,18-20], mixing of CaO with the mixture of methanol and glycerol under sonication [21] and mechanochemical treatment of CaO dispersed in glycerol [22]. Activation of CaO in the presence of ChCl : Gly as a co-solvent in sunflower oil methanolysis, was investigated by analyzing the spent catalyst [6], but modification of CaO with ChCl : Gly induced directly by mixing, has not been investigated yet. Therefore, this study aimed to investigate the effect of the complexes obtained by modification of CaO by mixing with glycerol and ChCl : Gly on the reaction rate and FAME content and to describe the variation of the TAG conversion degree during the reaction time.

## 2. EXPERIMENTAL

### 2. 1. Materials

Refined sunflower oil (Dijamant, Zrenjanin, Serbia) and methanol (purity of 99.5 %, Zorka Pharma, Šabac, Serbia) were used as the reactants. CaO (purity of ≥98, Sigma Aldrich, USA) was used for the catalyst preparation. Mixture of ChCl : Gly (molar ratio of 1 : 2) was prepared by using ChCl (purity of ≥98, Sigma Aldrich, USA) and glycerol (purity of 99.5 %, Ph. Eur, MeiLab Belgrade, Serbia). Methanol, 2-propanol, and *n*-hexane, HPLC grade (purity of 99.7 %, J.T. Baker, USA), were used for High Performance Liquid Chromatography (HPLC) analyses.

### 3.1. Catalyst preparation

CaO-glycerol complexes were prepared using two procedures. The first procedure [20], consisted of mixing CaO (3 g) with glycerol (10 g) and methanol (44 g) at 60 °C for 2 h. The obtained catalyst, here denoted as the C-G complex, was recovered by filtration and dried at 105 °C for 2 h. In the second procedure, CaO was modified with the ChCl : Gly, as a DES, prepared from ChCl and glycerol (molar ratio of 1: 2), which was then mixed (in the amount of 10 g) with CaO (3 g) at 60 °C for 1 h and dried at 105 °C for 2 h. This catalyst was denoted as the C-ChG complex. Both catalysts were stored in the well-closed glass bottles in a desiccator containing calcium chloride and potassium hydroxide pellets.

### 3.3. FTIR analysis

Fourier-transform infrared (FTIR) spectra of the obtained catalysts were recorded with a Michaelson Bomen MB-series spectrophotometer (BOMEM MB-100, Hartmann & Braun, Canada), using the KBr pellet (1 mg / 100 mg) technique.

### 3.4. Methanolysis reaction

The sunflower oil methanolysis was carried out in a 250 cm$^3$ two-neck round bottom glass flask, equipped with a condenser and a magnetic stirrer, placed in a chamber. The reaction was performed at 60 °C and under atmospheric pressure. The temperature was maintained constant (60 ± 0.1 °C) by water circulating from a thermostated water bath. Desired amounts of the catalyst (0.5, 1, or 5 % of oil weight) and methanol, corresponding to the initial methanol-to-oil molar ratio of 6 : 1 or 12 : 1, were added to the flask and agitated (400 rpm) at 60 °C for 30 min. Afterward, sunflower oil (30 g) that was preheated (at 60 °C) separately, was added to the methanol-catalyst suspension so that the total reaction mixture volume was 41.13 or 49.50 cm$^3$ (depending on the methanol-to-oil molar ratio), and the agitation intensity was raised to 900 rpm for 160 min.

Leaching experiments were performed in parallel in order to investigate leaching of the catalyst from the complex by mixing the C-G and C-ChG complexes (0.3 g) with methanol (16.76 cm$^3$) for 30 min at 60 °C. Then, the methanol-catalyst suspension was filtered under a vacuum to separate the catalyst from the methanol phase. The separated methanol phase was used for the reaction keeping the constant methanol-to-oil molar ratio of 12 : 1.

In all experiments in order to monitor the change of the reaction mixture composition, the samples (0.4 cm$^3$) were taken during the reaction at timed intervals (the total volume withdrawn was less than 10 %), quenched by immersing in ice water, and prepared for HPLC analysis [23]. HPLC analysis was performed by HPLC chromatography (Agilent 1100 Series, Agilent Technologies, Germany) [24]. All experiments were performed in duplicate.

### 3. KINETIC MODELING

The overall reaction of methanol and TAGs can be represented by the overall stoichiometric equations 1a and 1b:



(1a)

A + 3B ⇄ 3R + S　　　　　　　　(1b)
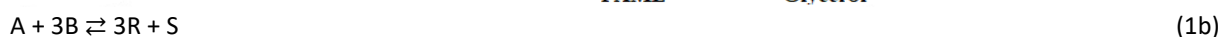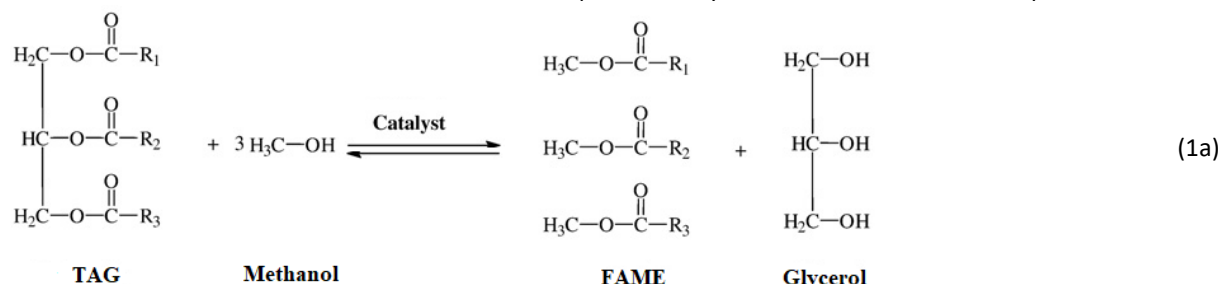
where A, B, R, and S denote TAGs, methanol, FAMEs, and glycerol, respectively. For modeling the kinetics of sunflower oil methanolysis over CaO modified with glycerol and ChCl : Gly, two kinetic models were tested.

a)  The semi-empirical model developed for the quicklime-catalyzed methanolysis [23] is expressed as:

$$\frac{dx_A}{dt} = k_{app} \cdot \frac{(1 - x_A) \cdot (c_{R0} + 3 \cdot c_{A0} \cdot x_A)}{K + c_{A0} \cdot (1 - x_A)}$$

(2)

where $x_A$ is the conversion degree of TAGs, $t$ is time, $k_{app}$ is the apparent reaction rate constant, $c_{R0}$ is the hypothetic initial FAME concentration corresponding to the initial available active catalyst surface, $c_{A0}$ is the initial TAG concentration, and $K$ is the model parameter defining the TAG affinity for the catalyst active sites.

b)  The model developed for CaO·ZnO catalyzed methanolysis [25] is expressed as:

$$\frac{dx_A}{dt} = \frac{k' \cdot (k_{mt,A})_0 \cdot \left[ 1 + \alpha x_A^\beta \right]}{k' + (k_{mt,A})_0 \cdot \left[ 1 + \alpha x_A^\beta \right]} \cdot (1 - x_A)$$

(3)

where $x_A$ and $t$ designate the same variables as in the model (a), $k'$ is the effective pseudo-first-order reaction rate constant, $(k_{mt,A})_0$ is the overall TAG volumetric mass transfer coefficient at the beginning of the process, and $\alpha$ and $\beta$ are fitting parameters.

General assumptions were as follows:

1.  The reaction was performed in the batch stirred reactor. High intensity of mixing provided a perfectly mixed reaction mixture with uniform composition and catalyst distribution.

2. The methanolysis reaction occurs between methoxide ions and carbonyl groups of approaching hydrophobic TAG molecules [18].

3. TAG mass transfer limitations are negligible in the initial period of the methanolysis reaction and are not included in the kinetics modeling of methanolysis, catalyzed by CaO modified with commercial glycerol and ChCl-Gly.

4. The internal diffusion rate within catalyst particles did not affect the methanolysis reaction rate due to the small specific surface area of the Ca-diglyceroxide complex [18].

5. Neutralization of free fatty acids can be ignored since the refined sunflower oil was used. Hence, the catalyst concentration was constant during the methanolysis.

## 4. RESULTS AND DISCUSSION

### 4. 1. FTIR analysis

Surfaces of neat CaO and its complexes with glycerol and ChCl : Gly were characterized by FTIR spectra (Figure 1) while the numerical data are given in Table 1. The spectrum of neat CaO contains a weak band at 3424 cm$^{-1}$ due to $v$(OH) stretching vibration. The band originates from the OH group located in Ca(OH)$_2$. Namely, the surface of CaO is covered with Ca(OH)$_2$ and CaCO$_3$, due to hydration and carbonization of CaO. The spectrum of the C-ChG complex contains a wide and strong band at 3388 cm$^{-1}$, due to $v$(OH) stretching vibration. Appearance of this band suggests the formation of an intramolecular hydrogen bond since the ChCl molecule contains both donor and acceptor of hydrogen. The bending OH vibration can be observed at 1650 cm$^{-1}$ while stretching ($v_{as}$(CH)) and ($v_s$(CH)) vibrations are at 2933 and 2843 cm$^{-1}$, respectively. A similar finding was observed in the FTIR spectrum of CaO after the transesterification process in the presence of the same DES (ChCl-Gly) as a co-solvent showing the characteristic peaks for Ca-diglyceroxide [6]. These characteristic vibrations for the spectrum of Ca-diglyceroxide complex are not present in the spectrum of the neat CaO. The same analysis can be applied to the modified CaO with commercial glycerol. Formation of the C-G complex can be confirmed by a strong and wide band at 3404 cm$^{-1}$, which can be assigned to stretching $v$(OH) vibration of hydrogen-bonded hydroxyl group, and proper bending vibration at ~1648 cm$^{-1}$, as well as the symmetrical and asymmetrical stretching vibrations of a methylene group (Table 1). The spectra of C-G and C-ChG complexes, after washing with methanol (Figure 1c,e) did not show appreciable changes in the band positions and intensities. This indicated the complex stability.

*Table 1. Numerical data of the FTIR spectra for the neat CaO and C-G and C-ChG complexes*

| Band assignation | Wavenumber, cm$^{-1}$ | | |
|---|---|---|---|
| | Neat CaO | C-G complex | C-ChG complex |
| $v$(OH) | 3424 | 3404 | 3388 |
| $v_{as}$(CH) | | 2926 | 2933 |
| $v_s$(CH) | | 2860 | 2843 |
| $\delta$(OH) | 1470 | 1648 | 1650 |
| $\delta$(CH) | | 1416 | 1419 |
| $v$(C-O) | 1114 | 1108 | 1123 |
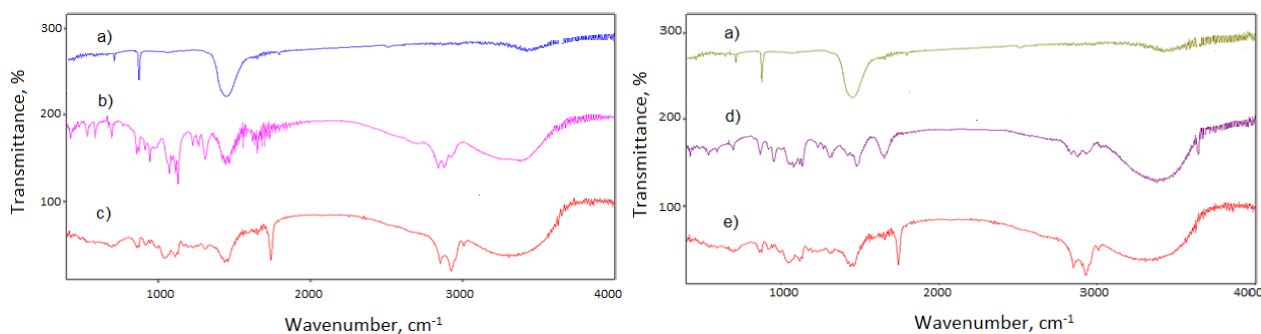


*Figure 1. FTIR spectra of the neat CaO (a), the C-G complex before (b) and after (c) washing with methanol and the C-ChG complex before (d) and after (e) washing with methanol*

## 4. 2. Sunflower oil methanolysis over the modified CaO catalysts

Variation of the FAME content during the sunflower oil methanolysis catalyzed by the C-G and C-ChG complexes at different initial methanol-to-oil molar ratios and catalyst loadings is shown in Figure 2. In both catalyst cases, independently of the initial methanol-to-oil molar ratio, the overall reaction rate and the content of FAMEs were lower at the lowest catalyst loading (0.5 %). It was probably the result of a lower available catalytic surface for the reaction. With increasing the catalyst loading to 1 %, the mass transfer resistance in the initial period of the reaction did not occur. More available catalytic active sites were provided by increasing the catalyst loading so that it affected the overall reaction rate, reaching the highest FAME content at a shorter reaction time. However, a further increase in the catalyst loading (5 %) decreased the reaction rate and the FAME content. This higher catalyst loading provided larger catalytically active surface but lower mixing efficiency of the reaction mixture at the beginning due to higher viscosity of the reaction mixture. A similar effect of the catalyst loading on the FAME content has been already observed [21,22].

The effect of the initial methanol-to-oil molar ratio on the reaction rate and FAME content depended on the catalyst loading and was more emphasized with the C-G complex (Figure 2a,b) than with the C-ChG complex (Figure 2c,d). A lower FAME content was observed at the C-G complex loading of 1 % when a higher methanol-to-oil molar ratio was employed. This could be the result of the higher methanol amount, which increased the total volume of the reaction mixture and diluted the catalyst concentration relative to methanol. A significant effect of the methanol amount on the reaction rate and FAME content was not observed at the lowest catalyst loading (0.5 %) due to the lower catalyst concentration. Moreover, the excess of methanol provides a better solubility of the produced glycerol that will more likely cover the active layer of the catalyst. This could be the reason for the insignificant effect of the methanol-to-oil molar ratio on the reaction rate and FAME content in the case of the C-ChG complex. Lukić *et al.* [22] have reported that the increase of the methanol-to-oil molar ratio affected only the final period of the reaction. On the other hand, when the methanol-oil molar ratio decreased from 14 : 1 to 7 : 1, Ferrero *et al.* [21] noticed a decrease of the FAME yield by 5 and 2 % in the initial and final periods of the reaction, respectively.
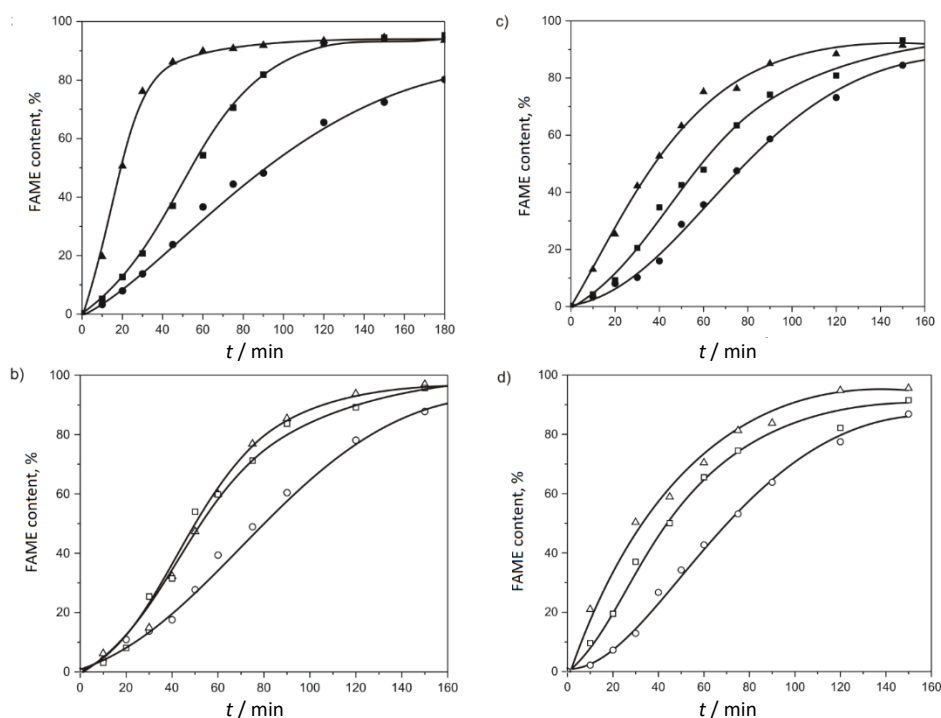


*Figure 2. FAME content over time during the reaction catalyzed by the C-G (a,b) and C-ChG (c,d) complexes (catalyst loading: circles –0.5 %, triangles – 1 %, squares – 5 %; methanol-to-oil molar ratio: 6 : 1 – solid symbols and 12 : 1 – open symbols) (data are average of n = 240, average SD=1.12 CL=95 %)*

Comparison of the sunflower oil methanolysis catalyzed by the C-G and C-ChG complexes and by quicklime [23], at the same operating conditions (methanol-to-oil molar ratio and catalyst loading), is shown in Figure 3. With the C-ChG

complex, the fastest reaction in the initial reaction period and a lower FAME content in the final reaction period were achieved due to the reduced TAG mass transfer resistance and to a reverse reaction promoted by increasing the glycerol concentration, respectively. The TAG concentration decreased near the active sites of the catalyst and the reaction between the produced FAME and glycerol was more likely to happen [22]. When quicklime was used as a catalyst, the formation of the CaO-glycerol complex during the reaction happened gradually, and the concentration of glycerol as a by-product still was not at the level to promote the reverse reaction as in the reactions catalyzed by the C-G and C-ChG complexes. The transformation of CaO into Ca-glyceroxide during the methanolysis requires a higher amount of glycerol [9,26]. Thereby, Ca-glyceroxide was formed at the end of the reaction (after 2 h), while at the beginning of the reaction (after 1 h) it could hardly be distinguished because of the low amount of glycerol [26]. It was concluded that Ca-glyceroxide can be generated on the surface of CaO particles by pre-treating them with glycerol; however, an excess of glycerol would cover the surface of Ca-glyceroxide and decreases its activity. This was supported by the observed decreased FAME content as more glycerol was added into the reaction mixture [10,26]. Also, with Ca-diglyceroxide, the TAG conversion degree increases proportionally to the catalyst loading, reaching 100 % at the catalyst loading of 1.46 % [19]. Therefore, optimization of the reaction conditions is suggested to maximize the FAME content.

Figure 4 shows the FAME formation during the sunflower oil methanolysis, catalyzed by the leachates obtained by mixing the C-G and C-ChG complexes with methanol for 30 min (60 °C) and separating the liquid phase by filtration. In both cases, the FAME content did not exceed the value of 2 % indicating a low catalyst leaching and the heterogeneous nature of the C-G and C-ChG complexes.

Many researchers have investigated the stability of Ca-diglyceroxide. Ca-diglyceroxide synthesized directly from hydrated lime and glycerol was not stable in biodiesel, methanol, water, and castor oil at 60 °C and its lixiviation was affected by the oil acidity [19]. The complex obtained by immersing CaO into glycerol blended with methanol was poorly soluble [10]. In the present study, the C-G and C-ChG complexes were synthesized in the presence of a large amount of methanol and directly from CaO and ChCl : Gly, respectively. Therefore, the nature of catalysis (homo- or hetero-geneous) depends on the method of the synthesis of CaO/glycerol complexes and the type and acidity of oily feedstock. In the case of refined sunflower oil used in the present study, the influence of the oil acidity on the lixiviation of the C-G and C-ChG complexes can be ignored.
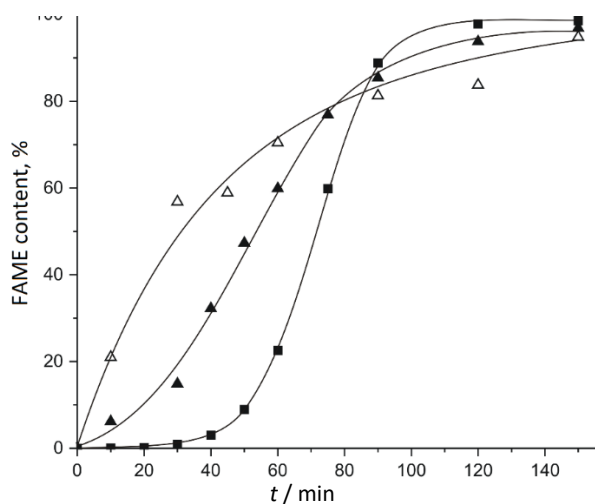


*Figure 3. Comparison of FAME formation during the sunflower oil me-thanolysis catalyzed by the C-G (▲) and C-ChG complexes (△), and quicklime [23] (■) (methanol-to-oil molar ratio of 12 : 1, catalyst load-ing of 1 %) (data are average of n = 52, average SD = 1.24, CL = 95 %)*
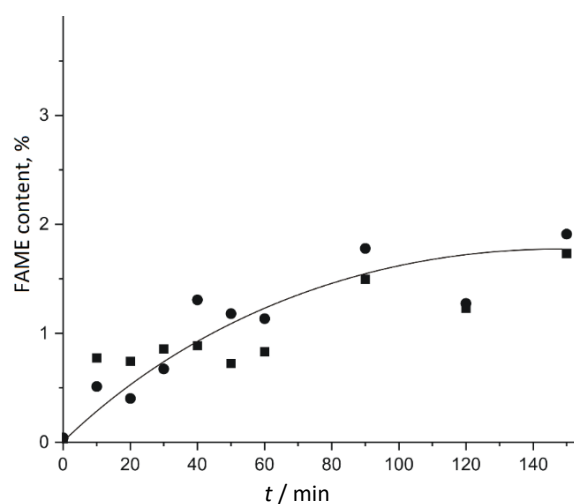
*Figure 4. The FAME content achieved in the reaction catalyzed by leachate of the C-G (●) and C-ChG (■) complexes (methanol-to-oil molar ratio 12 : 1) (data are average of n = 36, SD = 0.19, CL = 95 %)*

## 4. 3. Kinetics of the sunflower oil methanolysis over the modified CaO catalysts

The kinetic models, originally developed for the reactions catalyzed by quicklime [23] and Ca-diglyceroxide [22], were applied for the kinetic analysis of the sunflower methanolysis over the modified CaO catalysts. Both models have

been shown applicable for describing the kinetics of the reactions catalyzed by CaO, quicklime, $Ca(OH)_2$, and $CaO \cdot ZnO$ if the catalyst loading is higher than 0.5 % [27,28]. The values of the kinetic parameters are presented in Tables 2 and 3 along with the mean relative percent deviation (MRPD) between the calculated and experimental values of TAG conversion degree. The comparison of experimental data of TAG conversion degree with the predicted values, calculated by both kinetic models, is shown in Figure 5.

Generally, the apparent reaction rate constant $k_{app}$, depended on the reaction conditions. Independently of the catalyst type, the $k_{app}$-values decreased above the catalyst loading of 1 % (Table 2). Although the higher catalyst loading in the reaction mixture provided more active sites, which facilitated the reaction rate, a higher catalyst loading could hinder efficient mixing. Therefore, an increase in the methanol-to-oil molar ratio did not significantly affect the $k_{app}$-values at catalyst loadings above 1 %. The parameter $K$ for the C-G and C-ChG complexes was not affected by the reaction conditions as being constant. The values of parameter $c_{R0}$ did not show a consistent trend concerning the catalyst loading and the methanol-to-oil molar ratio.

The values of the effective pseudo-first-order reaction rate constant ($k'$) of the second model [22,25] for both catalysts (Table 3) increased with increasing the catalyst loading up to 1 % and then decreased with the further catalyst loading increase. Beyond 1 % of the catalyst loading, the $k'$-value of the C-G complex decreased with the increase of the methanol-to-oil molar ratio but not in the case of the C-ChG complex. The values of the overall TAG volumetric mass transfer coefficient at the beginning of the reaction ($k_{mt,A})_0$ followed a similar pattern as the reaction rate constant $k'$ with respect to the catalyst loading (Table 3). The methanol-to-oil molar ratio affected the $(k_{mt,A})_0$ -values positively in the case of the C-ChG complex but an opposite effect was observed for the C-G reaction system. The $\alpha$-values for both catalysts increased with increasing the catalyst loading up to 1 %, followed by a decrease at a higher catalyst load (5 %). A positive effect of the methanol-to oil molar ratio on the $\alpha$-values was observed only for the reaction catalyzed by the C-G complex. Higher values of the fitting parameter $\beta$ were obtained for the catalyst loading over 1 % and did not change with the methanol-to-oil molar ratio. The shape of the TAG conversion curves depended on the catalyst loading and methanol-to-oil molar ratio and shifted from exponential to slight sigmoidal. The $(k_{mt,A})_0$-values depended on the transition from the heterogeneous to the pseudo-homogeneous regime. If the reaction system was pseudo-homogeneous, the $(k_{mt,A})_0$-values increased, becoming closer to the $k'$-values or even higher. The $(k_{mt,A})_0$-values were lower when the curve departed from the exponential pattern, which can be ascribed to the presence of the lower catalyst amount in the reaction mixture that did not provide sufficient quantity of catalytic active sites or the higher catalyst amount that hindered mixing efficiency of the reaction mixture at the beginning of the reaction.

*Table 2. Determined model parameters for the model proposed by Miladinović et al. [23], Eq.(2)*

| Catalyst loading, % | $k_{app}$ / min$^{-1}$ | $K$ / mol dm$^{-3}$ | $c_{R0}$ / mol dm$^{-3}$ | $R^2$ | MRD, %* |
|---|---|---|---|---|---|
| | | C-G complex | | | |
| | | Methanol to oil molar ratio 6 : 1 | | | |
| 0.5 | 0.010 | 3.019 | 2.407 | 0.939 | 9.19 |
| 1.0 | 0.094 | 3.019 | 0.909 | 0.920 | 5.77 |
| 5.0 | 0.052 | 3.019 | 0.331 | 0.970 | 2.53 |
| | | Methanol to oil molar ratio 12 : 1 | | | |
| 0.5 | 0.040 | 3.019 | 0.361 | 0.928 | 7.54 |
| 1.0 | 0.052 | 3.019 | 0.305 | 0.976 | 7.74 |
| 5.0 | 0.051 | 3.019 | 0.539 | 0.946 | 5.52 |
| | | C-ChG complex | | | |
| | | Methanol to oil molar ratio 6 : 1 | | | |
| 0.5 | 0.028 | 3.019 | 0.658 | 0.922 | 8.39 |
| 1.0 | 0.032 | 3.019 | 1.625 | 0.940 | 3.45 |
| 5.0 | 0.028 | 3.019 | 1.076 | 0.972 | 8.37 |
| | | Methanol to oil molar ratio 12 : 1 | | | |
| 0.5 | 0.026 | 3.019 | 0.963 | 0.965 | 9.32 |
| 1.0 | 0.034 | 3.019 | 2.009 | 0.995 | 7.00 |
| 5.0 | 0.032 | 3.019 | 1.206 | 0.999 | 5.58 |

*Mean relative deviation

*Table 3. Determined model parameters for the model proposed by Lukić et al. [22,25], Eq. (3)*

| Catalyst loading, % | $k'$ / min⁻¹ | $(k_{mt,A})_0$ / min⁻¹ | $\alpha$ | $\beta$ | $R^2$ | MRD*, % |
|---|---|---|---|---|---|---|
| | | C-G complex | | | | |
| | | Methanol-to-oil molar ratio 6 : 1 | | | | |
| 0.5 | 0.011 | 0.009 | 11.79 | 1 | 0.948 | 10.74 |
| 1.0 | 0.080 | 0.029 | 27.09 | 2 | 0.944 | 7.34 |
| 5.0 | 0.055 | 0.009 | 15.12 | 2 | 0.961 | 6.45 |
| | | Methanol-to-oil molar ratio 12 : 1 | | | | |
| 0.5 | 0.035 | 0.002 | 28.29 | 1 | 0.955 | 9.55 |
| 1.0 | 0.048 | 0.005 | 66.49 | 2 | 0.979 | 6.37 |
| 5.0 | 0.033 | 0.008 | 41.39 | 2 | 0.953 | 6.49 |
| | | C-ChG complex | | | | |
| | | Methanol-to-oil molar ratio 6 : 1 | | | | |
| 0.5 | 0.025 | 0.003 | 16.17 | 1 | 0.943 | 8.64 |
| 1.0 | 0.031 | 0.026 | 28.68 | 2 | 0.977 | 2.71 |
| 5.0 | 0.027 | 0.011 | 23.18 | 2 | 0.990 | 7.73 |
| | | Methanol-to-oil molar ratio 12 : 1 | | | | |
| 0.5 | 0.045 | 0.007 | 5.17 | 1 | 0.989 | 9.18 |
| 1.0 | 0.031 | 1.153 | 22.73 | 2 | 0.999 | 7.51 |
| 5.0 | 0.030 | 0.017 | 8.85 | 2 | 0.994 | 4.75 |

*Mean relative deviation
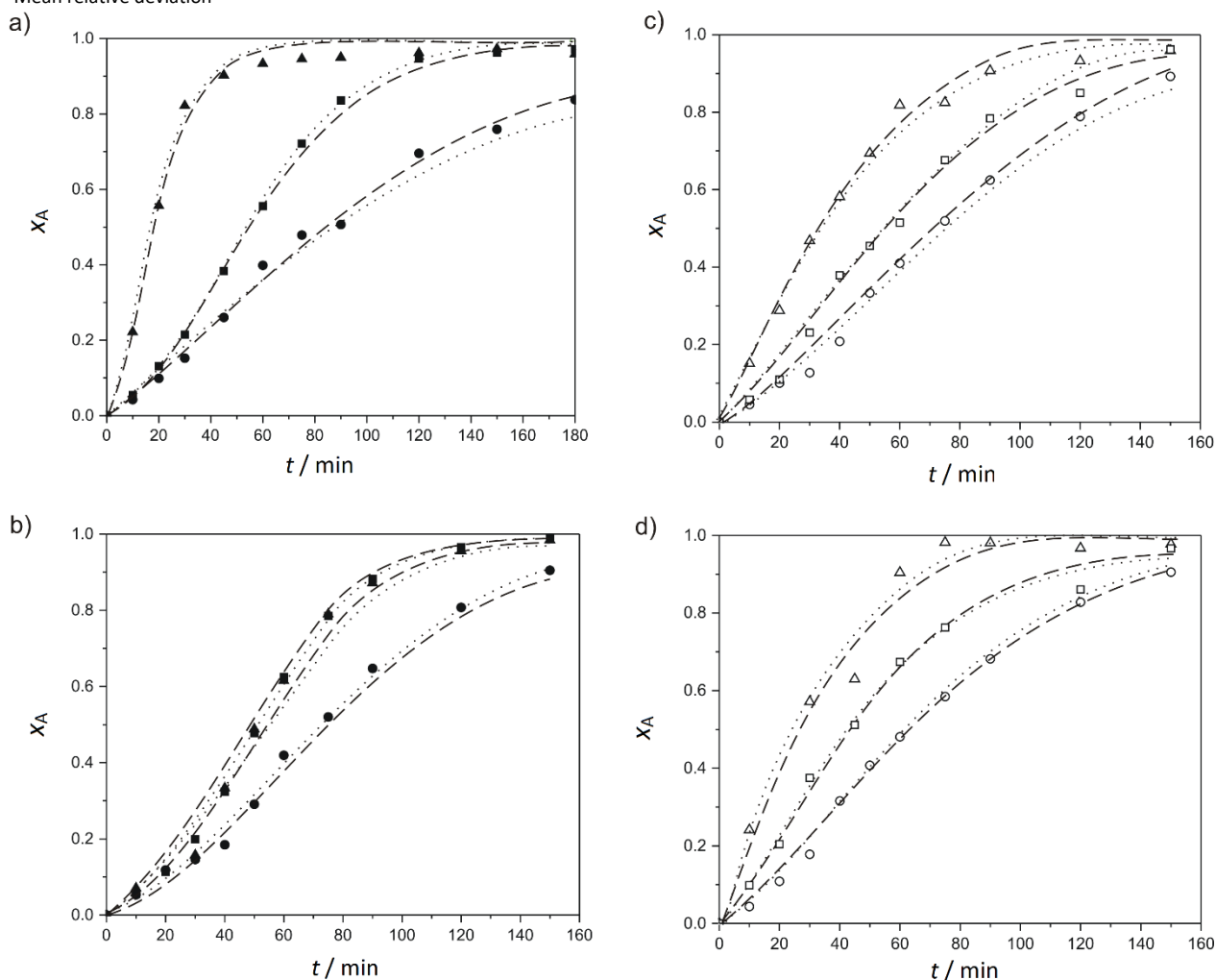


*Figure 5. Comparison of the experimental and predicted values of the TAG conversion degree calculated by the kinetic models based on Miladinović et al. [23], Eq. (2) (——) and Lukić et al. [22,25], Eq. (3) (···) in the presence of the C-G (solid symbols; a,b) and C-ChG (open symbols; c,d) complexes (methanol-to-oil molar ratio: (a,c) 6 : 1, (b,d) 12 : 1; catalyst loading: 0.5 % - circles, 1 % - triangles, 5 % - squares) (experimental data are average of n = 240)*

## 5. CONCLUSION

Catalytically active complexes of CaO and glycerol were obtained by modifying CaO with commercial glycerol and the ChCl : glycerol DES. The FTIR analysis confirmed formation of the CaO-glycerol complexes, both for the CaO modification with glycerol and ChCl : glycerol. When the CaO-glycerol complexes were employed as catalysts, the TAG mass transfer resistance was reduced in the initial period of the reaction and depended on the catalyst loading and the methanol-to-oil molar ratio. The optimal catalyst loading was 1 % based on the oil weight. The pseudo-homogeneous regime was more pronounced in the case of the C-ChG complex. The reactions catalyzed by the C-G and C-ChG complexes were faster in the initial period compared to the reaction catalyzed by quicklime. However, a shorter initial reaction period was achieved with the C-ChG complex than with the C-G complex. These reactions take place in the pseudo-homogeneous regime, but the maximum FAME content was lower as compared to the reaction catalyzed by quicklime at the same reaction conditions, likely due to the reversible reaction. Furthermore, the C-G and C-ChG complexes provided heterogeneous catalysis, confirmed by a negligible content of FAME synthesized in the presence of leachate. Two different kinetic models, originally developed for the quicklime and CaO·ZnO catalyzed reactions, successfully described the kinetics of the sunflower oil methanolysis catalyzed by the C-G and C-ChG complexes. The obtained results will have a significant contribution to the research of reducing the mass transfer limitation by modification of CaO surface, which improves the reaction kinetics.

## NOMENCLATURE

$c_{A0}$ - Initial TAG concentration, mol dm$^{-3}$

$c_{B0}$ - Initial methanol concentration, mol dm$^{-3}$

$c_{cat}$ - Catalyst concentration, mol dm$^{-3}$

$c_{R0}$ - Hypothetic initial FAME concentration corresponding to the initial available active catalyst surface, mol dm$^{-3}$

$CL$ - Confidence level

$k_{app}$ - Apparent reaction rate constant, Eq. (2), min$^{-1}$

$k'$ - Effective pseudo first-order reaction rate constant, Eq. (3), min$^{-1}$

$K$ - Model parameter defining the TAG affinity for the catalyst active sites, mol dm$^{-3}$

$(k_{mt,A})_0$ - Overall TAG volumetric mass transfer coefficient at the beginning of the process, min$^{-1}$

$SD$ - Standard deviation

$t$ - Time, min

$x_A$ - Conversion degree of TAG

$\alpha$ - Fitting parameter Eq. (3)

$\beta$ - Fitting parameter Eq. (3).

## REFERENCES

[1]    Boocock DGB, Konar SK, Mao V, Sidi H, Fast one-phase oil-rich processes for the preparation of vegetable oil methyl esters. *Biomass Bioenerg.* 1996; 11: 43-50. https://doi.org/10.1016/0961-9534(95)00111-5

[2]    Sakthivel S, Halder S, Gupta PD, Influence of Co-Solvent on the Production of Biodiesel in Batch and Continuous Process. *Int J Green Energy* 2013; 10: 876-884. https://doi.org/10.1080/15435075.2012.727365

[3]    Zhao H, Baker GA, Ionic liquids and deep eutectic solvents for biodiesel synthesis: a review. *J Chem Technol Biotechnol*. 2013; 88: 3-12. https://doi.org/10.1002/jctb.3935

[4]    Todorović ZB, Stamenković OS, Stamenković IS, Avramović JM, Veličković AV, Banković-Ilić IB, Veljković VB, The effects of cosolvents on homogeneously and heterogeneously base-catalyzed methanolysis of sunflower oil. *Fuel* 2013; 107: 493-502. https://doi.org/10.1016/j.fuel.2012.11.049

[5]   Banković-Ilić IB, Todorović ZB, Avramović JM, Veličković AV, Veljković VB, The effect of tetrahydrofuran on the base-catalyzed sunflower oil methanolysis in a continuous reciprocating plate reactor. *Fuel Process Technol*. 2015;,137:,339-350. https://doi.org/10.1016/j.fuproc.2015.03.023

[6]   Huang W, Tang S, Zhao H, Tian S, Activation of Commercial CaO for Biodiesel Production from Rapeseed Oil Using a Novel Deep Eutectic Solvent. *Ind Eng Chem Res*. 2013; 52: 11943–47. https://doi.org/10.1021/ie401292w

[7]   Banković-Ilić IB, Miladinović MR, Stamenković OS, Veljković VB, Application of nano CaO-based catalysts in biodiesel synthesis. *Renew Sustain Energy Rev*. 2017; 72: 746-760. http://dx.doi.org/10.1016/j.rser.2017.01.076

[8]   Marinković DM, Stanković MV, Veličković AV, Avramović JM, Miladinović MR, Stamenković OS, Veljković VB, Jovanović DM, Calcium oxide as a promising heterogeneous catalyst for biodiesel production: Current state and perspectives. *Renew Sustain Energy Rev*. 2016; 56: 1387–408. https://doi.org/10.1016/j.rser.2015.12.007

[9]   Kouzu M, Kasuno T, Tajika M, Yamanaka S, Hidaka J, Active phase of calcium oxide used as solid base catalyst for transesterification of soybean oil with refluxing methanol. *Appl Catal A Gen*. 2008; 334: 357–65. https://doi.org/10.1016/j.apcata.2007.10.023

[10]  Kouzu M, Hidaka JS, Wakabayashi K, Tsunomori M, Solid base catalysis of calcium glyceroxide for a reaction to convert vegetable oil into its methyl esters. *Appl Catal A Gen.* 2010; 390: 11–8. https://doi.org/10.1016/j.apcata.2010.09.029

[11]  Esipovich A, Danov S, Belousov A, Rogozhin A, Improving methods of CaO transesterification activity. *J Mol Catal A Chem*. 2014; 395: 225–233. http://dx.doi.org/10.1016/j.molcata.2014.08.011

[12]  Ranjan A, Dawn SS, Nirmala N, Santhosh A, Arun J, Application of deep eutectic solvent in biodiesel reaction: RSM optimization, CI engine test, cost analysis and research dynamics. *Fuel.* 2022; 307: 121933. https://doi.org/10.1016/j.fuel.2021.121933

[13]  Troter DZ, Todorović ZB, Đokić-Stojanović DR, Stamenković OS, Veljković VB, Application of ionic liquids and deep eutectic solvents in biodiesel production: A review. *Renew Sustain Energy Rev.* 2016; 61: 473–500. https://doi.org/10.1016/j.rser.2016.04.011

[14]  Gu L, Huang W, Tang S, Tian S, Zhang X, A novel deep eutectic solvent for biodiesel preparation using a homogeneous base catalyst. *Chem Eng J*. 2015; 259:647–52. https://doi.org/10.1016/j.cej.2014.08.026

[15]  Manurung R, Ramadhani DR, Maisarah S, One step transesterification process of sludge palm oil (SPO) by using deep eutectic solvent (DES) in biodiesel production. *AIP Conf Proceed*. 2017a; 1855: 070004. https://doi.org/10.1063/1.4985531

[16]  Manurung R, Winarta A, Taslim, IL, Biodiesel production from ethanolysis of palm oil using deep eutectic solvent (DES) as co-solvent. *Mater Sci Eng*. 2017b; 206: 012023. https://doi.org/10.1088/1757-899X/206/1/012023

[17]  Troter DZ, Todorović ZB, Đokić-Stojanović DR, VeselinovićLjM, Zdujić MV, Veljković VB, Choline chloride-based deep eutectic solvents in CaO-catalyzed ethanolysis of expired sunflower oil. *J Mol Liq.* 2018; 266: 557-67. https://doi.org/10.1016/j.molliq.2018.06.106

[18]  León-Reina L, Cabeza A, Maireles-Torres JRP, Alba-Rubio AC, Granados ML, Structural and surface study of calcium glyceroxide, an active phase for biodiesel production under heterogeneous catalysis. *J Catal.* 2013; 300: 30–36. https://doi.org/10.1016/j.jcat.2012.12.016

[19]  Sánchez-Cantú M, Reyes-Cruz FM, Rubio-Rosas E, Pérez-Díaz LM, Ramírez E, Valente JS, Direct synthesis of calcium diglyceroxide from hydrated lime and glycerol and its evaluation in the transesterification reaction. *Fuel* 2014; 138: 126–133. https://doi.org/10.1016/j.fuel.2014.08.006

[20]  Reyero I, Arzamendi G, Gandía LM, Heterogenization of the biodiesel synthesis catalysis: CaO and novel calcium compounds as transesterification catalysts. *Chem Eng Res Des* 2014; 92: 1519–30. https://doi.org/10.1016/j.cherd.2013.11.017

[21]  Ferrero GO, Almeida MF, Alvim-Ferraz MCM, Dias JM, Glycerol-enriched heterogeneous catalyst for biodiesel production from soybean oil and waste frying oil. *Energy Convers Manag.* 2015; 89:665–71. http://dx.doi.org/10.1016/j.enconman.2014.10.032

[22]  Lukić I, Kesić Ž, Zdujić M, Skala D, Calcium diglyceroxide synthesized by mechanochemical treatment, its characterization and application as catalyst for fatty acid methyl esters production. *Fuel* 2016; 165: 159–65. http://dx.doi.org/10.1016/j.fuel.2015.10.063

[23]  Miladinović MR, Krstić JB, Tasić MB, Stamenković OS, Veljković VB, A kinetic study of quicklime-catalyzed sunflower oil methanolysis. *Chem Eng Res Des*. 2014; 92: 1740-52. https://doi.org/10.1016/j.cherd.2013.11.023

[24]  Miladinović MR, Stamenković OS, Veljković VB, Skala UD, Continuous sunflower oil methanolysis over quicklime in a packed-bed tubular reactor. *Fuel* 2015;.154:.301-307. https://doi.org/10.1016/j.fuel.2015.03.057

[25]  Lukić I, Kesić Ž, Maksimović S, Zdujić M, Liu H, Krstić J, Skala D, Kinetics of sunflower and used vegetable oil methanolysis catalyzed by CaO·ZnO. *Fuel* 2013; 113: 367–78. https://doi.org/10.1016/j.fuel.2013.05.093

[26]  Chen X, Li Z, Chun Y, Yang F, Xu H, Wu X, Effect of the formation of diglycerides/monoglycerides on the kinetic curve in oil transesterification with methanol catalyzed by calcium oxide. *ACS Omega*. 2020; 5: 4646–4656. https://doi.org/10.1021/acsomega.9b04431

[27]  Miladinović MR, Tasić MB, Stamenković OS, Veljković VB, Skala DU, Further study on kinetic modeling of sunflower oil methanolysis catalyzed by calcium-based catalysts. *Chem Ind Chem Eng Q*. 2016; 22: 137–144 https://doi.org/10.2298/CICEQ150618027M

[28] Tasić MB, Miladinović MR, Stamenković OS, Veljković VB, Skala DU, Kinetic modeling of sunflower oil methanolysis catalyzed by calcium-based catalysts. *Chem EngTechol*. 2015; 38(9): 1550-56. https://doi.org/10.1002/ceat.201500076

# Metanoliza suncokretovog ulja katalizovana modifikovanim CaO

**Marija R. Miladinović[1], Milica Z. Petković[2], Ivana B. Banković-Ilić[2], Sandra S. Konstantinović[2] i Vlada B. Veljković[2,3]**

[1]*Poljoprivredni fakultet, Univerzitet u Nišu, Kosančićeva 4, 37000, Kruševac, Srbija*
[2]*Tehnološki fakultet, Univerzitet u Nišu, Bulevar Oslobođenja 124, 16000, Leskovac, Srbija*
[3]*Srpska akademija nauka i umetnosti, Knez Mihailova 35, 11000, Beograd, Srbija*

(Naučni rad)

*Izvod*

Metanoliza ulja u prisustvu katalizatora na bazi modifikovanog CaO proučavana je u cilju određivanja katalitičke aktivnosti novih katalizatora i definisanja odgovarajućeg kinetičkog modela. CaO je modifi-kovan komercijalnim glicerolom i eutektičkim rastvaračem (ES), holinhlorid : glicerolom (ChCl : Gly), da bi se dobili katalitički aktivni kompleksi CaO i glicerola. Cilj istraživanja bio je da se potvrdi katalitički uticaj dobijenih kompleksa na brzinu reakcije i sadržaj metilestara masnih kiselina (MEMK), a zatim opiše promena stepena konverzije triacilglicerola (TAG) sa vremenom. Na osnovu analize infracrvenom spektroskopijom sa Furijeovom (Fourier) transformacijom (engl. *Fourier Transform Infrared Spectro-scopy*, FTIR) potvrđeno je formiranje kompleksa CaO sa glicerolom i ES na bazi glicerola. Metanoliza ulja izvedena je na 60 °C pri različitim količinama katalizatora (0,5; 1 i 5 %) i molskim odnosima methanol : ulje (6 : 1, 12 : 1). Rezultati analize pokazali su da kinetički parametri dva primenjena modela zavise od količine katalizatora i molskog odnosa methanol : ulje. Oba modela se mogu uspešno primeniti za opisivanje kinetike reakcija katalizovanih kompleksima CaO sa glicerolom (srednje relativno procentualno odstupanje je manje od 10 % u oba slučaja).

# Investigating possibilities for synthesis of novel sorbents and catalyst carriers based on ceramics with controlled open porosity

**Vesna D. Nikolić[1], Jovana M. Đokić[2], Željko J. Kamberović[3], Aleksandar D. Marinković[3], Sanja O. Jevtić[3] and Zoran M. Anđić[2]**

[1]Innovation Centre of the Faculty of Technology and Metallurgy, Belgrade, Serbia
[2]Innovation Centre of the Faculty of Chemistry, Belgrade, Serbia
[3]University of Belgrade, Faculty of Technology and Metallurgy, Belgrade, Serbia

*Abstract*

The aim of this study was to investigate a possibility of synthesis of porous ceramics with controlled open porosity, which could be used as sorbents and catalyst supports. Two organic additives were used to obtain open porosity: polystyrene beads and cellulose fibers, which are mixed with kaolin clay powder and the appropriate water content. Samples were sintered at 1050 oC for 1 h. Characterization of the obtained products included X-ray powder diffraction analysis (XRPD), Fourier-transform infrared spectroscopy (FTIR), scanning electron microscopy (SEM), thermogravimetric analysis (TGA) and elemental CHNS analysis. In addition, porosity was examined by quantification of visual information. The specific surface areas were determined by the Brunauer–Emmett–Teller (BET) method. Also, density and compressive strength of the obtained samples were assessed. It was determined that by sintering, the organic component completely leaves the system. For samples prepared with polystyrene beads and with cellulose fibers, satisfactory mechanical properties were obtained: compressive strengths were 1.42 and 1.56 MPa, respectively. It was noted that significantly higher open porosity was obtained by using polystyrene beads as a sacrificial template (porosity of ~56 %) instead of cellulose fibers (porosity of ~6 %).

*Keywords:* porous sintered clay; kaolin; polystyrene; cellulose fibers.

*Available on-line at the Journal web address: http://www.ache.org.rs/HI/*

## 1. INTRODUCTION

High levels of heavy metals, metalloids, drugs, and other pollutants present in the environment may represent long-term risks to human health and ecosystems, and therefore they have to be lowered to at least maximum allowable concentrations that the World Health Organization has recommended [1]. Amongst many methods for removal of pollutants from water, adsorption technology is mostly applied due to the highest efficiency [2-4].

Porous ceramics are widely used in adsorption, but also in heterogeneous catalysis to support catalytically active substances for waste gas treatment due to high porosity and permeability to liquids, as well as high thermal stability and low density of these materials [5-13]. There are numerous methods for the synthesis of either porous solid shapes or fine particles based on ceramics such as polymer replication [10,14], modified sol-gel method [12,15], sintering of green bodies prepared from starting ceramic powders [14,16], external gelatinization [17], *etc*. For example, a suspension of polymer particles in AlF$_3$ was sintered to burn the polymer template and form reactive aluminum foam filters for the purification of molten aluminum [11]. Also, reticulated ceramic foams were prepared by dipping a polymer foam into ceramic slurry, controlled drying (60 $^o$C for 72 h then 100 $^o$C for 1 h) followed by sintering at 1250 $^o$C for 2 h resulting in foams of various shapes and broad porosity range [14]. Mesoporous γ-alumina adsorbents for heavy metal removal were synthesized by a method based on modified sol-gel, using polymethyl methacrylate microspheres as templates for obtaining mesopores, while the alumina precursor was aqueous solution of Al$_2$Cl(OH)$_5$×2.5H$_2$O. After

mixing, compressing, drying (48 h at 40 °C) and sintering at 800 °C for 5 h, highly efficient adsorbents for $Pb^{2+}$, $Ni^{2+}$ and $Cd^{2+}$ with highly ordered porosity were obtained [12]. Similarly, macroporous γ-alumina spheres were produced by an external gelatinization, sol-gel based process for potential applications as adsorbents [17]. Activated γ-alumina powder was mixed with alumina sol, medium density fibreboard (MDF) powder and chemical precipitation media to enable the sol-gel transformation. The obtained gel spheres were aged, washed, dried and calcined at temperatures from 600 to 1250 °C. The developed production method is efficient in the conservation of microporosity of the spheres, shown to be good adsorbents for $Cd^{2+}$, $Cu^{2+}$ and $Zn^{2+}$ [17]. Porous alumina was also obtained from ceramic powders without using a polymer template by mixing corundum powders with aluminum hydroxide, which decomposed during the thermal treatment, and sintering at 1000 °C for 30 min. It was concluded that the fracture strength and fracture toughness were increased compared to ceramic prepared with only corundum when 90 wt.% of $Al(OH)_3$ was mixed with corundum powder, and at the same time, highest porosity of some samples reached 62 % [16]. By described polymer foam replication or sacrificial template (polymethyl methacrylate microspheres) replication methods, desired shape and porosity of ceramics are obtained by burnout of the templates during sintering [12,18]. In addition, controlled open porosity in ceramic foams can be formed by gas bubbles, obtained by the use of foaming agents during ceramic preparation [19]. Previous studies have shown that it is possible to use NaOH as an effective foaming agent for the preparation of glass or glass-ceramic foams. Starting powders of soda lime glass were mixed with a solution of NaOH (10 wt.%) and sintered at about 750 °C in order to obtain a porosity of up to 92 % [20-23].

The aim of this study was to examine the possibility of synthesis of ceramic sorbents and / or catalyst carriers with controlled open porosity, which will provide a high degree of sorption and homogeneous precipitation of catalytically active substances, *i.e.* high catalytic activity. In order to obtain porous ceramics with a hierarchically arranged controlled open porosity, polystyrene beads and cellulose fibers were used for the first time as a sacrificial template mixed with kaolin clay powder and appropriate water content.

## 2. EXPERIMENTAL

### 2. 1. Materials and methods

In order to synthesize porous ceramic samples, the following materials were used: kaolin clay powder (99 %, Zorka Alas Kamen, Serbia), cellulose fibers (Đuraškovic Aleksej Ltd., Serbia), crosslinked polystyrene beads with phosphate groups (Lewatit® VP OC 1026, Lanxess, Germany) and demineralized water.

Kaolin clay powder had particle size of 99 % under 43 μm, and the following chemical composition: $SiO_2$ 69.20 wt.%, $Al_2O_3$ 18.90 wt.%, $Fe_2O_3$ 1.40 wt.%, $TiO_2$ 0.83 wt.%, CaO 0.42 wt.%, MgO 0.46 wt.%, $Na_2O$ 0.10 wt.% and $K_2O$ 2.89 wt.% as provided by the producer (Zorka Alas Kamen, Serbia). Polystyrene beads had particle diameter in the range from to 0.31 to 1.65 mm.

Samples with polystyrene beads (G-PS-G) were obtained by mixing beads with dry powder of kaolin clay. The content of the beads was 27 wt.% (of total weight), which corresponds to about 70 vol.% of the dry mixture. After 15 min of mixing dry components, 40 wt.% of water was slowly added, and the mixture was stirred for another 15 min by using an IKA Eurostar 20 mechanical mixer (IKA-Werke GmbH & Co., Germany) at 250 rpm until thick paste was obtained. The content of water was previously determined experimentally and that is the minimal water content needed to obtain the paste that can be stirred by a mechanical mixer at 250 rpm. The paste was then manually pressed into cylinders in gypsum molds. The obtained green samples, G-PS-G, were dried in air atmosphere for 48 h at room temperature. Slow drying was carried out in order to prevent cracking and to distribute humidity evenly in the volume of samples.

The samples with cellulose fibers as a sacrificial template (G-CV-G) were prepared under the same conditions as the samples with polystyrene. To allow mixing by a mechanical mixer at the same speed as in the G-PS-G sample, about the amount of water added was about four-fold higher. The water content was previously determined experimentally as the minimal amount that enables stirring of the paste by mechanical mixer at the specified speed. The cellulose content in the paste was 30 wt.%, and in the dry mixture it was approximately 70 %.

Green samples (G-PS-G and G-CV-G) were then removed from molds and sintered at 1050 °C for 1 h to obtain the final product (heating rate of 5 °C min$^{-1}$). The obtain samples after sintering were denoted as G-PS-S (sample with polystyrene) and G-CV-S (sample with cellulose fibers). During each synthesis, five green samples were made and subsequently sintered.

### 2. 2. Characterization

Crystallographic structure investigation (X-ray powder diffraction, XRPD) of green and sintered samples was performed by using the Roentgen diffractometer ("Philips", model PW-1710, Philips, Netherlands) with a curved graphite monochromator and a scintillation counter. Intensities of the diffracted CuK$_\alpha$ Roentgen radiation ($\lambda$ = 1.54178·10$^{-10}$ m) were measured at room temperature at 0.02° intervals of 2$\theta$, in the range 5 – 80°. The presence of the organic sacrificial templates in green and sintered samples was determined by Fourier-transform infrared spectroscopy (FTIR) using FTIR BOMEM MB series (Hartmann & Braun, country), in the range 4000-500 cm$^{-1}$ with a resolution of 4 cm$^{-1}$ in the form of KBr pellets. Thermogravimetric analysis (TGA) was performed by using a SDT Q-600 TA Instruments device (producer, country). The samples were heated in an alumina sample pan from room temperature to 700 ° C at a heating rate of 10 ° C min$^{-1}$ under nitrogen flow rate of 100 cm$^3$ min$^{-1}$. Amounts of carbon in the samples after sintering were determined by a Vario EL cube - Elementar CHNS analyzer (producer, country). The specific surface areas were determined by the Brunauer–Emmett–Teller (BET) method, using an automated gas adsorption analyzer Micrometrics ASAP 2020 (producer, country). The morphology of the sintered samples was analyzed by using a Field Emission Scanning Electron Microscope (FESEM, TESCAN MIRA 3, producer, country)). Open porosity was examined at SEM images of sintered samples by using KVI software for quantification of visual information. Density values of the sintered samples were determined from the ratio of mass and volume. Afterwards, compressive strength of disc shaped specimens with diameter of 30 mm was determined by using a servo hydraulic machine Shimadzu UH - F1000kNI (producer, country) at the piston speed of 2 mm min$^{-1}$. All analyses were performed by using minimum 5 replicate measurements.

### 3. RESULTS

Diffractograms of green (G-PS-G and G-CV-G) and sintered (G-PS-S and G-CV-S) samples are presented in Figure 1. Distinct peaks of kaolin, quartz and polystyrene or cellulose are observed in non-sintered samples. After sintering, kaolin peaks intensity decreases, the organic component completely disappears, while a phase which can be attributed to aluminum-silicon spinel appears.
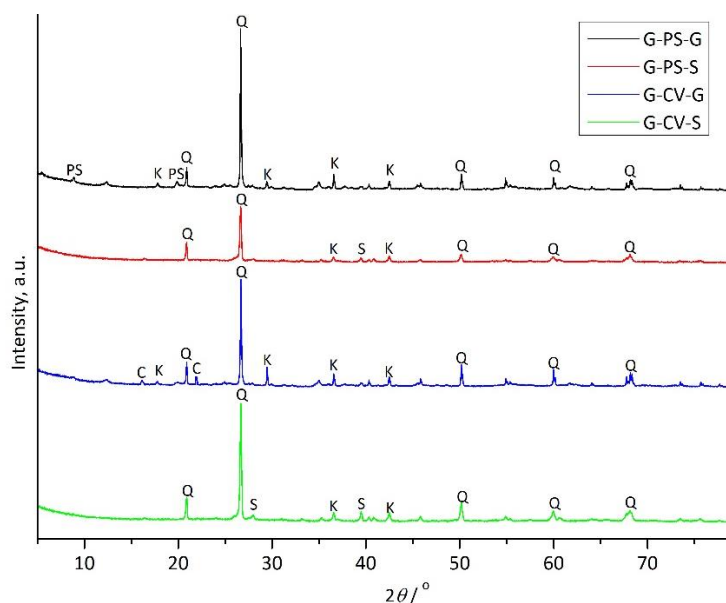


*Figure 1. XRD spectra of green and sintered samples (K – kaolinite, Q – quartz, S - aluminum-silicon spinel, PS – polystyrene, C – cellulose)*

FTIR spectra of the green and sintered samples are presented in Figures 2 and 3.
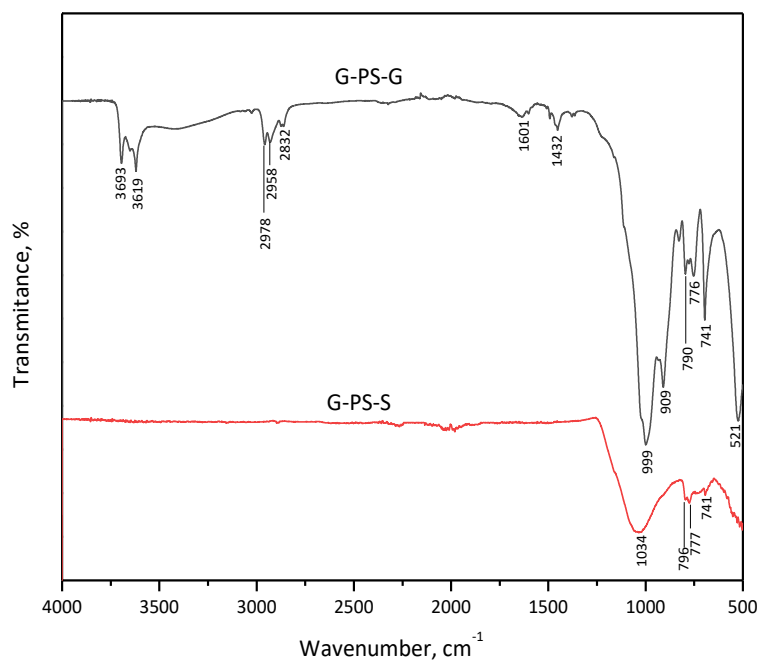


*Figure 2. FTIR spectra of green (G-PS-G) and sintered (G-PS-S) samples prepared with polystyrene beads*
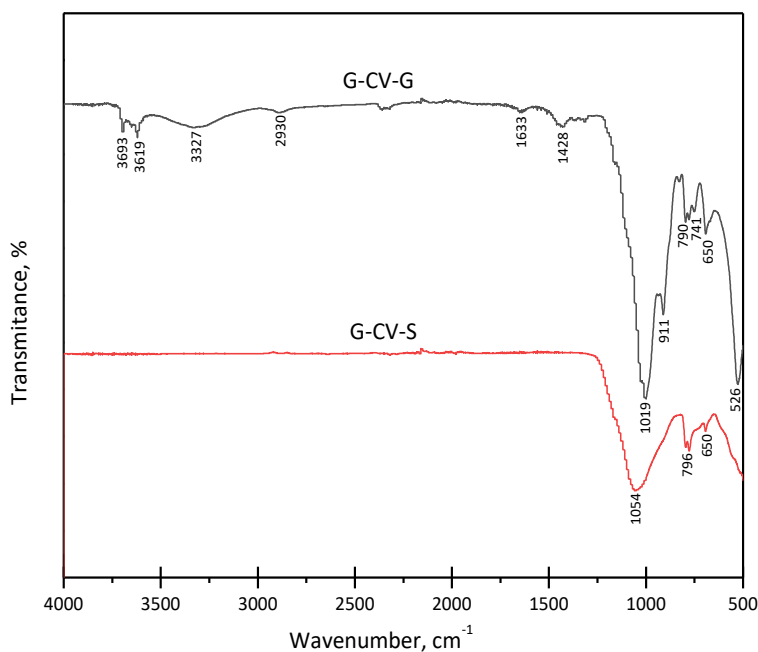


*Figure 3. FTIR spectra of green (G-CV-G) and sintered (G-CV-S) samples prepared with cellulose fibers*

The results of the TGA analysis are shown in Figure 4. The total weight loss in the sample G-PS-S was 0.44 %, while in the sample G-CV-S it was 0.31 %, which correspond to residues of organic components remaining after sintering.

The CHNS analysis has shown carbon contents of 0.13 and 0.1 wt.% in G-PS-S and G-CV-S samples, respectively.

The specific surface area of G-PS-S and G-CV-S samples was determined by the BET analysis yielding 0.33 $m^2\,g^{-1}$ for G-PS-S and less than 0.2 $m^2\,g^{-1}$ for G-CV-S.

SEM images of sintered porous ceramic samples are presented in Figure 5.
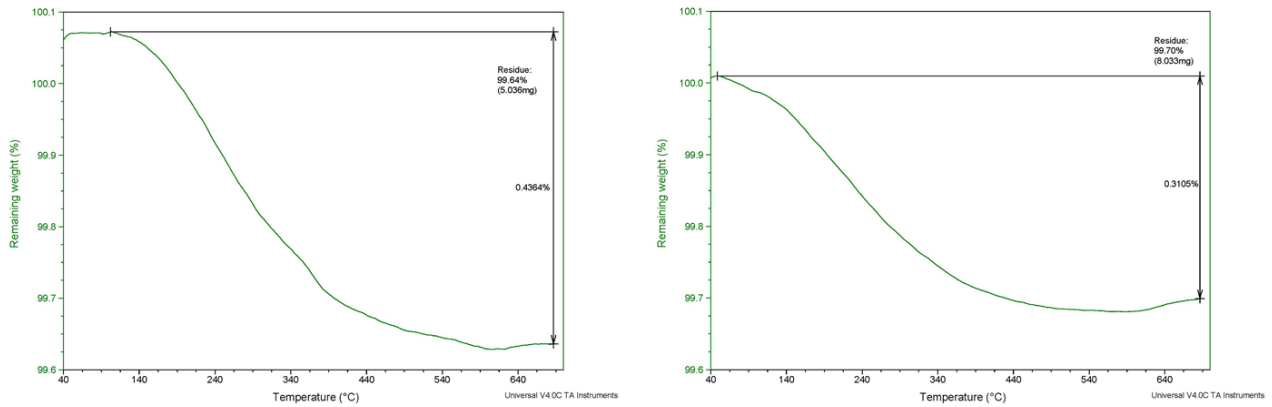
*Figure 4. Thermograms of sintered G-PS-S and G-CV-S samples*
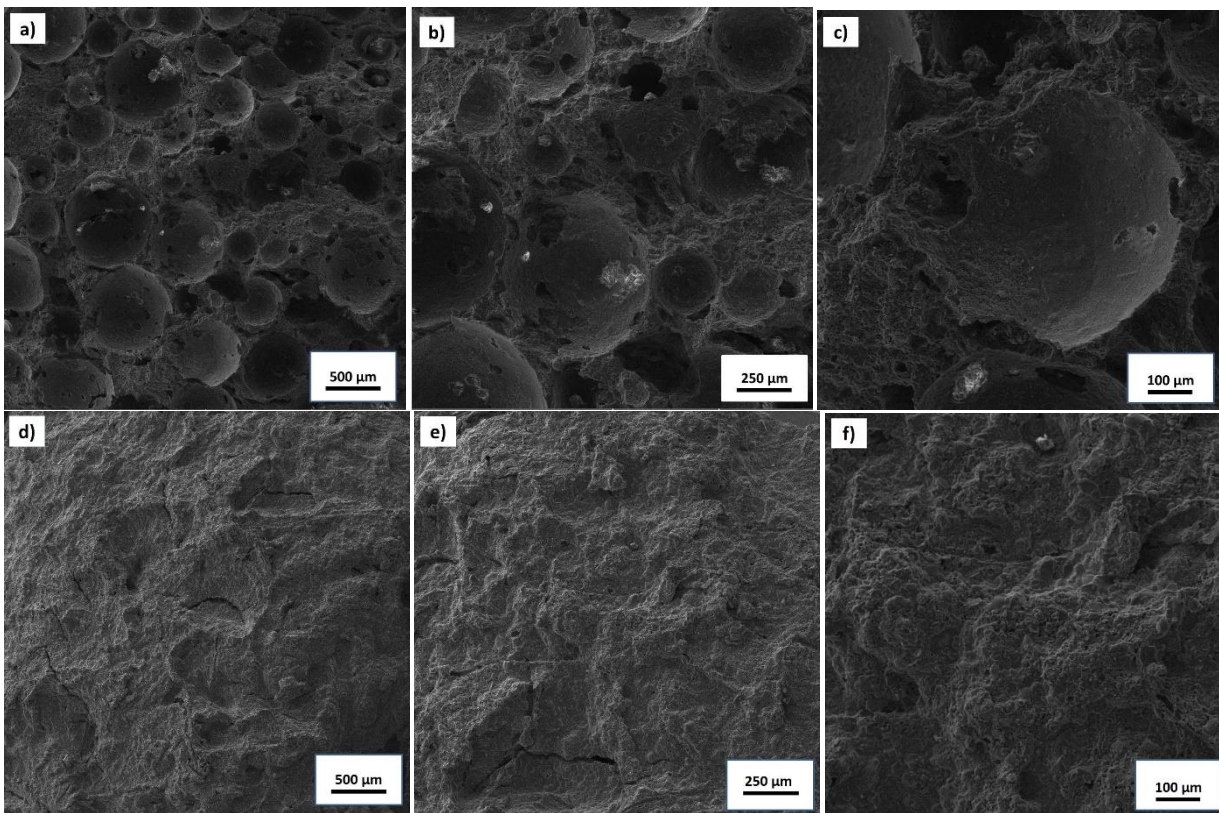


*Figure 5. SEM images of sintered porous ceramics: G-PS-S (a-c) and G-CV-S (d-f)*

Results of quantification of pore sizes and porosity of sintered samples, determined by SEM analyses and the Archimedes' method, are presented in Table 1.

*Table 1. Visual open porosity and mean pore size of sintered samples prepared with polystyrene beads (G-PS-S) and cellulose fibers (G-CV-S) determined by analyses of SEM macrographs and the Archimedes' method*

| Sample | SEM analyses | | Archimedes' met. | |
|---|---|---|---|---|
| | G-PS-S | G-CV-S | G-PS-S | G-CV-S |
| Visual open porosity, % | 56 | 6 | 59.44 | 7.72 |
| Mean pore size, µm | 340 | 5 | / | / |
| Maximal pore size, µm | 807 | 9 | / | / |
| Minimal pore size, µm | 64 | 2 | / | / |
| Standard error, µm | 29 | 1 | 0.75 | 0.02 |
| Standard deviation | 201 | 2 | 1.69 | 0.05 |

The results of the density and compressive strength tests of the sintered samples are shown in Table 2.

*Table 2. Density and compressive strength of the sintered samples prepared with polystyrene beads (G-PS-S) and cellulose fibers (G-CV-S)*

| Sample | G-PS-S | G-CV-S |
|---|---|---|
| Mean compressive strength, MPa | 1.42 | 1.56 |
| Stdandard deviation | 0.032 | 0.022 |
| Mean density, kg m$^{-3}$ | 1580 | 2210 |
| Stdandard deviation | 71.64 | 70.77 |

## 4. DISCUSSION

XRPD analyses (Fig. 1) of the green sample G-PS-G has shown that the sample contained kaolin and quartz, while peaks at the $2\theta$ = 9.5 and 19° could be attributed to polystyrene [24]. After sintering, these peaks completely disappeared, which indicates that polystyrene is not present in the system anymore, which is consistent with FTIR, TGA and elemental CHNS analyses. In the green sample G-CV-G, the main phases are also kaolin and quartz while the peaks at about $2\theta$ = 16 and 22° can be attributed to the presence of cellulose. As in the case of PS, these peaks disappear after sintering, which is in accordance with other reported analyses [25]. In both sintered samples, a decrease in the intensity of peaks originating from kaolinite is observed, which is a consequence of the formation of the aluminum-silicon spinel phase ($2\theta$ = 27 and 40°), which transforms into mullite at higher temperatures [26].

Figure 2 shows FTIR spectra of green (G-PS-G) and sintered samples (G-PS-S) prepared with polystyrene beads. The bands at 3693 and 3619 cm$^{-1}$ present in the IR spectrum of G-PS-G are related to the vibration of hydroxyl groups in kaolin, *i.e.* Si–O(H)–Al, indicating the presence of these groups before sintering. Such conclusion is corroborated with the band at 1601 cm$^{-1}$ which is assigned to the OH bending vibration. The peaks at 2978, 2958 and 2832 cm$^{-1}$ are attributed to asymmetric and symmetric stretching vibrations of the methylene group present in the PS structure. The band at 1432 cm$^{-1}$ is attributed to bending vibration of the C-H group [24].

The shoulders at 999 and 909 cm$^{-1}$ were assigned to the kaolin in-plane asymmetric Si—O—Si stretching vibration [27]. Bands at 691 and 521 cm$^{-1}$, which relate to symmetrical and asymmetrical Si—O—Si bending vibrations, respectively, describe the main vibration modes of the SiO$_4$ structure. The band pattern with peaks at 790, 776 and 741 cm$^{-1}$ correspond to Al-O-Al and Al-OH structure from Al$_2$O$_3$ overlapped with symmetrical Si-O vibration [28]. Also, in this region noticeable absorption form the PS structure, *i.e.* out-of-plane deformation vibration, was observed.

Disappearance of the bands related to polystyrene and hydroxyl group in the sintered sample indicates that the PS structure decomposes after treatment at high temperatures without residual carbonaceous material in the structure of G-PS-S. After thermal treatment of G-PS-G appearance of the peak at 1034 cm$^{-1}$ is a result of kaolin crystallization and sintering. Also, the bands at 796 and 777 cm$^{-1}$ are attributed to bonds in the quartz structure, which is in accordance with results of the XRPD analysis showing a decrease in the intensity of the peaks which belong to kaolinite [29].

Green and sintered samples prepared in the presence of cellulose fibers were also studied by using FTIR spectroscopy (Fig. 3). Similar FTIR spectra of G-CV-G and G-PS-G were obtained with exception of the peak at 3327 cm$^{-1}$ which appears due to OH stretching vibration originating from cellulose. Small band at about 2930 cm$^{-1}$ is attributed to the CH stretching vibration of hydrocarbon group in cellulose. A band at 1633 cm$^{-1}$ is associated with the bending vibration of hydroxyl groups in cellulose and hydroxyl group at the kaolinite surface, whereas the band at 1428 cm$^{-1}$ is attributed to the bending vibration of C-H group [30,31]. Vibrations at wave numbers between 500 and 650 cm$^{-1}$ are attributed to bonds in the aluminosilicate lattice of kaolin. High similarity of the spectra of G-PS-S and G-CV-S indicate similar surface functionalities and structures of both samples, which is also confirmed by the XRPD analysis. Thermogravimetric analysis (Fig. 4) confirmed that during sintering almost all amounts of polystyrene and cellulose leave the system. Presence of insignificant amounts of organic components in the sintered samples was also examined by the CHNS analysis confirming the same results obtained by the TG analysis (i.e. carbon content of 0.13 and 0.1 wt.% in G-PS-S and G-CV-S, respectively).

Specific surface areas of G-PS-S and G-CV-S samples determined by the BET analysis were low amounting to 0.33 $m^2 g^{-1}$ for G-PS-S and less than 0.2 $m^2 g^{-1}$ for G-CV-S. A small value of specific surface area of sintered kaolin-based samples it was expected [26] and is the result of the applied sintering temperature-time regime.

SEM analysis of the sample G-PS-S (Fig. 5a-c) clearly indicates the presence of particles of different sizes, having spherical shape and spongy structure. Unlike in the case of irregularly shaped particles, the spherical particle shape ensures their proper packaging during the sintering process, which is finally manifested by obtaining the final product with the required controlled porosity. Also, rough morphology of the particle surface is noticeable. The spongy structure and rough surface morphology are the result of polystyrene decomposition. Also, SEM analysis of these samples indicates that contacts were formed between individual particles. However, in some regions increase in the contact area was not observed, so that the sintering process was not complete. In accordance with the results SEM analysis, further research should be focused on optimizing the temperature-time regime of sintering.

The sample prepared with cellulose fibers (Fig. 5d-f) did not have satisfactory porosity. The pores are rare and small in diameter, which leads to the conclusion that a much higher content of cellulose fibers in the starting ceramic paste is required to obtain open porosity, while still it is uncertain if hierarchical porosity can be obtained with this material.

As presented in Table 1, the sample G-PS-S had satisfactory visual porosity of 56 %, obtained by using only 27 wt.% of polystyrene beads. The mean pore size was 340 μm. On the other hand, 30 wt.% of cellulose fibers provided visual porosity of only 6 % with the mean pore size of only 5 μm. It is obvious that the lower content of polystyrene provides significantly higher porosity.

Having in mind the SEM micrographs (Figure 3 a-c), in which particles of a regular geometric shape (spheres) are clearly visible, it could be assumed that during sintering irregularities in the particle packaging did not occur resulting in a uniform pore distribution, which significantly contributed to obtaining satisfactory mechanical properties [32, 33].

Namely, density of the sample prepared with polystyrene beads was 1580 kg $m^{-3}$ while the compressive strength reached 1.42 MPa (Table 2), which is consistent with previous research results [29]. Silicon carbide particle reinforced mullite composite foams intended for various purposes had compressive strength of 1.11 MPa at the foam density of 440 kg $m^{-3}$ [29]. Alumina foams that were synthesized for use in photocatalytic water purification had compressive strength of 0.59 MPa [33].

The obtained results show that higher, controlled porosity and satisfactory mechanical properties are achieved when polystyrene beads are used in the synthesis instead of cellulose fibers.

## 5. CONCLUSION

The goal of the present research was to investigate possibilities for synthesis novel sorbents and catalyst carriers based on ceramics with controlled open porosity. Two different sacrificial templates were mixed into starting ceramic pastes to obtain open porosity: polystyrene beads (27 wt.%) and cellulose fibers (30 wt.%). Samples were sintered at 1050 °C for 1 h. Analyses of the obtained ceramics have shown that considerably higher open porosity was formed by using polystyrene beads (56%) than by using cellulose fibers (6 %). Also, satisfactory mechanical properties were obtained: compressive strengths were 1.42 and 1.56 MPa for samples prepared with polystyrene beads and cellulose fibers, respectively. Based on the obtained results, it can be concluded that it is possible to synthesize ceramics with controlled open porosity in the presence of polystyrene beads. These materials can find their potential application as sorbents and carriers of catalytically active substances, which will be the subject of further research through optimization of relevant parameters in the synthesis process.

## REFERENCES

[1]    World Health Organization (2011) Guidelines for Drinking-water Quality, 4th edn. World Health Organization, Geneva, http://www.who.int/guidelines/en/ Accessed June 15, 2021.

[2]   Ren Y, Yan N, Wen Q, Fan Z, Wei T, Zhang M, Ma J. Graphene/δ-MnO2 composite as adsorbent for the removal of nickel ions from wastewater. *Chem Eng J.* 2011; 175: 1–7. https://doi.org/10.1016/j.cej.2010.08.010

[3]   Hadi P, Barford J, McKay G. Synergistic effect in the simultaneous removal of binary cobalt-nickel heavy metals from effluents by a novel e-waste-derived material. *Chem Eng J*, 2013; 228: 140–146. https://doi.org/10.1016/j.cej.2013.04.086

[4]   Popović A, Rusmirović J, Radovanović Ž, Milošević M. Novel method of optimized synthesis of an efficient adsorbent based on vinyl modified lignin for cadmium (II) removal. *In: Processing '19, Society for Process Engineering within SMEITS*. Belgrade, Serbia, 2019, pp. 195–201

[5]   Nikolić V, Kamberović Ž, Ranitović M, Gavrilovski M, Anđić Z. Synthesis of novel WO₃/ZrSiO₄ catalysts for dehalogenation of halogenated hydrocarbons. *Metall Mater Eng*. 2019; 25: 31-37. https://doi.org/10.30544/411

[6]   Lindon D. Montreal Protocol on Substances that Deplete the Ozone Layer, Volume 3 B, Report of the Task Force on Destruction Technologies. https://ozone.unep.org/treaties/montreal-protocol, Accessed June 15, 2021.

[7]   Pawnuk M, Grzelka A, Miller U, Sówka I. Prevention and Reduction of Odour Nuisance in Waste Management in the Context of the Current Legal and Technological Solutions. *J Ecol Eng*. 2020; 21: 34–41. https://doi.org/10.12911/22998993/125455

[8]   Cao J, Rambo CR, Sieber H. Preparation of Porous Al₂O₃-Ceramics by Biotemplating of Wood. *J Porous Mater*. 2004; 11: 163–172. https://doi.org/10.1023/B:JOPO.0000038012.58705.c9

[9]   Twigg MV, Richardson JT. Theory and applications of ceramic foam catalysts. *Chem Eng Res Des*. 2002; 80: 183–189. https://doi.org/10.1016/S0263-8762(02)72166-7

[10]  Damoah LNW, Zhang L. AlF₃ reactive Al₂O₃ foam filter for the removal of dissolved impurities from molten aluminum: Preliminary results. *Acta Mater*. 2011; 59: 896–913. https://doi.org/10.1016/j.actamat.2010.09.064

[11]  Sokić M, Kamberović Ž, Nikolić V, Marković B, Korać M, Anđić Z, Gavrilovski M. Kinetics of NiO and NiCl₂ hydrogen reduction as precursors and properties of produced Ni/Al₂O₃ and Ni-Pd/Al₂O₃ catalysts, *Sci World J*. 2015; 2015: 1-9. https://doi.org/10.1155/2015/601970

[12]  Drah A, Tomić NZ, Veličić Z, Marinković AD, Radovanović Ž, Veličković Z, Jančić-Heinemann R. Highly ordered macroporous γ-alumina prepared by a modified sol-gel method with a PMMA microsphere template for enhanced Pb²⁺, Ni²⁺ and Cd²⁺ removal. *Ceram Int*. 2017; 43: 13817–13827. https://doi.org/10.1016/j.ceramint.2017.07.102

[13]  Nikolić V, Kamberović Ž, Korać M, Anđić Z, Mihajlović A, Uljarević J. Nickel-based catalysts: Dependence of properties on nickel loading and modification with palladium. Hem Ind. 2016; 70: 137-142. https://doi.org/10.2298/HEMIND140928090N

[14]  Nor MAAM, Akil HM, Ahmad ZA. The effect of polymeric template density and solid loading on the properties of ceramic foam. *Sci Sinter*. 2009; 41: 319–327. https://doi.org/10.2298/SOS0903319N

[15]  Niesz K, Yang P, Somorjai GA. Sol-gel synthesis of ordered mesoporous alumina. *Chem Commun*. 2005; 1986–1987. https://doi.org/10.1039/b419249d

[16]  Deng ZY, Fukasawa T, Ando M, Zhang GJ, Ohji T. Microstructure and Mechanical Properties of Porous Alumina Ceramics Fabricated by the Decomposition of Aluminum Hydroxide. *J Am Ceram Soc*. 2001; 84: 2638–2644. https://doi.org/10.1111/j.1151-2916.2001.tb01065.x

[17]  de Faria CLL, de Oliveira TKR, dos Santos VL, Rosa CA, Ardisson JD, de Almeida Macêdo WA, Santos A. Usage of the sol-gel process on the fabrication of macroporous adsorbent activated-gamma alumina spheres, *Microporous Mesoporous Mater*. 2009; 120: 228–238. https://doi.org/10.1016/j.micromeso.2008.11.008

[18]  Nikolić V, Kamberović Ž, Anđić Z, Korać M, Sokić M. Synthesis of α-Al₂O₃ based foams with improved properties as catalyst carriers. *Materiali in Tehnologije*, 2014; 48: 45–50. http://mit.imt.si/izvodi/mit141/nikolic_v.pdf

[19]  Binner J, *Ceramic foams, Cellular ceramics: Structure, Manufacturing, Properties and Applications*. WILEY-VCH Verlag GmbH & Co. KGaA, Wienheim; 2005.

[20]  Bento AC, Kubaski ET, Sequinel T, Pianaro SA, Varela JA, Tebcherani SM. Glass foam of macroporosity using glass waste and sodium hydroxide as the foaming agent. *Ceram Int*. 2013; 39: 2423-2430. https://doi.org/10.1016/j.ceramint.2012.09.002

[21]  da Silva RC, Kubaski ET, Tenório-Neto ET, Lima-Tenório MK, Tebcherani SM. Foam glass using sodium hydroxide as foaming agent: Study on the reaction mechanism in soda-lime glass matrix. *Journal Non-Cryst*. Solids, 2019; 511: 177-182. https://doi.org/10.1016/j.jnoncrysol.2019.02.003

[22]  da Silva RC, Kubaski ET, Tebcherani SM. Glass foams produced by glass waste, sodium hydroxide, and borax with several pore structures using factorial designs. *Int J Appl Ceram Technol*. 2019; 17: 75-83. https://doi.org/10.1111/ijac.13210

[23]  Yatsenko EA, Goltsman BM, Klimova LV, Yatsenko LA. Peculiarities of foam glass synthesis from natural silica-containing raw materials. *J Therm Anal Calorim*. 2020; 142: 119–127. https://doi.org/10.1007/s10973-020-10015-3

[24]  Wankasi D, Dikio ED. Comparative Study of Polystyrene and Polymethylmethacrylate Wastes as Adsorbents for Sorption of Pb²⁺ from Aqueous Solution. *Asian J Chem.* 2014; 24: 8295-8302. http://dx.doi.org/10.14233/ajchem.2014.16809

[25]  Ishak WHW, Ahmad I, Ramli S, Amin MCIM. Gamma Irradiation-Assisted Synthesis of Cellulose Nanocrystal-Reinforced Gelatin Hydrogels. *Nanomaterials*. 2018; 8: 749-762. http://dx.doi.org/10.3390/nano8100749

[26]  Milheiro FAC. Freire MN. Silva AGP. Holanda JNF. Densification behaviour of a red firing Brazilian kaolinitic clay. *Ceram Int*. 2005; 31: 757–763. http://dx.doi.org/10.1016/j.ceramint.2004.08.010

[27]  Castellano M, Turturro A, Riani P, Montanari T, Finocchio E, Ramis G, Busca G, 2010. Bulk and surface properties of commercial kaolins, *Appl. Clay Science*. 2010; 48: 446–454. http://dx.doi.org/10.1016/j.clay.2010.02.002

[28] Hlavay J, Jonas K, Elek S, Inczedy J, Characterization of the particle size and the crystallinity of certain minerals by IR spectrophotometry and other instrumental methods-II. investigations on quartz and feldspar, *Clays and Clay Minerals*. 1978; 26: 139-143. https://doi.org/10.1346/CCMN.1978.0260209

[29] Deju R, Mazilu C, Stanculescu I, Tuca C, Fourier transform infrared spectroscopic characterization of thermal treated kaolin, *Rom Rep Phys*. 2020; 72: 1-11. http://www.rrp.infim.ro/2020/AN72806.pdf

[30] Poletto M, Ornaghi HL, Zattera AJ. Native Cellulose: Structure, Characterization and Thermal Properties. *Mater*. 2014; 7: 6105-6119. https://doi.org/10.3390/ma7096105

[31] Hospodarova V, Singovszka E, Stevulova N. Characterization of Cellulosic Fibers by FTIR Spectroscopy for Their Further Implementation to Building Materials, *AJAC*. 2019; 9: 303-310. http://dx.doi.org/10.4236/ajac.2018.96023

[32] Akpinar S, Kusoglu IM, Ertugrul O, Onel K. Silicon carbide particle reinforced mullite composite foams, *Ceram Int*. 2012; 38: 6163-6169. https://doi.org/10.1016/j.ceramint.2012.04.067

[33] Plesch G, Vargova M, Vogt UF, Gorbar M, Jesenak K. Zr doped anatase supported reticulated ceramic foams for photocatalytic water purification, *Mat Res Bull.* 2012; 47: 1680-1686. https://doi.org/10.1016/j.materresbull.2012.03.057

# Ispitivanje mogućnosti sinteze inovativnih sorbenata i nosača katalizatora na bazi keramike kontrolisane otvorene poroznosti

**Vesna D. Nikolić[1], Jovana M. Đokić[2], Željko J. Kamberović[3], Aleksandar D. Marinković[3], Sanja O. Jevtić[3] i Zoran M. Anđić[2]**

[1]*Inovacioni centar Tehnološko-metalurškog fakulteta, Beograd, Srbija*
[2]*Inovacioni centar Hemijskog fakulteta, Beograd, Srbija*
[3]*Univerzitet u Beogradu, Tehnološko-metalurški fakultet, Beograd, Srbija*

(Naučni rad)

*Izvod*

Cilj ovog rada je ispitivanje mogućnosti sinteze porozne keramike sa kontrolisanom otvorenom poroznošću, koji se mogu koristiti kao sorbenti i nosači katalizatora. Dva organska dodatka su korišćena za dobijanje otvorene poroznosti: perle od polistirena i celulozna vlakna, pri čemu su bili pomešani sa prahom kaolinske gline i odgovarajućim količinama vode. Uzorci su sinterovani na 1050 ᵒC tokom 1 h. Karakterizacija dobijenih proizvoda obuhvatala je rendgensku difrakciju praha, infracrvenu spektroskopiju sa Furijeovom transformacijom, skenirajuću elektronsku mikroskopiju (SEM), termogravimetrijsku (TGA) analizu i elementnu CHNS analizu. Pored toga, poroznost je ispitivana kvantifikacijom vizuelnih informacija sa SEM mikrografija. Specifične površine su određene BET (engl. Brunauer–Emmett–Teller) metodom. Takođe, kod dobijenih uzoraka ispitane su gustina i čvrstoća na pritisak. Utvrđeno je da sinterovanjem organska komponenta u potpunosti izlazi iz sistema. Za uzorke pripremljene sa polistirenskim perlama i sa celuloznim vlaknima dobijene su zadovoljavajuće mehaničke karakteristike: čvrstoće na pritisak su bile 1,42 i 1,56 MPa, redom. Primećeno je da je značajno veća poroznost dobijena korišćenjem polistirenskih kuglica kao žrtvene faze (~56%) u odnosu na celulozna vlakana (~6%).

# Effects of production conditions on the properties of limestone briquettes aimed for acid soil liming

**Vladimir Jovanović[1], Dragana Nišić[2], Vladimir Milisavljević[2], Dejan Todorović[1], Dragan Radulović[1], Branislav Ivošević[1] and Sonja Milićević[1]**

*[1]Institute for Technology of Nuclear and Other Mineral Raw Materials, Belgrade, Serbia*
*[2]University of Belgrade, Faculty of Mining and Geology, Belgrade, Serbia*

*Abstract*

This paper presents the results of experiments performed to determine how the quantity of the binder (bentonite) and the parameters of the laboratory roll press affect the quality of the briquettes obtained from limestone powder. These experiments aim to examine the conditions in which limestone briquettes are formed and to determine their use for agricultural purposes. During the experiments various mass fractions of bentonite was added to limestone (from 1 to 10 %), while the force of roll press drums ranged from 2 to 25 kN. The briquettes have been tested by applying scanning electron microscopy (SEM), differential thermal and thermo-gravimetric (DTA/TG) analyses, X-ray diffraction (XRD) and Fourier-transform infrared spectroscopy (FTIR). Bentonite distribution was found to be uniform within the compact briquette structure. Formation of new compounds was not evidenced. The experiments also demonstrated that during briquetting, limestone properties remain unchanged, the changes are only physical, water solubility is not reduced, mechanical properties (impact resistance, compressive strength and abrasion resistance) are satisfactory by the transport and storage terms if the binder mass fraction is over 5% and the briquetting force exceeds 10kN and finally there is no loss due to wind dispersal during application. The only downside of the "green" briquettes obtained is the time required for their complete disintegration if totally immersed in water.

*Keywords:* bentonite; briquette roll press; green briquette; briquette properties.

*Available on-line at the Journal web address: http://www.ache.org.rs/HI/*

## 1. INTRODUCTION

Limestone, a salt of calcium and carbonic acid, is a naturally occurring mineral [1]. It appears throughout the world and it is crucial raw material used in various industries [2]. As reported, there are approximately 300 various applications of limestone and further on, processed limestone is a base for numerous other products [3]. One of them is the limestone use for agricultural purpose to adjust the soil acidity.

In low pH environments, abutment of heavy metals is dissolved and released to the soil, which can be toxic to plants [4-5]. Acidity of the soil (pH) has an impact on availability of most heavy metals [6]. Liming efficiently improved soil chemical composition [7]. Limestone is commonly applied for treatment of acidic soils in agriculture and forestry to boost yield and product quality [8]. Soil acidity reduction and higher levels of ex-changeable Ca and Mg was achieved during a ten-year soil liming field experiment, by treating the soil with powdered limestone and finally resulting in higher green grain yield [9-11].

Calcium-oxide (CaO) is a compound with greatest impact on the limestone quality [3]. By adding CaO into soil, the heavy metal-induced toxicity is significantly reduced, and the yield is increased. After treating the soil with limestone, calcium reacts with carbon dioxide and water from the soil, depositing Ca and Mg carbonates. Further on, this triggers a reaction with the acidic colloidal complexes, where Ca and Mg are replacing hydrogen and Al. These reactions produce

emission of carbon dioxide and higher pH value of the soil to a satisfactory level [12]. By increasing the soil pH metal mobility is reduced so that limestone can be designated as a stabilization agent [13-17].

In agricultural application, limestone should be sufficiently fine as to be dissolved by the effects of weathering and spread evenly on the soil. However, problems arise during transportation and handling when this powdery material is easily dissipated and dispersed by wind from land surface. Thus, it is necessary to consolidate the powdered limestone, to meet both requirements. Common approaches are pelletizing and briquetting, resulting in suitable material size, easy for transport, handling, and use [18]. Pelletized nutrition is already used for application of urea. Experiments with urea briquettes pointed to significantly ($p < 0.05$) increased grain yields, nitrogen uptake, and nitrogen recovery compared to broadcast urea [19].

Briquettes can be produced by high load compaction, during which a bulk solid is transformed into a new structure with physical properties different from the original ones [20]. It is desired to control agglomeration of powdered materials in order to improve physical properties such as density, homogeneity, strength, compressive strength, shape, appearance, etc., and increase product quality [18]. The required values are determined by standards, norms or needs and demands of individual customers. Which method of agglomeration will be chosen depends on the type of material and on the target properties of the agglomerate; pelletizing (agglomeration by rotation), briquetting (agglomeration by pressure) or sintering (agglomeration by thermal treatment) [18,21].

The technologically simplest methods for limestone briquette formation have been the matter of extensive studies and presented in numerous literary sources [18,21,22]. The most important parameter for agglomeration strength is adhesion force between the particles that form the agglomerate [24] and different adhesion mechanisms have been studied [25]. Since the adhesion forces may differ, with sufficiently large separating forces (*e.g.* elastic reactive forces, current or frictional or impact forces) the formation of agglomerates is possible only when these, adhesion forces, are sufficiently greater than the separating ones [26]. Therefore, briquettes are dried to achieve the necessary strength. Usually, the quality of produced briquettes is in relation to their application (testing properties are shape, size, strength, porosity, and surface area) [27].

The main aim of this work was to examine conditions for production of limestone briquettes with the addition of bentonite as a binder and to determine adequacy of their use for agricultural purposes. Tests were conducted on the assumption that bentonite, as a highly viscous binder will not produce negative effects on the soil quality as confirmed in literature [26,28]. Briquetting conditions were investigated with the goal to form briquettes of the same structure and solubility as the initial crushed limestone, and that will not be prone to dispersal and loss during application, while exhibiting mechanical properties adequate for transport and storage. In addition, the tests aimed at production of "green" briquettes. The term ''green'' briquettes is used to indicate that the resulting material does not contain ingredients that are harmful to the environment, i.e., the resulting briquettes should be eco-friendly.

## 2. MATERIALS AND METHODS

### 2. 1. Briquette production

For experimental tests, a limestone sample was taken from the lithothamnium limestone deposit at the Dobrilovic Site near Loznica (Serbia). Bentonite, composed predominantly of the mineral smectite and originating from the Sipovo Deposit (Bosnia and Herzegovina) was used as a binder.

A series of detailed tests were performed with crushed lithothamnion limestone to examine the briquette forming conditions. The tests were conducted in three phases:

- Phase 1 - forming briquettes with different binder mass fractions and applying different briquetting forces,
- Phase 2 – determining limestone structural changes when transformed into briquettes,
- Phase 3 – examining other limestone properties essential for liming acid soils. Each testing phase was conditioned by the positive results of the previous phase.

Briquetting was performed with the B050 Laboratory Roller Press (Komarek, US) with specifications as follows: roll diameter - 100 mm, roll width - 38 mm, roll speed – variable from 0 to 7,5 rpm, roll separating force – variable up to 50 kN, feed screw speed – variable up to 137 rpm, variable throughput up to 20 kg h$^{-1}$, total power installed – 1.4 kW.

The briquetting process was conducted by applying different forces (in the range of 2, 5, 10, 15, 20 and 25 kN) and different binder contents (in the range of 1; 2.5; 5 and 10 %), while keeping constant the other process and press parameters. The initial amount of each sample (limestone) was 500.0 g. Different amounts of binder (bentonite) were added, in the range of 1; 2.5; 5 and 10 % related to the initial amount of the limestone. The roller press itself contains a vessel with a mixer that serves to uniformly distribute the binder within the material. Limestone and the binder are first added to that vessel which provided mixing until the mixture was completely homogenized. During the homogenization process, water was continuously added up to a maximum of 10 % related to the total sample amount. Then the homo-genized sample was transferred *via* a screw conveyor to the press section in which the sample was briquetted. Once the so-called "green" briquettes were withdrawn from the press they were left in air for the next 24 h. Following this method, 24 sets of briquettes were made each with different (combined) characteristics (the briquetting force and the binder content).

Briquette groups obtained under extreme conditions were selected for characterization: briquettes formed with the lowest binder content (1 %) and at applying the lowest force (2 kN) and briquettes formed with the highest binder content (10 %) and at applying the highest force (25 kN).

## 2. 2. Briquette characterization

### 2. 2. 1. Thermal analysis

The STA 409 EP (Netzsch, Germany) was used for differential thermal and thermo gravimetric analysis (DTA, TG). The samples were thermally treated in air atmosphere, in a temperature range 20 to 1000 $^{o}$C, at a heating rate of 10 $^{o}$C min$^{-1}$. The sample α-Al$_2$O$_3$ was used as reference sample.

### 2. 2. 2. Fourier transform infrared spectroscopy

Infrared spectroscopic tests were performed with the Nicolet IS-50 (Thermo-Fisher Scientific, US). The attenuated total reflectance (atr) technique was used for measurements in the range between 4000 and 400 cm$^{-1}$ with 32 scans at a resolution of 4. After completed measurements it was necessary to make two corrections: the atmospheric correction for the removal of gas signals ($CO_2$ and $H_2O$) and automatic baseline correction.

### 2. 2. 3. X-ray diffraction analysis

A PW1710 X-Ray Diffractometer (Philips, Netherlands) with curved-graphite monochromator and scintillation counter was used to monitor the phase composition of the samples applying X-ray diffraction analysis.

### 2. 2. 4. Scanning electron microscope analyses

Scanning electron microscope (SEM) analyses were performed with the JSM-6610LV Scanning Electron Microscope (Jeol, Japan) equipped with INCA Energy Dispersive X-Ray Spectrometer (EDS).

### 2. 2. 5. Impact resistance

Impact resistance was tested on a set of 10 briquettes each having a total weight of 100 g. Impact resistance testing was performed by 25 consecutive releases of the briquette sample from the height of 457 mm on a steel plate 9-mm thick, after which the briquette sample was sieved on a 2-mm mesh screen and the mass of screen undersize was weighed [29]. This means that the mass of broken briquette particles lower than 2 mm in size is weighted. The results are presented as a mass percentage with respect to the initial sample mass and should not exceed 10 % of the total initial weight.

### 2. 2. 6. Compressive strength

Compressive strength was tested on a group (set) of 10 pellets on a laboratory press (Tonindustrie, Germany), to determine the maximum pressure that the pellet can withstand without breaking. These tests were performed according to the procedure of the company Mars Minerals (US), which is a designer and manufacturer of agglomeration equipment and systems and has been the pioneer in this field [29], which recommended that pellets should withstand a minimum of 0.5 kg / pellet, considered satisfactory for further manipulation.

### 2. 2. 7. Abrasion resistance

Abrasion resistance was tested by sieving a group of pellets weighing 100 g each on a mechanical laboratory sieving device Analysette 3 (Fritsch, Germany) using a sieve of appropriate mesh size (depending on the tested size class) for a period of 5 min. After that, the mass of the screen undersize that arise due to mechanical abrasion is determined, which should not exceed 5% of the total mass of the sample.

### 2. 2. 8. Disintegration

Briquette disintegration (complete disintegration) time when immersed in water at room temperature was tested by placing 3 briquette samples from each group into water. The disintegration is determined visually.

### 2. 2. 9. Limestone solubility

Solubility tests were performed to determine the solubility of various limestone products in water and to determine the possible impact of agglomeration processes on the solubility process. The following were used in the tests: analytical balance, platinum cups, water bath, laboratory oven and hotplate. The experiment is performed by dissolving 6.0000 g (weight) of the sample in 100 cm$^3$ of hot distilled water and cooking for 1 min. When the suspension has cooled, the solution was separated from the precipitate by squeezing through a filter paper (blue tape). Two tests were performed for each sample. Platinum cups are dried at 105 °C in an oven and cooled in a desiccator for 1 h and measured to constant weight ($m_1$). 50 cm$^3$ of the solution is poured into a platinum cup (which mass is stable), evaporated in a water bath, and then the platinum cup is dried in an oven at 105 °C, cooled for 1 h in a desiccator and measured on the analytical balance to constant mass ($m_2$). Thus, the difference in two measured mass values presents the sample fraction soluble in water. After the measurement, the mass percentage of the fraction soluble in water ($S_{H_2O}$) is determined according to the equation (1):

$$S_{H_2O} = \frac{2(m_2 - m_1)}{6000}100 \qquad\qquad (1)$$

where $m_1$ and $m_2$ are masses expressed in g.

### 2. 2. 10. Wind dispersal

Tests of the influence of wind on the distribution of materials of 2 different limestone products were performed, *i.e.* limestone powder and briquettes.

Three 100-g samples taken from each group (limestone powder and limestone briquette) were, at different wind speeds of 1, 3 and 5 m s$^{-1}$ uniformly discharged from a height of 60 cm to a 50×70 cm container, for a period of 4 minutes per each test. Wind was simulated by the axial fan type A.B.V.E - 3.5 (capacity 3600 m$^3$ h$^{-1}$, 780 rpm) (Tvornica ventilacijskih uređaja, Croatia) and wind speed was measured using anemometer CFM Metal Vane Anemometer SN: Q617422 (Extech, US). After every test the weight of the material from the container was measured. During each test the weather elements were also measured: temperature and humidity were measured by using the sensor ST-321S (Standard Instruments, China) and air pressure was measured by using Barolux A 9896 (R. Fuess Berlin-Steglitz, Germany).

## 3. RESULTS AND DISCUSSION

Limestone in the form of briquettes, used for testing is shown in Figure 1.
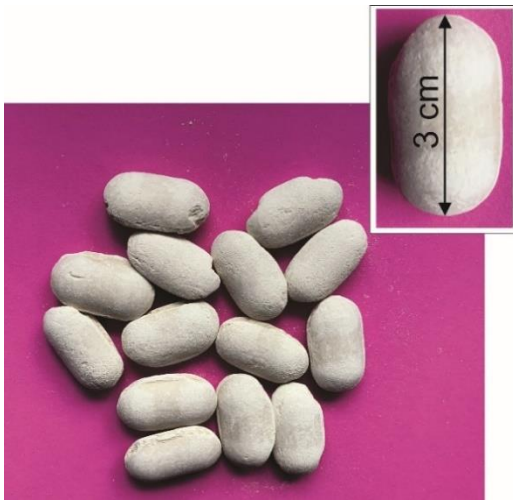


*Figure 1. Limestone briquettes*

To produce a usable briquette, limestone must not undergo any changes that might disturb its structure or hinder its ability to raise the alkalinity of soil. For characterization, we selected the briquette groups obtained under extreme conditions – briquettes formed with the lowest binder content and by applying the lowest force (1 % of bentonite at 2 kN) and on briquettes formed with the highest binder content at the highest force (10 % of bentonite at 25 kN). The briquettes were analysed by applying SEM, DTA/TG and FTIR analyses to determine possible changes in the structure.

The results of scanning electron microscopy (SEM) analysis are shown in Figure 2, which comparatively presents the SEM micrographs of samples at different magnifications. Despite the large difference in the binder mass fraction, the SEM micrographs do not reveal any difference between the two sample groups. This can be explained by the fact that the initial material is fine-grained, and the sample is well homogenized with the binder.

DTA curves of briquettes with different bentonite contents are shown in Figure 3a, which presents typical limestone peaks without major displacements. With the higher bentonite content, the peak intensity typical for limestone gradually decrease. Due to the low bentonite content and considerably lower peak intensity, typical bentonite peaks were not detected. Also, results of TG analyses (Figure 3b) indicate negligible difference in mass as compared to the initial limestone sample. The reason for this finding is a relatively low mass fraction of bentonite. From the TG diagram it can be observe that there is insignificant mass loss in the temperature range up to 100 $^{\circ}$C, which corresponds to the water loss. These results indicated that after the drying process the remaining moisture content in briquettes is around 1 wt.%.

The results shown in Figure 3 are indicating that the application of bentonite as a binder in limestone briquetting at various mass fractions does not have an impact on the briquette thermal properties in comparison to the initial limestone sample.

Figure 4 shows the results of the infrared spectroscopy analysis (FTIR).

As shown in Figure 4 in the infrared spectra of briquette samples, in addition to the spectral lines characteristic for limestone, with unchanged intensities and positions, it is possible to observe bands typical for bentonite at 993 cm$^{-1}$ whose intensity increases with higher bentonite content. The absence of either new spectral lines or major displacements of positions typical for spectral bands in the spectra of the analyzed samples (Fig. 4), indicate that the structural properties of the initial samples have not changed [30].

The results of all shown tests are confirming sufficient homogenization of bentonite and limestone, without any impact of the process (briquetting) and binder on limestone structural properties. These facts confirm that the briquettes can be equally successful for liming acid soils as limestone powder or limestone lumps and can be used interchangeably.
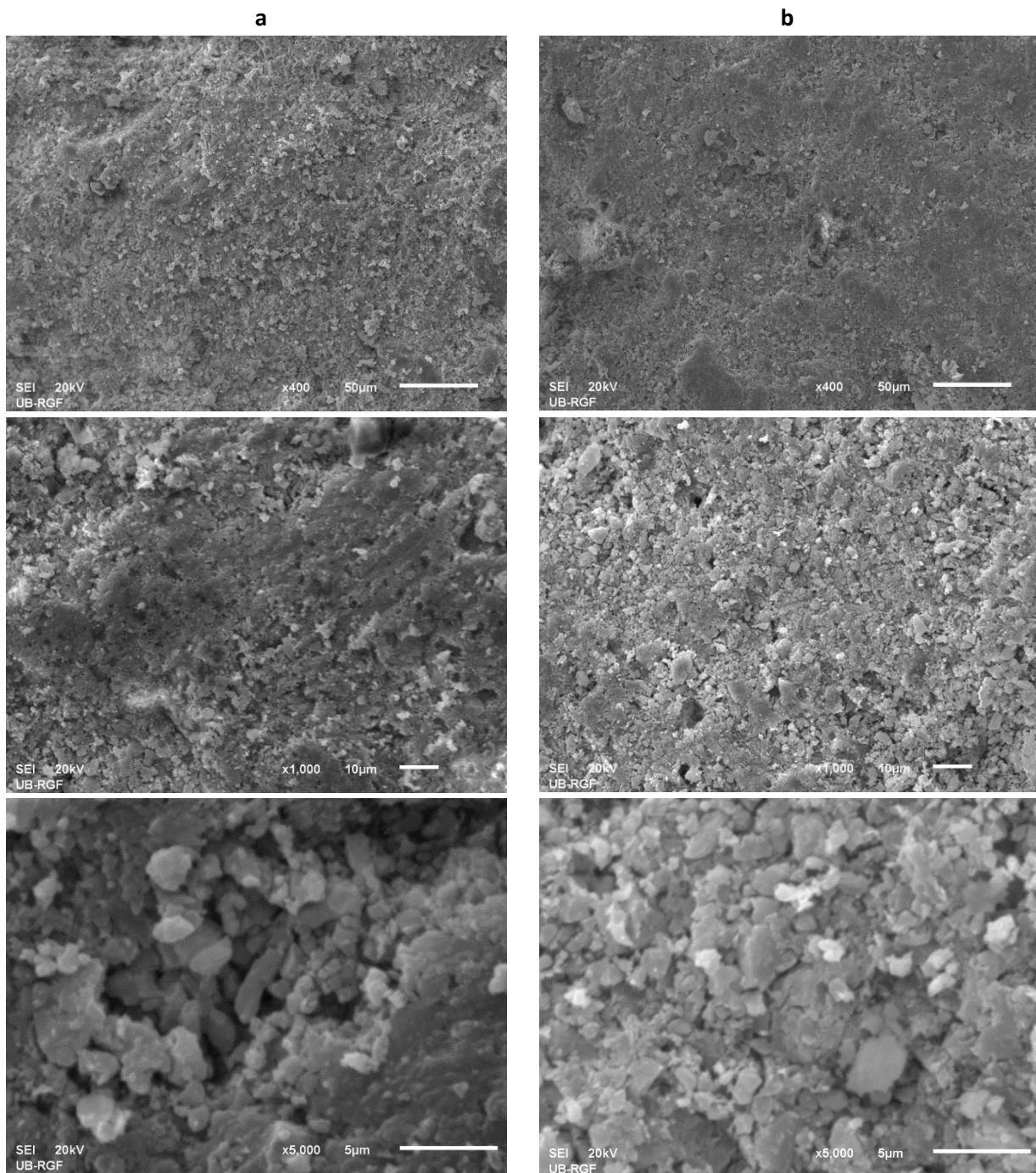
*Figure 2. SEM micrographs of briquette samples: (a) with the lowest binder content (1 %) at the minimum briquetting force (2 kN) and (b) with the highest binder content (10 %) at the maximum briquetting force (25 kN), at different magnifications*

For the agricultural use, it is important that briquettes retain the initial solubility of crushed limestone. Soluble content of powdered limestone and briquettes with 1 % of the binder obtained at 2 kN force was 0.12 %, while it was 0.128 % for briquettes with 10 % binder obtained at 25 kN force. According to these results, limestone maintained excellent solubility, which was not disturbed in the briquetting process.

For briquette handling it is important to determine how it behaves when fully submerged in water. This is determined by measuring the time needed to obtain the complete disintegration of the briquette. From the results presented in Figure 5, it is evident that the time of disintegration is longest at the lowest binder content. Therefore, the swelling property of bentonite reduces the strength of the links between limestone grains.
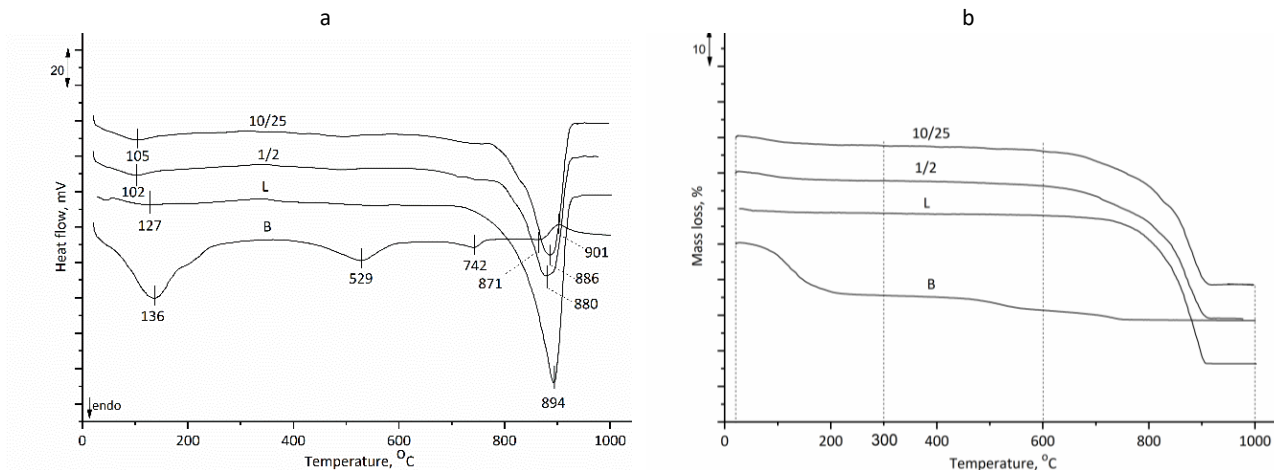
*Figure 3. DTA (a) and TG (b) results for: bentonite (B), limestone (L) and briquette samples 10/25 (produced with 10 % binder under 25 kN force) and 1/2 (produced with 1 % binder under 2 kN force)*
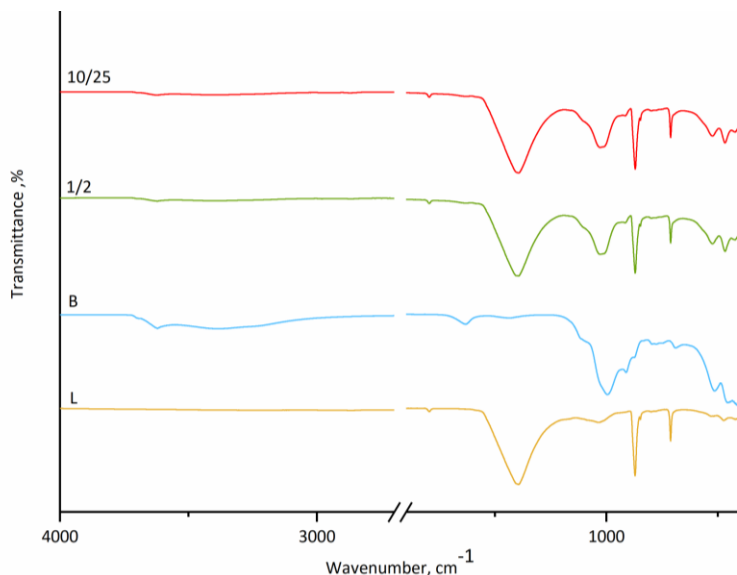


*Figure 4. Infrared spectra of bentonite (B), limestone (L) and briquette samples 10/25 (produced with 10 % binder under 25 kN force) and 1/2 (produced with 1 % binder under 2 kN force)*
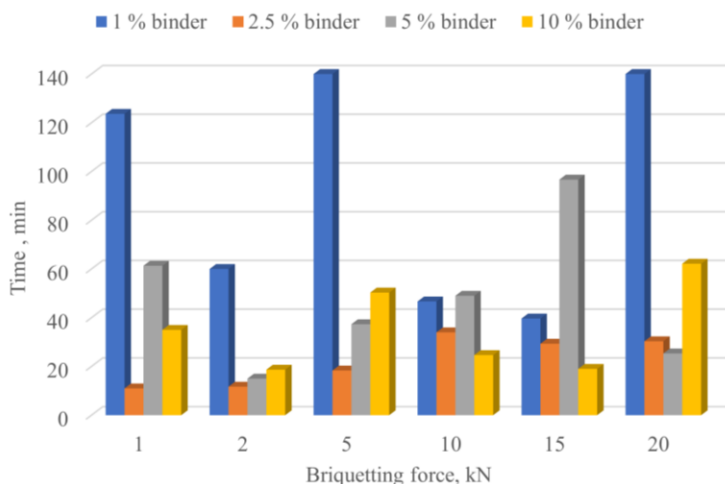


*Figure 5. Time required for complete disintegration of briquettes with different binder contents obtained at different briquetting forces submerged in water*

The results of mechanical tests of "green" briquettes are shown in Figure 6. Standard mechanical properties were tested such as: impact resistance, compressive strength, and abrasion resistance [29]. According to authors dealing with briquette quality issue mechanical durability is main indicator of briquette mechanical quality [14,21,27,31]. The company Mars Minerals (USA), proficient in agglomeration of limestone, has provided the literature data that was used as a baseline for determining the fulfillment of conditions [29].
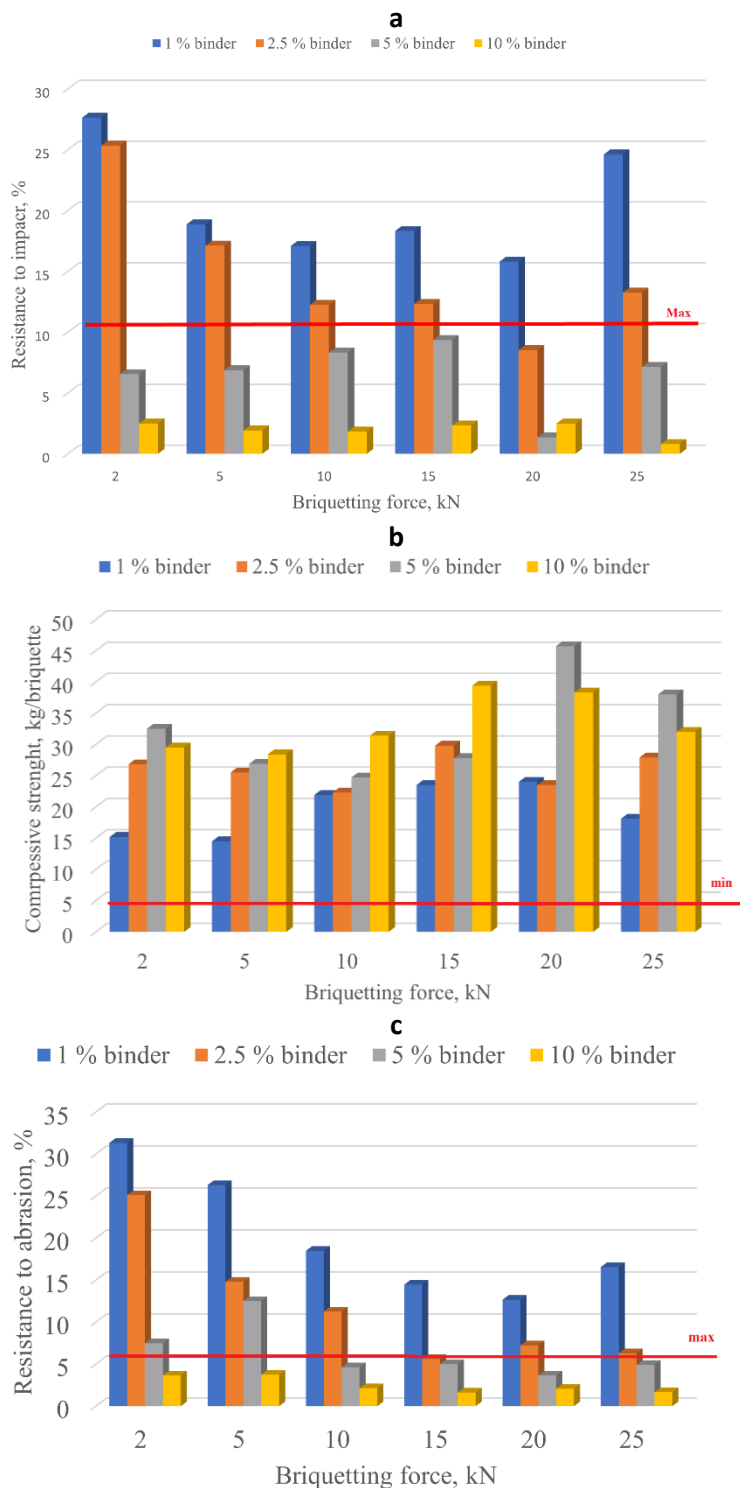


Figure 6. Mechanical properties of "green" briquettes with different binder contents and obtained under different briquetting forces: (a) impact resistance, (b) compressive strength according to the procedure in [29], (c) resistance to abrasion

The obtained mechanical properties of the "green" briquettes (Fig. 6) indicate that the impact resistance depends more on the binder mass content than on the briquetting force. The binder mass content is a relevant parameter for achieving suitable briquette abrasion resistance, but the force at which the briquette is formed is equally important. Briquettes with 1 and 2.5 % binder contents show satisfactory resistance to compression, but unsatisfactory resistance to abrasion and impact. Briquettes with 5 % binder obtained at briquetting forces above 10 kN and briquettes with 10% binder meet all resistance criteria.

The overall results show that the briquettes demonstrate better mechanical properties if the binder mass fraction is higher and generally if formed at higher briquetting forces. Separately, the best results are achieved with a 10 % binder mass content at 15 kN briquetting force, however from the practical point of view, the most economical briquetting procedure implies the use of 5 % binder content at the force of 10 kN. Considering that herein "green" briquettes were the object of investigation, it can only be assumed that after drying, even the briquettes with 2.5 % binder content, formed at the briquetting force ranging from 10 to 15 kN will be acceptable, since it is reasonable to expect that drying will increase the briquette resistance to impact and abrasion.

However, regarding the disintegration time in water, only the samples with low binder mass content showed satisfactory properties, irrespective of the briquetting force applied.

Table 1 shows results obtained by examining the effects of wind on material dispersal for briquettes and limestone powder for comparison. Air temperature was 20 $^{\circ}$C, air humidity was 35 % and air pressure was 1001 mbar in the moment of testing. Tests at higher wind speeds than 5 m s$^{-1}$ were not performed since it is considered unreasonable to apply limestone in stronger winds.

*Table 1. Test results for determining the effects of wind on material dispersal*

| Product | Limestone powder | | | Limestone briquette[1] | | |
|---|---|---|---|---|---|---|
| Wind speed, m/s | 1 | 3 | 5 | 1 | 3 | 5 |
| The weight of the sample before the test, g | 1000 | 1000 | 1000 | 1000 | 1000 | 1000 |
| The weight of the sample after the test, g | 640 | 470 | 370 | 1000 | 1000 | 1000 |
| Weight loss, % | 36 | 53 | 63 | 0 | 0 | 0 |

[1]Briquette sample was the 50-50 mixture of 10/25 and 1/2 samples

Briquettes have also shown superior properties in wind dispersal tests, as expected, as compared to the powdered material, which was significantly lost at the increasing wind speed (for 36-63 %, Table 4), while it did not induce briquette dispersal. The obtained results showed that it is possible to produce stable "green" briquettes with different binder mass fractions and applying different briquetting forces.

## 5. CONCLUSIONS

This paper presents the results observed during briquette formation from lithothamnium limestone by adding bentonite. The criteria for determining the quality of "green" briquettes are defined as: unchanged structure and function of limestone, unchanged water solubility, mechanical properties follow the recommendations of the company Mars Minerals and there is no loss during application to the soil. The conducted tests have shown that during briquetting, limestone properties remain unchanged, and all the changes are limited to physical characteristics. According to this we can conclude that during the agglomeration process the binding of the starting material occurred due to the physical and not chemical adsorption. This fact helps us, from the scientific point of view, to better understand the processes that occur during the agglomeration of limestone with the bentonite as a binding agent. Additionally, water solubility is not reduced, the briquettes have satisfactory mechanical properties when binder mass fraction is over 5 % and the briquetting force exceeds 10 kN and finally there is no loss due to wind dispersal during application.

The only downside of so produced "green" briquettes is related to the time required for their complete disintegration if totally immersed in water, (*e.g.* if there is a flood in the limestone briquette warehouse). In such conditions the bentonite starts swelling and briquettes with generally good mechanical properties, quickly lose their shape and disintegrate completely. Given the results, it is evident that the briquetting process should be completed by

introdu**c**ing drying, which would transform the "green" briquettes into hardened briquettes that should have even better mechanical properties.

## REFERENCES

[1]    Oh S, Hyun CU, Park HD. Near-Infrared Spectroscopy of Limestone Ore for CaO Estimation under Dry and Wet Conditions. *Minerals* 2017; 7(10): 193 https://doi.org/10.3390/min7100193

[2]    Carvalho EAD, Brinck V, Campos ARD, Campos VRD. *Aglomeração. Parte I: Briquetagem*, 5th ed, Comunicação Técnica elaborada para o LivroTratamento de Minérios, Rio de Janeiro, 2010; 683-750 (in Portuguese)

[3]    Lee H, Kim K, Kim J, You K, Lee H. Breakage Characteristics of Heat-Treated Limestone Determined via Kinetic Modeling. *Minerals* 2018; 8(1): 18 https://doi.org/10.3390/min8010018

[4]    McLaughlin MJ, Zarcinas BA, Stevens DP, Cook N, Soil testing for heavy metals. *Communications in Soil Science and Plant Analysis* 2000; 31(11-14): 1661-1700 https://doi.org/10.1080/00103620009370531

[5]    McLaughlin MJ, Hamon RE, McLaren RG, Speir TW, Rogers SL. A bioavailability-based rationale for controlling metal and metalloid contamination of agricultural land in Australia and New Zealand. *Soil Research* 2000; 38(6): 1037-1086 http://dx.doi.org/10.1071/SR99128

[6]    Karalic K, Loncaric Z, Popovic B, Zebec V, Kerovec D. Liming effect on soil heavy metals availability. *Poljoprivreda* 2013; 19(1): 59-64.

[7]    Parecido RJ, Soratto RP, Perdona MJ, Gitari HI, Dognani V, Santos AR, Silveira L. Liming Method and Rate Effects on Soil Acidity and Arabica Coffee Nutrition, Growth, and Yield. *Journal of Soil Science and Plant Nutrition*, 2021; 21: 2613–2625 https://doi.org/10.1007/s42729-021-00550-9

[8]    Boyd CE. Use of agricultural limestone and lime in aquaculture. *CAB Reviews* 2017; 12 (015): 1-10 http://dx.doi.org/10.1079/PAVSNNR201712015

[9]    Cifu M, Qinglin F. Changes in chemical properties of red soil after surface application of powdered limestone, *Acta Pedologica Sinica* 1995; 3

[10]   Haque F, Chiang YW, Santos RM. Alkaline Mineral Soil Amendment: A Climate Change 'Stabilization Wedge'?. *Energies* 2019; 12(12): 2299  https://doi.org/10.3390/en12122299

[11]   Renforth P, Manning DAC, Lopez-Capel E. Carbonate precipitation in artificial soils as a sink for atmospheric carbon dioxide. *Applied Geochemistry* 2009; 24(9): 1757-1764 http://dx.doi.org/10.1016/j.apgeochem.2009.05.005

[12]   [12] Milic S. Soil Fertility on Privately Owned Lands in Various Agricultural Production Regions of Vojvodina, *In: Proceedings of 45th Symposium on Agriculture*, Zlatibor, Serbia, 2001; Available online: www.nsseme.com /about /inc /SAS /45SAS/2011-02-04/3%Milic.pdf

[13]   Silva AC, Silva EMS, de Barros MR, Marinho DY. Limestone fines reuse for agriculture through briquetting, *Tecnologiaem Metalurgia, Materiais e Mineração* 2016; 13(4): 365-372 http://dx.doi.org/10.4322/2176-1523.1147

[14]   Brožek M, Study of briquette properties at their long-timestorage. *J. For. Sci.* 2013; 59(3): 101-106. https://doi.org/10.17221/27/2012-JFS

[15]   Yun SW, Yu C. Immobilization of Cd, Zn, and Pb from Soil Treated by Limestone with Variation of pH Using a Column Test, *Journal of Chemistry* 2015; 2015: Article ID 641415, 8 pages, https://doi.org/10.1155/2015/641415

[16]   Lim JM, You Y, Kamala-Kannan S, Oh SG. Oh B-T. Stabilization of Metals-contaminated Farmland Soil using Limestone and Steel Refining Slag, *J. Soil Groundw. Environ.* 2014; 19 (5): 1~8.  DOI: http://dx.doi.org/10.7857/JSGE.2014.19.5.001

[17]   Sekulic Ž, Mihajlovic S, Kašic V, Cosic V, Liming Acid Soils Using Lithothamnium Limestone. *In: Proceedings of Natural Mineral Resources and the Possibility of their Use in Agriculture and Food Industry*, Belgrade, Serbia, 2006, pp. 113-123.

[18]   Silva CA, Barros MR, Silva MSE, Marinho YD, Lopes FD, Sousa ND, Tomaz SR. Limestone briquette Production and Characterization. *Inter. Journal of Environmental, Chemical, Ecological, Geological and Geophysical Engineering*. 2016; 10 (10): 1006-1012.

[19]   Siddique IA, Mahmud AA, Hossain M, Islam MR, Gaihre YK, Singh U. Movement and Retention of NH4-N in Wetland Rice Soils as Affected by Urea Application Methods. *Journal of Soil Science and Plant Nutrition*, 2020; 20 (2):589-597. http://dx.doi.org/10.1007/s42729-019-00148-2

[20]   Cabiscol R, Shi H, Wünsch I, Magnanimo V, Finke JH, Luding S, Kwade A. Effect of particle size on powder compaction and tablet strength using limestone, *Advanced Powder Technology*, 2020;31 (3):1280-1289. http://dx.doi.org/10.1016/j.apt.2019.12.033

[21]   Pietsch W. *Agglomeration Processes – Phenomena, Technologies, Equipment*; Wiley-VCH Verlag GmbH: Weinheim, Germany, 2001.

[22] Zhou HY, Zhou JM, Peng HY, Deng SX. Experiment Study of Preparation Process of Limestone-Upright-Furnace Briquette, *Coal Technology* 2005; 12.

[23] Jovanovic VD, Kneževic DN; Sekulic ŽT, Kragovic MM, Stojanovic JN, Mihajlovic SR, Nišic DD, Radulovic DS, Ivoševic BB, Petrov MM. Effects of bentonite binder dosage on the properties of green limestone pellets. *Chem. Ind.* 2016; 10: 135-144 http://dx.doi.org/10.2298/HEMIND160210023J

[24] Gluba T. The Effect of Wetting Conditions on the Strength of Granules. *Physicochem. Probl. Miner. Process.* 2006; 36(1): 233-242.

[25] Sastry KVS, Fuerstenau DW. Kinetics of Green Pellet Growth by the Layering Mechanism. *Transactions of AIME.* 1977; 262: 43–47.

[26] Nicol SK, Adamiak ZP. Role of Bentonite in Wet Pelletizing Processes. *Trans. IMM.* 1973; 82: C26-C33.

[27] M. Petrovic, Mineral Processing – Fundamentals of Agglomeration, PhD dissertation Faculty of Mining, Geology and Civil Engineering: Tuzla, Bosnia and Herzegovina; (2008) p. 288.

[28] Waters PL. Briquette Binders, A Reappraisal, *In: Proceedings of the 12th Biennial Conference of the Institute for Briquetting Agglomeration*, Institute for Briquetting and Agglomeration, Vancouver, Canada, 1971, pp. 145-159.

[29] Albert KB, Langford D. *Pelletizing Limestone Fines*, Mars Mineral, Pennsylvania. 1998; pp. 12-29.

[30] Orolínová Z, Mockovciaková A, Dolinská S, Briancin J, Effect of thermal treatment on the Bentonite properties. *Arhiv za tehnicke nauke.* 2012; 7(1): 49-56. http://dx.doi.org/10.5825/afts.2012.0407.049O

[31] Brunerova A, Ivanova A, Brozek M, Mechanical durability of digestate briquettes mixed with mineral additives. *In: Proceedings Engineering for rural development*. Jelgava, Latvia, 2016, pp. 971-976.

# Korelacija uslova dobijanja i kvaliteta briketa krečnjaka za upotrebu u kalcizaciji kiselih zemljišta

**Vladimir Jovanović[1], Dragana Nišić[2], Vladimir Milisavljević[2], Dejan Todorović[1], Dragan Radulović[1], Branislav Ivošević[1] i Sonja Milićević[1]**

[1]Institut za tehnologiju nuklearnih i drugih mineralnih sirovina, Beograd, Srbija
[2]Univerzitet u Beogradu, Rudarsko-geološki fakultet, Beograd, Srbija

(Naučni rad)

*Izvod*

U radu su prikazani rezultati eksperimenata koji su sprovedeni da bi se utvrdilo kako količina veziva (bentonita) i parametri laboratorijske valjkaste (rol) prese utiču na kvalitet briketa dobijenih od krečnjačkog praha. Ovi eksperimenti imaju za cilj ispitivanje uslova u kojima se formiraju briketi krečnjaka i utvrđivanje mogućnosti njihove upotrebe u poljoprivredi. U toku eksperimenata krečnjaku su dodavani različiti maseni udeli bentonita (od 1 do 10 %), dok se sila valjaka prese kretala od 2 do 25 kN. Briketi su analizirani primenom skenirajuće elektronske mikroskopije (SEM), diferencijalno termičkih analiza (DTA/TG) i infracrvene spektroskopije sa Furijeovom (Fourier) transformacijom (FTIR). Utvrđena je ravnomerna distribucija bentonita, kao i kompaktnost briketa, bez stvaranja novih jedinjenja. Eksperimenti su takođe pokazali da tokom briketiranja svojstva krečnjaka ostaju nepromenjena, promene su samo fizičke, rastvorljivost u vodi nije smanjena, mehanička svojstva (otpornost na udar, čvrstoća na pritisak i otpornost na abraziju) su zadovoljavajuća prema uslovima transporta i skladištenja, ako je maseni udeo veziva preko 5 % i sila briketiranja prelazi 10 kN i, konačno, nema gubitaka usled rasprščivanja vetrom tokom nanošenja. Jedini nedostatak dobijenih „zelenih" briketa je vreme koje je potrebno za njihovu potpunu dezintegraciju ako su potopljeni u vodu.

*Ključne reči:* bentonit; briketiranje; rol-briket presa; zeleni briket; osobine briketa

107

# Determination of silicon dioxide content in bauxite: comparing the ICP-OES method with the UV-VIS method

**Gordana S. Ostojić[1], Dragica Z. Lazić[2] and Saša M. Zeljković[3]**

*[1]Factory "Alumina" Ltd, Karakaj bb, 75 400 Zvornik, Bosnia and Herzegovina*
*[2]University of East Sarajevo, Faculty of Technology Zvornik, Karakaj bb, 75 400 Zvornik, Bosnia and Herzegovina*
*[3]University of Banja Luka, Faculty of Science, Department of Chemistry, 2 Mladena Stojanovica, 78 000 Banja Luka, Bosnia and Herzegovina*

*Abstract*
In this paper, the ICP-OES method (induced coupled plasma optical emission spectrometry) was used to determine the content of silicon dioxide in bauxite, as an important impurity that affects the quality and application of bauxite in alumina production by the Bayer process. Twenty bauxite samples from seven different deposits were analysed. The results were compared with the reference spectrophotometric UV-VIS method. The mean relative difference between the silicon dioxide content determined by the ICP-OES method and the reference method is found to be 4.88 %. Statistical tests were used to assess the comparability of the two methods, followed by a scatter plot, the Bland Altman, Passing-Bablok, and the "Mountain" plot. Graphical comparisons generally do not show statistically significant differences between methods. The accuracy and precision of the ICP-OES method were verified by using the standard reference material SRM NIST 697, Dominican Bauxite. Recovery and repeatability values, expressed as relative standard deviation (RSD), are within the acceptance criteria. Based on the t-test, there is a statistically significant difference between the mean value of ICP-OES measurements and the certified value of silicon dioxide, which can be attributed to the effect of systematic error of ICP-OES analysis.

*Keywords:* impurities; sample preparation; precision; X-ray analysis; alumina.

*Available on-line at the Journal web address: http://www.ache.org.rs/HI/*

## 1. INTRODUCTION

Bauxite is the most important aluminium ore presently serving as a source of almost the entire world production of alumina and aluminium. Bauxites are a complex multi-component raw material with the basic components being the minerals of aluminium, iron, silicon, titanium, calcium, and magnesium [1]. The quality of bauxite and the choice of process parameters are determined by the content of impurities in addition to the percentage content of $Al_2O_3$ and the mineral form in which it is found. Silicon occurs in bauxite in the form of clay minerals of kaolinite and halosite ($Al_2O_3 \cdot 2SiO_2 \cdot 2H_2O$) and quartz $SiO_2$ [2]. The presence of $SiO_2$ in bauxite in the form of chamosite $4FeO \cdot Al_2O_3 \cdot 3SiO_2 \cdot 4H_2O$ [3] is also possible. Based on these facts, for the assessment of bauxite quality in laboratory conditions, methods for fast, accurate, and precise characterization of bauxite are extremely important. In numerous papers, different methods have been used to quantify silicon and other impurities in bauxite, such as spectrophotometry [4,5], X-ray fluorescence (XRF) [4], *Fourier transform infrared spectroscopy* (FTIR) [1], and laser-induced plasma spectroscopy (LIBS) [6,7]. Combinations of LIBS, energy-dispersive X-ray *spectroscopy (EDS)*, X-ray diffraction (XRD), and *scanning electron microscopy* (*SEM*) [8] methods were used for the chemical-mineralogical analysis of high silicate bauxite. The previously frequently used gravimetric method, is not practical for the silicon dioxide determination [3] as it is time-consuming. Although it is a more expensive analysis compared to most of the others, the method of inductively coupled plasma emission spectrometry (ICP-OES) [9,10] is increasingly used. The advantages of this method are low detection limit,

stability and reproducibility of excitation sources, efficient atomization, speed of analysis, wide dynamic range, and the possibility of multi-element analysis.

This study aimed to evaluate the possibility of using the ICP-OES method as an alternative method for the determination of silicon dioxide in bauxite, by comparing the results with the reference spectrophotometric method and the use of a standard reference material. The used method of sample preparation was the same as for the spectrophotometric method, therefore not requiring additional time or material consumption.

## 2. EXPERIMENTAL

### 2. 1. Materials, standard solutions and reagents

Twenty bauxite samples from several different deposits from Bosnia and Herzegovina (Milići, Posušje, Jajce, Srebrenica, Široki Brijeg and Mrkonjić Grad) and from Montenegro (Nikšić) were analyzed. A standard bauxite sample SRM NIST 697, Dominican bauxite (National Institute of Standards and Technology, USA), was used to assess the accuracy and precision of the ICP-OES method.

All chemical reagents used were of analytical grade: sodium carbonate anhydrous, CAS 497-19-8 (Merck KGaA, Germany), sodium tetraborate decahydrate, CAS 1330-43-4 (Merck KGaA, Germany), ammonium molybdate tetrahydrate, CAS 12054-85-2 (LobaChemie PVT, Mumbai, India), ascorbic acid, CAS 50-81-7 (LobaChemie PVT, Mumbai, India), monoelement ICP standard silicon solution of 1000 mg dm$^{-3}$ (Certipur Merck, KGaA, Germany), Specto Genesis ICAL solution (Bernd Kraft GmbH, Germany), HCl acid 37 % (m/m), CAS 7647-01-0 (Zorka Pharma, Šabac, Serbia) and H$_2$SO$_4$ acid 96 % (*m/m*), CAS 7664-93-9 (Zorka Pharma, Šabac, Serbia). Argon gas purity of 5.0. (99.999 %), CAS 7440-37-1 (Messer, B&H) was used for ICP-OES analyses. A standard solution concentration of 0.04 g dm$^{-3}$ SiO$_2$ for spectrophotometric measurements was prepared from powdered SiO$_2$ *p.a.*, CAS 60676-86-0 (Fisher Scientific, Germany). Ultrapure water (resistance 18 MΩ cm$^{-1}$) was used for all analyses.

### 2. 2. Methods and instruments

2. 2. 1. Determining the silicon dioxide content by the ICP-OES method

The concentration of silicon dioxide was determined by using the ICP-OES spectrometer SPECTRO GENESIS, Spectro Analytical Instruments GmbH, Kleve, Germany in radial plasma mode. Calibration, measurements and data processing were performed by using the Smart Analyzer Vision 5.0 software package, which also served to record and control the instrument itself. Disassembly torch with 1.8 mm diameter Al$_2$O$_3$ injector, nebulizer, and spray chamber is adapted to work with HF. The continuous flow of the sample was achieved by using a peristaltic pump. The power of the radiofrequency generator was 1400 W, the flow rate of the cooling gas 12 dm$^3$ min$^{-1}$, the flow rate of the nebulizer gas 0.90 dm$^3$ min$^{-1}$, and the flow rate of auxiliary gas 0.90 dm$^3$ min$^{-1}$.

All laboratory glassware used for quantification of the silicon oxide content by the ICP-OES method was previously immersed in 10 % (v/v) HNO$_3$ for 24 h, washed with high purity distilled water, and dried with dry air at room temperature. Set-up method, ICALization (Intelligent Calibration and Logic) of the optical system of the ICP-OES spectrometer, calibration and measurement of control samples were performed according to the appropriate instructions [11].

The following equipment was used for sample preparation: VIMS Elektrik dryer (Tršić, Serbia) with a maximum temperature of 200 °C, analytical balance Entris (Sartorius, Germany with the precision of 0.1 mg, annealing furnace up to 1100 °C and laboratory stove (ELEKTRON, Banja Koviljača, Serbia), pipettes and burettes of AS class and other common glass laboratory accessories. Ultrapure water (resistance 18 MΩ cm$^{-1}$) for all analyses was provided by using the Milli-Q Reference system, Merck Millipore, Germany.

2. 2. 2. Measurements by the reference method

Analysis of the ICP-OES results were performed with respect to the spectrophotometric method MA.BM.006, following the method "VAMI" St. Petersburg and JUS B.G8.518 (ISO 6607). Spectrophotometric analysis was performed

by using a double-beam UV-VIS spectrophotometer Shimadzu UV 1800 (Shimadzu, Japan) with UV Probe software. The pH value was measured by using a Five Esay pH meter (Mettler Toledo, Germany).

Silicon is characterized by the formation of a yellow silicomolybdate complex under strictly controlled conditions of acidity, reagent concentration, temperature, and time. The addition of ascorbic acid in the sulphuric acid environment reduces the resulting complex to a blue colour. The absorbance of this coloured complex was measured at 810 nm and the results were calculated and related to the calibration curve in the $SiO_2$ concentration range of 0.4-2.8 mg dm$^{-3}$.

### 2. 2. 3. Mineralogical characterization of samples

Qualitative mineralogical characterization of bauxite samples was performed by X-ray diffraction using a powder diffractometer D8 ENDEAVOR Minerals (BRUKER, Germany), under the following conditions: radiation of cobalt anticathode wavelength CoK$\alpha$ = 0.178897 nm, current and voltage of the generator 35 mA and 40 kV, respectively, angular range 10-90° 2$\theta$, variable divergent slit, step size 0.02°, step time 1 s. Interpretation of diffractograms was performed by using the software package EVA.DIFRAC (BRUKER, Germany) with an integrated database.

## 2. 3. Sample preparation

Bauxite samples were homogenized, dried at 105 °C, and ground to a particle size below 200 μm. For both methods the samples were prepared in the same way, by melting with a mixture $Na_2CO_3$: $Na_2B_4O_7$ in a ratio of 3:1 and by dissolving the molten mass in hydrochloric acid (1:3), according to the method MA.BM.004, and modified methods JUS B.G8. 520/92 and ISO 6994/86. The bauxite specimen mass of 1 g was mixed with 6 g of $Na_2CO_3$:$Na_2B_4O_7$ mixture (3:1) in a Pt-crucible. Sodium tetraborate decahydrate, $Na_2B_4O_7 \cdot 10$ $H_2O$, was previously annealed for two hours at 400 °C, after which it was cooled and ground to powder. The sample with the mixture was melted in a covered crucible at 1000 °C for 30 min. The molten mass was dissolved in 60 cm$^3$ of HCl 1: 3, taking care not to boil. The solution was transferred to a normal 500 cm$^3$ vessel, filled up to the mark with water, and well homogenized. The prepared samples were analysed by spectrophotometry and ICP-OES methods, at appropriate dilutions. For the ICP-OES analysis samples were diluted 10 times. The blank probe was prepared in the same way, but without a sample, and measured with each series of samples. Three samples of each bauxite specimen were prepared for the analyses. To assess accuracy and precision, the standard bauxite specimen SRM NIST 697 was prepared in the same way and measured ten times.

## 2. 4. Statistical processing

Microsoft Excel with the Analysis ToolPak (Microsoft, US) and MedCalc Statistical Software version 19.3.1 (MedCalc Software Ltd, Ostend, Belgium) were used for statistical data processing. The scatter plot, Bland Altman, Passing-Bablok, and "Mountain" plots were used to process and display the data obtained by the two analytical methods.

Bland Altman difference plots are used to describe agreement between two quantitative measurements by constructing limits of the agreement. These statistical limits are calculated by using the mean and the standard deviation of the differences between two measurements (SD). Bland-Altman recommended that 95 % of the data points should lie within ± 1.96 SD of the mean difference. The normal distribution of the differences must always be verified. If the line of equality (differences=0) is not in the confidence interval for the mean, the bias between the two measurements is statistically significant [12].

The Passing-Bablok regression is a linear regression model that assumes that neither of the two variables is either dependent or independent. The result is presented through a graphical representation of the value of the intercept and the slope, with a confidence interval that indicates the existence of a constant or proportional difference between the measurement results [13].

A "Mountain" plot is a complementary plot to the difference plot. It shows the distribution of differences between the two methods with an emphasis on the center and the tails of the distribution [14].

The measurement uncertainty according to the certified $SiO_2$ value was calculated based on the European Reference Materials [15].

## 3. RESULTS AND DISCUSSION

Diffractograms of bauxite samples from the seven deposits and of the standard bauxite sample are shown in Figures 1-7. According to the results of the X-ray analysis, the Milići, Jajce, Nikšić, Srebrenica, Široki Brijeg and Mrkonjić Grad bauxite deposits are of boehmite type, while bauxite from the Posušje deposit is of the mixed boehmite-gibbsite type. In addition to boehmite (AlOOH) and gibbsite (Al(OH)$_3$), the samples contain hematite (Fe$_2$O$_3$), goethite (FeOOH), kaolinite (Al$_2$O$_3$ ·2SiO$_2$ ·2H$_2$O), anatase (TiO$_2$), rutile (TiO$_2$), calcite (CaCO$_3$), and quartz (SiO$_2$). The bauxite from Jajce deposit also contains a small amount of diaspore (AlOOH). Silicon dioxide (SiO$_2$) is predominantly present in the form of kaolinite. Within bauxite obtained from Milići (samples 2 and 3), Posušje (samples 1 and 3), and Srebrenica (samples 1, 2 and 3), apart from kaolinite, there was also a certain amount of quartz. The standard bauxite sample NIST 697, Dominican bauxite [16] is a gibbsite type with a boehmite content of up to 10 %. Apart from gibbsite and boehmite, this bauxite contains hematite, goethite, kaolinite, anatase and calcite.
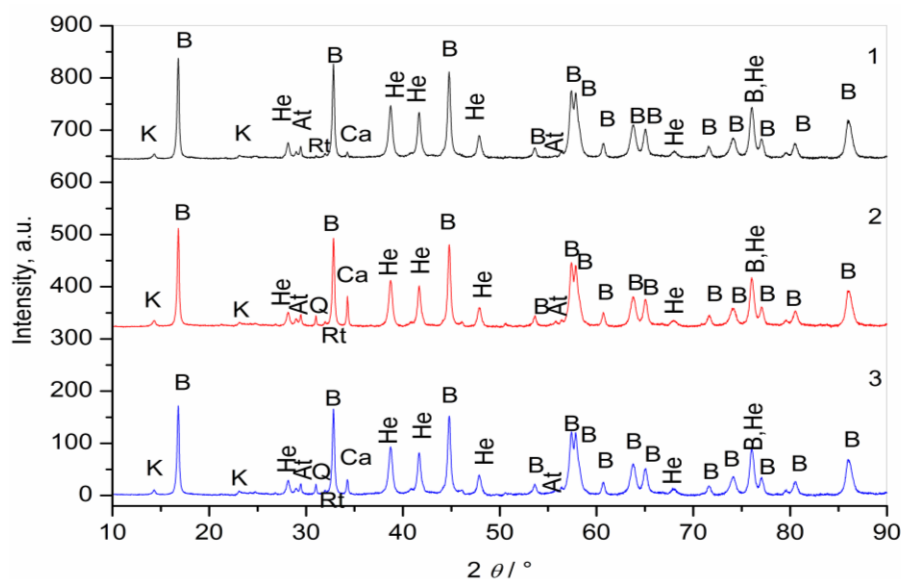


*Figure 1. Diffractogram of the bauxite samples Milići (1-3): B-boehmite, He-hematite, At-anatase, Rt-rutile, Ca-calcite, Q-quartz and K-kaolinite*
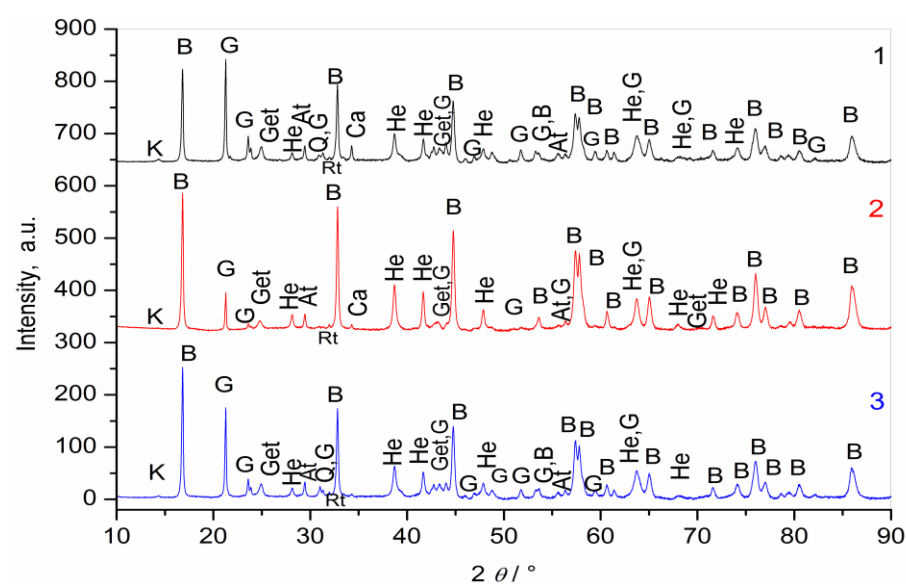


*Figure 2. Diffractogram of the bauxite samples Posušje (1-3): B-boehmite, G-gibbsite, He-hematite, Get-goethite, At-anatase, Rt-rutile, Ca-calcite, K-kaolinite and Q-quartz*
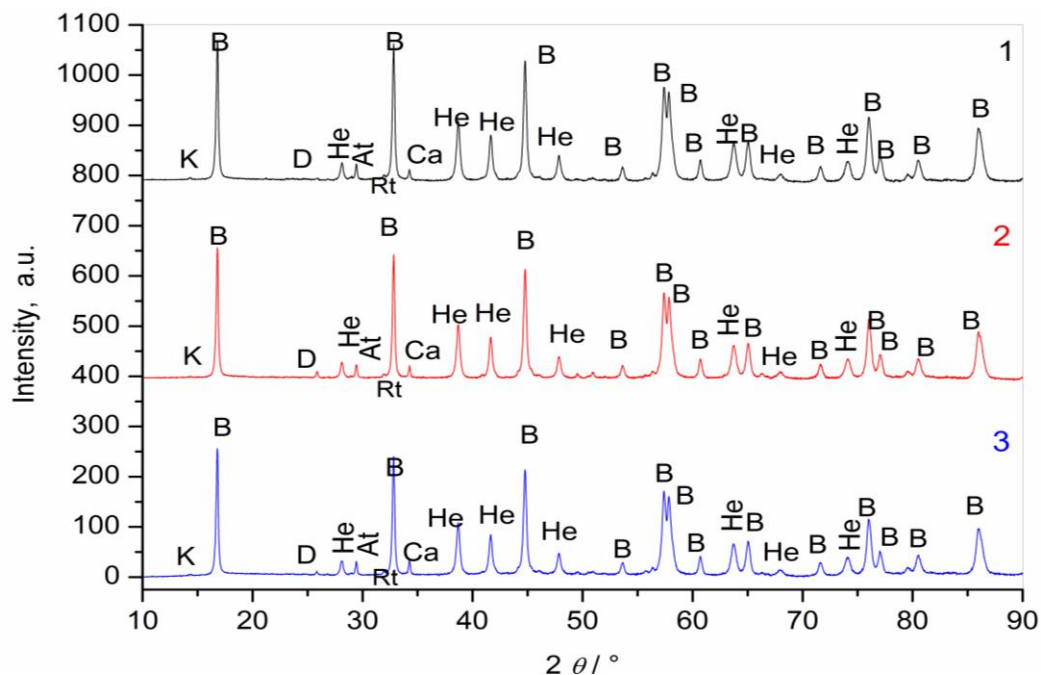
*Figure 3. Diffractogram of the bauxite samples Jajce (1-3): B-boehmite, He-hematite, At-anatase, Rt-rutile, Ca-calcite, K-kaolinite and D-diaspore*
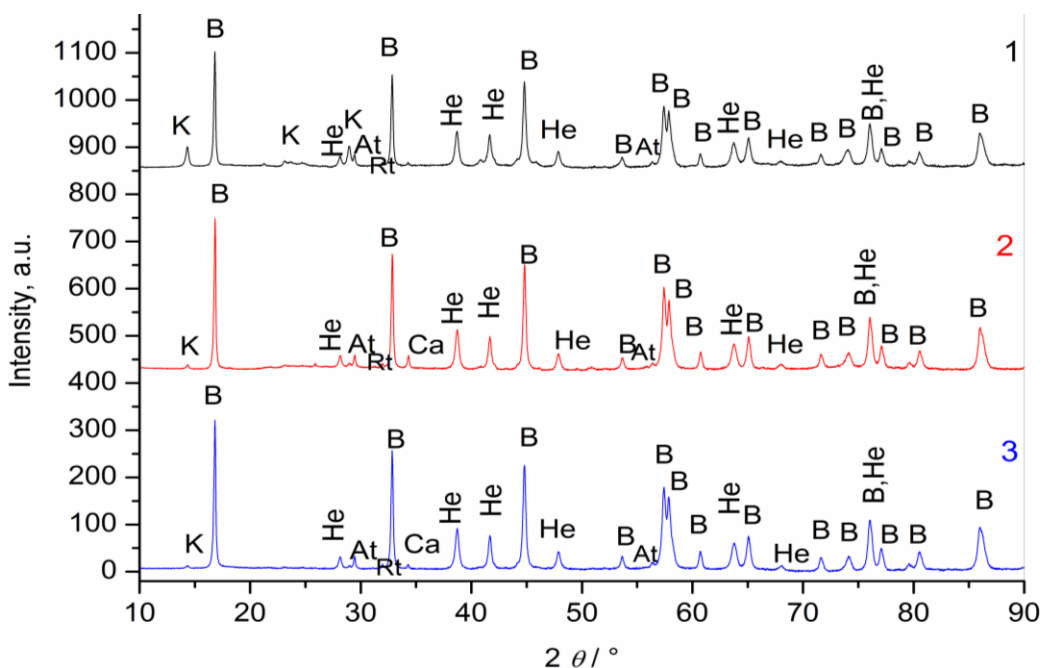


*Figure 4. Diffractogram of the bauxite samples Nikšić (1-3): B-boehmite, He-hematite, At-anatase, Rt-rutile, Ca-calcite and K-kaolinite*

Calibration curve for the ICP-OES analysis was constructed using eight points in the range of 0-80 mg dm$^{-3}$ Si by a serial dilution of the standard solution with ultrapure water to the desired concentrations, with three measurements for each concentration level. According to the literature data [17], a line of wavelength 288.158 nm is recommended for the determination of silicon by this method. In this paper, three Si wavelengths were observed simultaneously: 212.412, 251.612 and 288.158 nm, as it was also reported in literature [18]. For further processing of the results, a wavelength of 251.612 nm was used because it is the most sensitive line with a BEC (*Background Equivalent Concentration*) value of 0.645 mg dm$^{-3}$, as compared with 0.865 mg dm$^{-3}$ on 212.412 nm and 1.15 g dm$^{-3}$ on 288.15 nm, Table 1.
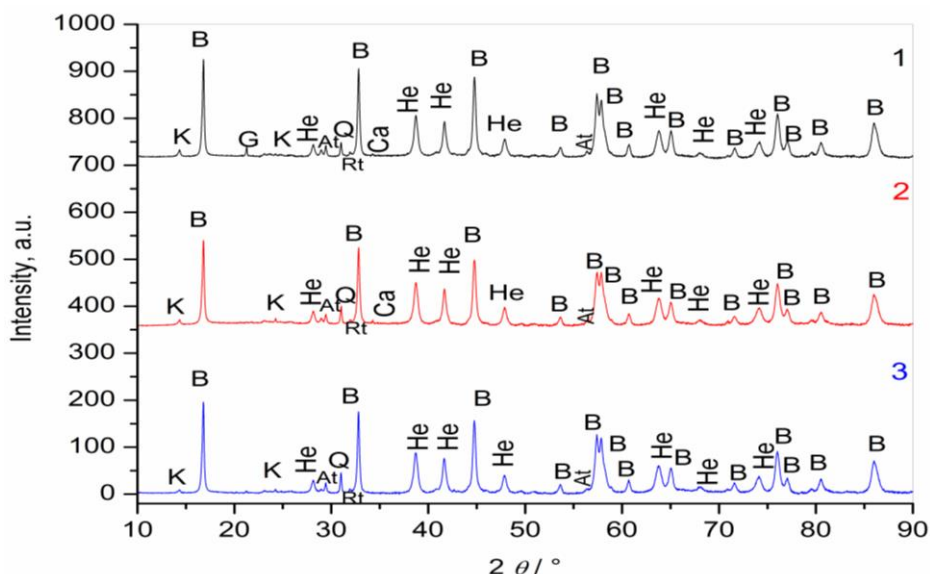
Figure 5.  Diffractogram of the bauxite samples Srebrenica (1-3): B-boehmite, He-hematite, At-anatase, Rt-rutile, Ca-calcite, Q-quartz, K-kaolinite and G-gibbsite
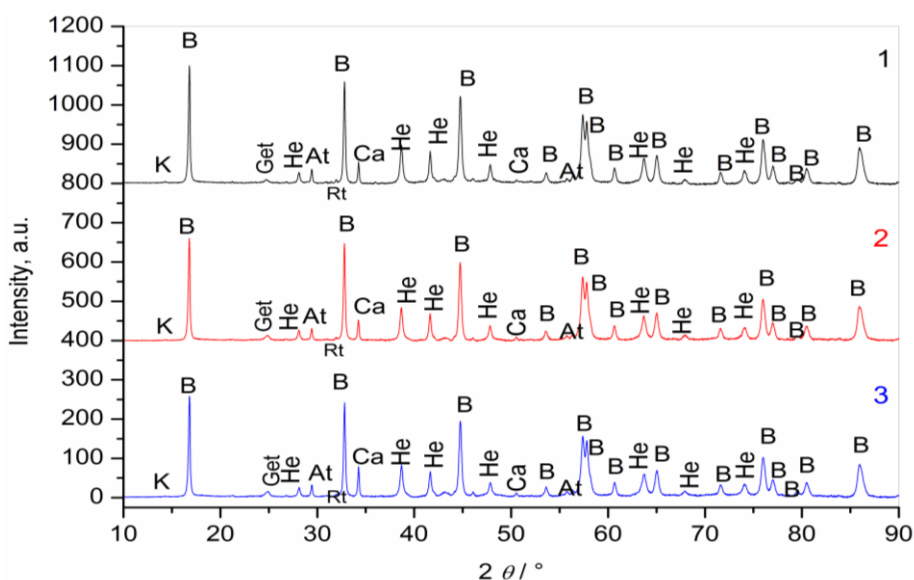


Figure 6. Diffractogram of the bauxite samples Široki Brijeg (1-3): B-boehmite, He-hematite, At-anatase, Rt-rutile, Ca-calcite, K-kaolinite, G-gibbsite and Get-goethite

Table 1. Calibration data of silicon emission lines determined by regression analysis. Correlation coeficient is 1 for all lines.

| Si wavelength line, nm | LOD[a], mg dm$^{-3}$ | BEC, mg dm$^{-3}$ | Standard error, mg dm$^{-3}$ | Detection range, mg dm$^{-3}$ |
|---|---|---|---|---|
| 212.412 | 0.0136 | 0.865 | 0.0788 | 0.0136-96 |
| 251.612 | 0.00168 | 0.645 | 0.0592 | 0.00168-96 |
| 288.158 | 0.0221 | 1.15 | 0.0765 | 0.0221-96 |

[a]LOD - limit of detection

For verification of calibration, a solution of silicon concentration of 20 mg dm$^{-3}$ with a tolerance of ± 10 % to the expected value was used as an ICV (*Initial verification calibration*) control sample [11,19], Figure 8. Bauxite NIST 697 was analysed with each series of samples as a laboratory control sample (LCS) [11,19] and the measurement results are shown in Figure 9.

*Figure 7. Diffractogram of the bauxite samples Mrkonjić Grad (1-2) and bauxite standard reference material NIST 697: B-boehmite, G-gibbsite, He-hematite, At-anatase, Rt-rutile, Ca-calcite, K-kaolinite and Get-goethite*



*Figure 8. Recovery of Si concentration in ICV control sample (concentration 20 mg dm⁻³ Si) according to the reference value (acceptance recovery criteria: 90-110 %)* [11]

*Figure 9. Percentage recovery of SiO₂ concentration in LCS control sample. Bauxite standard NIST 697 measured as a Laboratory Control Sample (LCS) during the period of measuring samples, acceptance recovery criteria: 80-120 %* [11]

The silicon dioxide content determined by ICP-OES was calculated by multiplying the results (mg dm⁻³) with a conversion factor of 2.14 (SiO₂/Si) and a dilution factor. The results of ICP-OES silicon dioxide content determination in comparison with spectrophotometric methods are presented in Table 2. Each result is the average value of three samples (preparation and measurement), with an error in the form of one standard deviation. Bias and recovery values were calculated related to the spectrophotometric method.

The mean relative deviation (bias) of ICP-OES results compared to UV-VIS spectrophotometry results is 4.88 %, and the mean recovery value of ICP-OES results compared to spectrophotometric results is 97.83 % (from 85.56 to 107.04 %). The scatter-plot diagram shown in Figure 10 shows that there is a good and strong correlation between the results of the two methods: correlation coefficient, $R$ = 0.9993, determination coefficient $R^2$ = 0.9987, $p$-value <0.0001. The relationship between the results of the two methods is defined by the direction equation: $c_{SiO_2 (ICP-OES)}$ =-0.1984 + 1.0647$c_{SiO_2(UV-VIS)}$.

The correlation of the results is not sufficient to conclude the comparability of the two methods [20]. Further comparison and evaluation are performed by applying the Bland Altman, Passing-Bablok, and "Mountain" plots [12-14],

as well as statistical tests. The Shapiro-Wilk test ($W$ = 0.92262, $P$ = 0.11764, $\alpha$ = 0.05) confirms the normal distribution of differences between the two methods, Figure 11, thus fulfilling the condition for the Bland Altman analysis.

*Table 2. Content of SiO$_2$ in bauxites from different deposits, determined by the ICP-OES method and compared to the results obtained by the spectrophotometric UV-VIS method*

| Bauxite sample | Concentration of SiO$_2$ ± SD, % | | Bias, % | Apsolute bias*, % | Recovery, % |
|---|---|---|---|---|---|
| | ICP-OES | UV-VIS | | | |
| Milići 1 | 4.74±0.066 | 4.75±0.057 | -0.01 | 0.21 | 99.79 |
| Milići 2 | 6.33±0.034 | 6.12±0.057 | 0.21 | 3.43 | 103.43 |
| Milići 3 | 6.49±0.089 | 6.36±0.184 | 0.13 | 2.04 | 102.04 |
| Posušje 1 | 1.79±0.003 | 1.95±0.042 | -0.16 | 8.21 | 91.79 |
| Posušje 2 | 0.75±0.004 | 0.85±0.078 | -0.10 | 11.76 | 88.24 |
| Posušje 3 | 2.46±0.043 | 2.59±0.085 | -0.13 | 5.02 | 94.98 |
| Jajce 1 | 1.67±0.022 | 1.92±0.106 | -0.25 | 13.02 | 86.98 |
| Jajce 2 | 1.25±0.014 | 1.24±0.071 | 0.01 | 0.81 | 100.81 |
| Jajce 3 | 1.54±0.017 | 1.80±0.198 | -0.26 | 14.44 | 85.56 |
| Nikšić 1 | 11.62±0.064 | 11.13±0.106 | 0.49 | 4.40 | 104.40 |
| Nikšić 2 | 3.28±0.052 | 3.20±0.156 | 0.08 | 2.50 | 102.50 |
| Nikšić 3 | 2.33±0.055 | 2.35±0.042 | -0.02 | 0.85 | 99.15 |
| Srebrenica 1 | 5.47±0.069 | 5.27±0.000 | 0.20 | 3.80 | 103.80 |
| Srebrenica 2 | 6.72±0.028 | 6.52±0.064 | 0.20 | 3.07 | 103.07 |
| Srebrenica 3 | 6.69±0.020 | 6.25±0.042 | 0.44 | 7.04 | 107.04 |
| Široki Brijeg 1 | 1.51±0.008 | 1.61±0.007 | -0.10 | 6.21 | 93.79 |
| Široki Brijeg 2 | 1.15±0.013 | 1.21±0.028 | -0.06 | 4.96 | 95.04 |
| Široki Brijeg 3 | 1.57±0.015 | 1.60±0.014 | -0.03 | 1.88 | 98.13 |
| Mrkonjić Grad 1 | 1.59±0.007 | 1.61±0.014 | -0.02 | 1.24 | 98.76 |
| Mrkonjić Grad 2 | 1.82±0.010 | 1.87±0.046 | -0.05 | 2.67 | 97.33 |
| Average | | | | 4.88 | 97.83 |
| Standard deviation | | | | 4.13 | 6.10 |

*[(Bias$_{ICP-OES}$– Bias$_{UV-VIS}$) / Bias$_{UV-VIS}$] 100
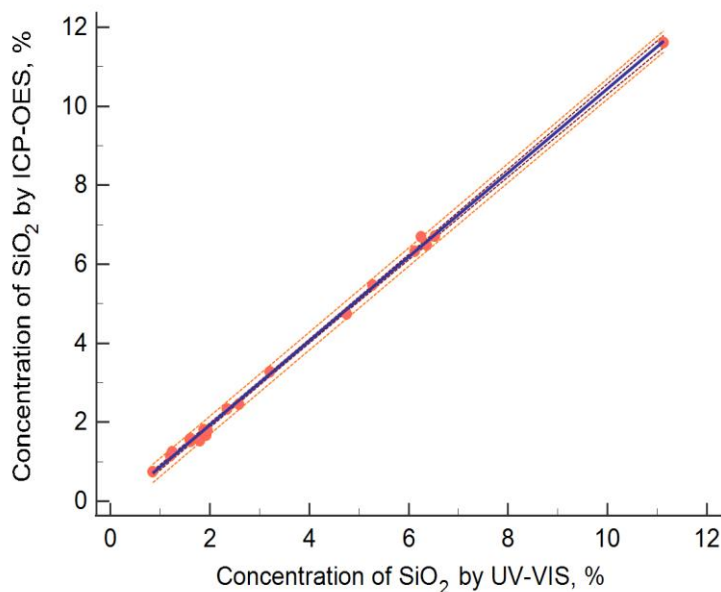


*Figure 10. Correlation results of ICP-OES and spectrophotometric method for determination of SiO$_2$ content in bauxite samples. The solid line represents regression direction and dashed lines represent the 95 % confidence interval*

The correlation of the results is not sufficient to conclude the comparability of the two methods [20]. Further comparison and evaluation are performed by applying the Bland Altman, Passing-Bablok, and "Mountain" plots [12-14], as well as statistical tests. The Shapiro-Wilk test ($W = 0.92262$, $P = 0.11764$, $\alpha = 0.05$) confirms the normal distribution of differences between the two methods, Figure 11, thus fulfilling the condition for the Bland Altman analysis.
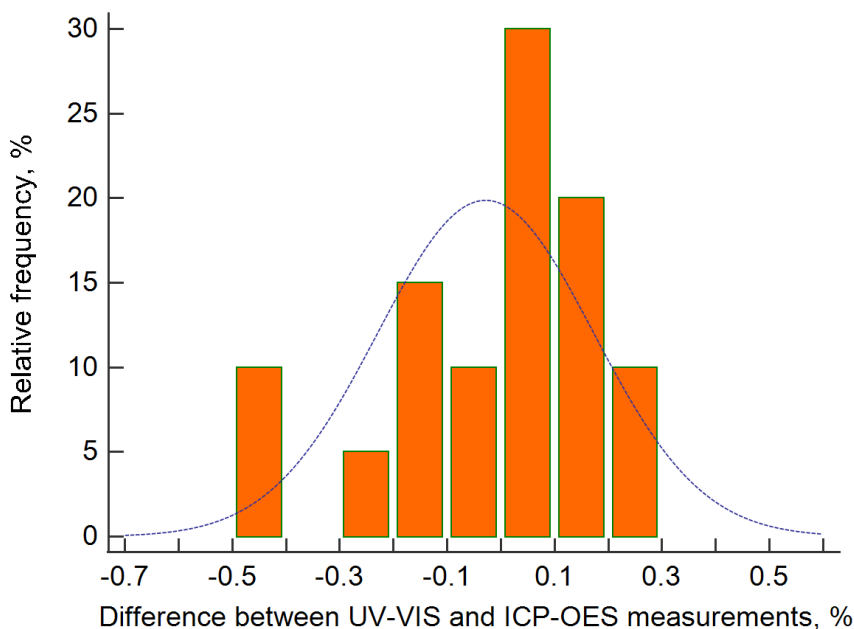


*Figure 11. Distribution plot of differences between measurements by ICP-OES and UV-VIS methods. The dotted line represents normal distribution. Shapiro-Wilk test for normal distribution accepted normality (W = 0.92262, P = 0.11764)*

By using the Bland Altman plot of the difference between the obtained measurements, it can be seen whether there is a difference in the measurements of the two methods in different concentration ranges, *i.e.* whether there is a constant or proportional difference in the measurements by a different method. The Bland Altman plot displayed in Figure 12 shows the difference between the measurement results of the two methods for determining $SiO_2$ in bauxite depending on the mean value of the measurement by the two methods for each sample. The solid center line represents the mean value of the difference measured by different methods for each sample (-0.03), with a 95 % confidence interval (CI) above and below the mean value line (CI from -0.1224 to 0.0654), while the dotted line represents the zero differences. The dashed lines represent the range of values or agreement limits ± 1.96 SD (from -0.42 to 0.36). Two points are outside these control limits. The regression direction of the measurement difference $y = 0.1946-0.0633x$ has a slightly negative slope depending on the mean value. This indicates that the differences decrease proportionally and move towards negative values with increasing $SiO_2$ concentration. The value of the zero difference is within the confidence interval of the mean value, based on which it can be concluded that the mentioned difference between the methods is not statistically significant.

A similar conclusion can be drawn from the analysis of Figure 13. This figure represents a Bland Altman graph comparing the relative differences of the two methods for determining $SiO_2$ in bauxite depending on the mean value. It is obvious that there is a proportional difference with a negative slope of the regression line, $y = 7.8642-1.5562 x$, and one point is outside the range of ± 1.96 SD (from -10.09 to 14.92). The value of the zero difference is within the confidence interval of the mean value, based on which it can be concluded that the mentioned difference between the methods is not statistically significant.

Figure 14 shows the results of the Passing-Bablok regression, where the relationship between the methods is given by the equation:

$$y = -0.157 \ (-0.2376-0.1066) + 1.058 \ (1.0374-1.0833) \ x \tag{1}$$
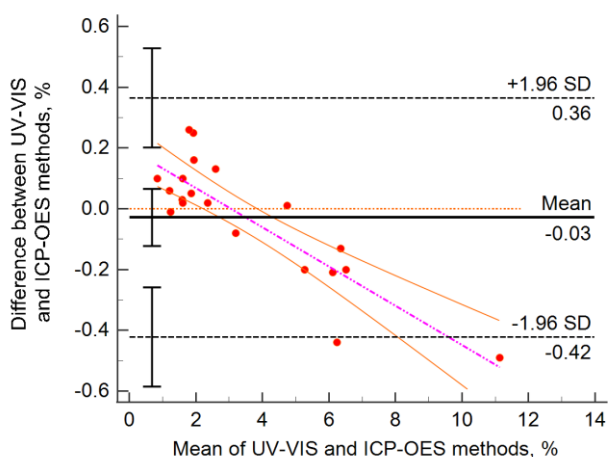
*Figure 12. Bland Altman plot of absolute differences between the results of two methods from Table 2. Dashed black lines represent limits of agreement from -1.96 SD to +1.96 SD. Dashed pink line represent direction equation y=0.1946-0.0633x, confidence interval limits are pre- sented as continuous line. Error bars with horizontal lines showa 95 % confidence interval of mean and limits agreement*
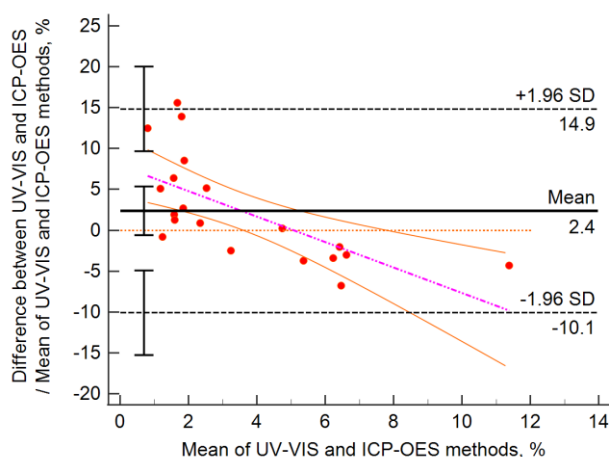
*Figure 13. Bland Altman plot of the relative differences between the results of two methods from Table 2. Dashed lines represent limits of agreement from -1.96 SD to +1.96 SD. Dashed pink line represent direction equation y=7.8642-1.5562x, confidence interval limits are pre- sented as continuous line. Error bars with horizontal lines showa 95 % confidence interval of mean and limits agreement*

The Cusum linearity test ($P$ = 0.36) shows that there is no significant deviation from linearity. To confirm the agreement between the two methods, the values 0 and 1 for the section on the ordinate and the slope of the direction must be within 95 % confidence intervals. If the zero is not within the 95 % confidence interval of intercept, there is a constant difference between methods. In the case that the value of 1 is not within the 95 % confidence interval for the slope confidence interval, there is a proportional deviation. In this paper, the 95 % confidence interval of the section does not contain zero, and the 95 % confidence interval of the slope does not include the value 1, which indicates the existence of slight systematic (constant) and proportional differences between ICP-OES and UV-VIS methods. The distribution of concentration differences between measurements of the two methods is additionally described by using the "Mountain" graph, Figure 15, where it is clear that the top of the graph is close to zero, indicating a good agreement between the results of the compared methods.
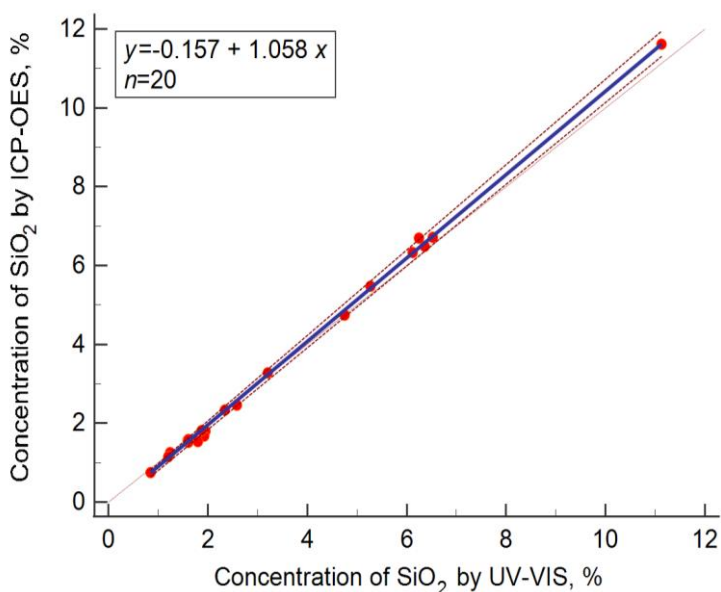


*Figure 14. Passing-Bablok regression. The solid line represents regression direction. Regression equation is expressed as y= -0.157+1.058 x. Reggresion line has a slope of 1.058 (1.0374 to 1.0833) and an intercept of -0.157 (-0.2376 to -0.1066). Dashed lines represent the 95 % confidence interval*
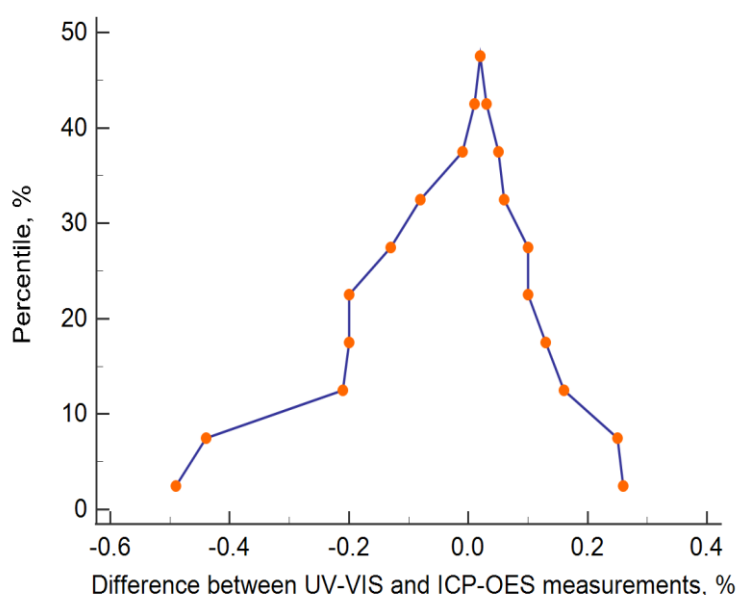
*Figure 15. "Mountain" plot of differences between the results of two methods from Table 2*

Further, a paired *t*-test was used to compare the mean values of the methods. The calculated value of the parameter *t* (0.635) is lower than *t* critical (2.093), so it can be concluded that there is no statistically significant difference between the mean values of the ICP-OES and UV-VIS methods, Table 3. As *F* is calculated (1.135) to be lower than the critical value of $F_{19,19}$ at $\alpha$ = 0.05 (2.12), it can be concluded that there is no statistically significant difference in the precision of the two methods when measuring routine bauxite samples.

*Table 3. t-test paired two samples for means of SiO₂ content measurement by UV-VIS and ICP-OES methods*

|  | ICP-OES | UV-VIS |
|---|---|---|
| Mean, % | 3.5385 | 3.51 |
| Variance | 8.091224 | 7.129052632 |
| Observations | 20 | 20 |
| Pearson correlation | 0.999352 |  |
| Hypothesized mean difference | 0 |  |
| df | 19 |  |
| *t*-stat | 0.635 |  |
| P(*T*<=*t*) one-tail | 0.266499 |  |
| *t* critical one-tail | 1.72913 |  |
| P(*T*<=*t*) two-tail | 0.53299 |  |
| *t* critical two-tail | 2.093024 |  |

In the next step, the accuracy assessment of the ICP-OES method was performed by successively measuring ten different samples (each time newly prepared) of the standard reference material, SRM NIST 697, Dominican bauxite, with a SiO₂ content of 6.81 ± 0.07 % [16]. Recovery values are in the range from 95.45 to 98.53 %. According to literature [21], the mean value of 96.51 % is slightly lower than the acceptance criteria of 97-103 %. Additionally, and according to [22], for this level of concentration this result is within the acceptability value of 95-102 %, Table 4. By using the *t-test*, it is determined that t calculated (11.499) is greater than *t* critical (2.262) for df-9, at $\alpha$= 0.05. At the same time, the mean value of ten measurements and the certified value differs significantly, which can be attributed to the effect of a systematic error of the ICP-OES analysis. The calculated value for the 95 % confidence interval (6.53-6.61 %) does not include the certified value of the standard bauxite sample. The measurement uncertainty calculated in relation to the SRM [12] is 0.082 %. On the other hand, compared to the reference method, t calculated (2.305) is slightly higher than t critical (2.262), so it can be concluded that there is a good correlation of SRM NIST 697 measurement results using both methods, as well as for measuring routine samples, Table 4.

*Table 4. Assessment of the accuracy of the ICP-OES method by using the standard reference material NIST 697*

| Number of measurements | ICP-OES | | UV-VIS | |
|---|---|---|---|---|
| | $C_{SiO_2}$ / % | Recovery, % | $C_{SiO_2}$ / % | Recovery, % |
| 1. | 6.71 | 98.53 | 6.46 | 94.86 |
| 2. | 6,.56 | 96.33 | 6.50 | 95.45 |
| 3. | 6.65 | 97.65 | 6.50 | 95.45 |
| 4. | 6.58 | 96.62 | 6.54 | 96.04 |
| 5. | 6.55 | 96.18 | 6.53 | 95.89 |
| 6. | 6.54 | 96.04 | 6.47 | 95.01 |
| 7. | 6.52 | 95.74 | 6.55 | 96.18 |
| 8. | 6.60 | 96.92 | 6.50 | 95.45 |
| 9. | 6.50 | 95.45 | 6.58 | 96.62 |
| 10 | 6.51 | 95.59 | 6.42 | 94.27 |
| Average | 6.57 | 96.51 | 6.51 | 95.52 |
| Standard deviation | 0.066 | 0.971 | 0.047 | 0.693 |
| RSD | 1.01 | 1.00 | 0.73 | 0.73 |
| *t*-calculated, SRM | 11.498 | | | |
| *t*-calculated, ref. method | | | 2.305 | |
| *t*-critical (df-9, $\alpha$-0,05) | 2.262 | | 2.262 | |
| 95 % confidence interval | | ±0.0409 (6.53 - 6.61 %) | | |
| Measurement uncertainty according to the certified value=0.082 % | | | | |

Table 5 shows the estimation of precision in repeatability. For this purpose, the solution of molten control bauxite samples SRM NIST 697 was measured in one day as follows: three repeated measurements during aspiration of the same solution, measuring the same sample ten times consecutively in the series and measuring the same sample several times in one day, every 30 min. Repeatability expressed as RSD is 0.48, 0.66, and 2.10 %, respectively.

*Table 5. Assessment of repeatability of the ICP-OES method by measuring NIST 697 samples*

| Measurement number | Concentration of SiO$_2$, % | | |
|---|---|---|---|
| | The same aspiration, measuring 3 times | Measurement in the series | Periodic measurement during day |
| 1. | 6.65 | 7.00 | 6.96 |
| 2. | 6.66 | 6.96 | 6.78 |
| 3. | 6.60 | 6.97 | 6.68 |
| 4. | | 7.02 | 6.55 |
| 5. | | 6.99 | 6.69 |
| 6. | | 6.94 | 6.89 |
| 7. | | 7.08 | 6.86 |
| 8. | | 7.01 | |
| 9. | | 6.92 | |
| 10. | | 7.02 | |
| Average | 6.64 | 6.99 | 6.77 |
| SD | 0.032 | 0.046 | 0.142 |
| RSD | 0.48 | 0.66 | 2.10 |
| Precision limit based on measurement in the series, *r*=2.8·SD=2.8·0.046 = 0.129 % | | | |

The precision of the method was checked against the Horwitz limit for intra-laboratory repeatability [21] for this concentration level, according to the equation (2):

$$PRSD_r = 2^{(1 - 0.5 \log C)} \qquad (2)$$

which has been modified as Equation (3):

$$RSD_r = 0.67 \, PRSD_r \qquad (3)$$

where: $PRSD_r$, % is the predicted relative standard deviation, *C* is the concentration expressed as mass fraction, RSDr is an acceptable limit for repeatability

The Horwitz's equation (2) represents an exponential relationship between the laboratory determined relative standard deviation (RSD) and concentration. This equation has emerged from sever al inter-laboratory studies conducted by the AOAC (American Association of Official Analytical Chemists). The Horwitz's PRSDr limit for SiO₂ concentration of

6.57 % is 3.01 %, while the modified value of the Horwitz's limit RSDr is 2.02 %. The repeatability in the series (RSD = 0.66 %) meets this criterion, and the RSD of periodic measurements during the day between analyses of other samples (2.10 %) differs slightly from the mentioned criterion. As a result, it can be concluded that the repeatability of the ICP-OES method is good. The repeatability of measurements of ten newly prepared samples of the same specimen (RSD = 1.01 %), Table 4, is within this criterion. The absolute difference between the two measurements in repeatability conditions (*r*) is 0.129 %, and according to the Horwitz's equation should not be greater than 0.372 %. Intermediate precision was determined by measuring one sample of SRM NIST 697 in a period of seven days (three times during each day), Table 6. In this period the calibration curve was not recalibrated, and different days of analyses were included as an additional factor of variability.

*Table 6. Intermediate precision by measuring NIST 697 samples during 7 days*

| Measurement number | Concentration of $SiO_2$, % | | | | | | |
|---|---|---|---|---|---|---|---|
| | 1. day | 2. day | 3. day | 4. day | 5. day | 6. day | 7. day |
| 1 | 6.90 | 7.05 | 6.65 | 6.42 | 6.49 | 6.79 | 6.70 |
| 2 | 6.73 | 6.99 | 6.72 | 6.42 | 6.79 | 6.48 | 6.67 |
| 3 | 6.71 | 7.49 | 6.46 | 6.42 | 6.39 | 6.39 | 6.92 |
| Average | 6.78 | 7.18 | 6.61 | 6.42 | 6.56 | 6.55 | 6.76 |
| Standard deviation | 0.104 | 0.273 | 0.135 | 0.000 | 0.208 | 0.210 | 0.137 |
| Average value of all measurements | | | | | | | 6.69 |
| Standard deviation | | | | | | | 0.275 |
| RSD | | | | | | | 4.11 |

Mean and relative standard deviations are calculated for each day. The total accuracy expressed as the value of RSD is 4.11 % and this value is about 50 % higher than the RSD measurements for one day, as well as the calculated predicted Horwitz's value of PRSDr [21]. In previous research [22-25], precision as RSD of <10 % and recovery of 90-110 % are generally considered satisfactory.

Intermediate precision was also observed over a longer period. During that time, the sample introduction system and torch were cleaned. The recalibration of the calibration curve was performed to the same standards. A control laboratory sample (LCS) NIST 697 was measured every day and the obtained results are presented in Table 7.

*Table 7. Intermediate precision after 19 days, torch and sample introduction system was cleaned*

| Measurement | I series-before cleaning | | II series-after cleaning | |
|---|---|---|---|---|
| | $c_{SiO_2}$ / % | Recovery, % | $c_{SiO_2}$ /% | Recovery, % |
| 1. | 6.26 | 92.00 | 6.46 | 94.81 |
| 2. | 6.20 | 91.04 | 6.08 | 89.23 |
| 3. | 6.20 | 91.04 | 5.94 | 87.22 |
| 4. | 6.49 | 95.37 | 6.43 | 94.49 |
| 5. | 6.49 | 95.31 | 6.23 | 91.44 |
| 6. | 6.27 | 92.01 | 6.10 | 89.61 |
| 7. | 6.59 | 96.97 | 6.27 | 92.09 |
| 8. | 6.41 | 94.05 | 6.51 | 95.61 |
| 9. | 6.53 | 95.94 | 7.35 | 107.90 |
| 10. | 6.86 | 100.72 | 6.81 | 99.93 |
| 11. | 7.23 | 106.20 | 5.71 | 83.78 |
| 12. | 7.31 | 107.30 | 5.97 | 87.71 |
| 13. | 6.99 | 102.71 | 6.26 | 91.88 |
| 14. | 7.05 | 103.57 | 6.02 | 88.41 |
| 15. | 6.65 | 97.68 | 7.10 | 104.30 |
| 16. | 6.66 | 97.86 | 7.13 | 104.71 |
| 17. | 6.53 | 95.89 | 5.40 | 79.27 |
| 18. | 6.27 | 92.01 | 5.59 | 82.06 |
| 19. | 6.35 | 93.31 | 5.39 | 79.17 |
| Average | 6.60 | 96.88 | 6.25 | 91.77 |
| Standard deviation | 0.343 | 5.041 | 0.559 | 8.216 |
| RSD | 5.20 | 5.20 | 8.94 | 8.95 |
| *t*-test: *t* calculated = 2.304, *t* critical = 2.042 | | | | |
| Anova single factor: *F* = 5.309, *F* critical = 4.113, *p*-value= 0.027 | | | | |

Recovery values are in the acceptable range, 80-120 %, except in two cases in the second series of measurements. Precision during the first 19 working days was 5.20 %, while it was 8.95 % during the next 19 days, after cleaning the instrument. Values of the paired *t*-test (*t* calculated > *t* critical) and the ANOVA test (*F* > *F* critical, *p*-value $< \alpha$ = 0.05) indicate that there is a statistically significant difference between the mean values and the precision of these two series of results. It can be concluded that RSD increases over time and that intermediate precision is deteriorating. The results are indicating that the ICP-OES method is sensitive to the variability of experimental measurement conditions (next working day, new argon bottle, memory effect, cleaning torch, and sample introduction system) [19], leading to random and systematic errors. This is implying that the determination of silicon dioxide by the ICP-OES method requires control of operating conditions, high purity of reagents, and measurement of a control sample, prepared according to the same procedure as the tested samples.

The errors of the reference method are not discussed in the paper. The fact that there is an agreement between the results of both methods, as well as the use of the same method of sample preparation, indicates the existence of several factors during the analysis that can be a source of errors in both methods.

## 4. CONCLUSION

The $SiO_2$ content in the analyzed bauxites, according to ICP-OES, ranges from 0.75 to 11.62 %. The emission line of 251.612 nm was selected for the determination of silicon dioxide by the ICP-OES method due to the lowest BEC values and standard error. Based on a graphical comparison of ICP-OES and UV-VIS results of bauxite analysis, there is a good correlation and comparability of analysis results of reference material and bauxite samples from different deposits. The values of the *t*-test and *F*–test indicate that there is no statistically significant difference in measurements by the two methods while the Passing-Bablok regression indicates slight differences between the methods. The value of the *t*-test shows that there is a statistically significant difference to the certified value of the NIST 697 standard, while the recovery values are in the acceptable range for a given concentration level. The repeatability of determination of the $SiO_2$ concentration in bauxite by the ICP-OES method, consecutively, in series (0.66 %) and over one day (2.10 %), is within the acceptable Horwitz's limit. RSD values that represent intermediate accuracy over 7 days (4.11 %), over a longer period of 19 days (5.2 %), and after instrument cleaning and measurement concerning the new calibration (8.94 %), are above the predicted RSDr limits but are still less than 10 %. The ICP-OES method shows greater sensitivity to experimental conditions and lower precision over time. Errors of the reference UV-VIS method are not considered and discussed in this paper. In the absence of another alternative method, the ICP-OES method can be applied with control of measurement conditions, system cleanliness, and measurement of the bauxite control sample (SRM or internal standard) with each group of unknown samples, with correction factor relative to the reference value.

## REFERENCES

[1]  McGuiness L, Nunes MD, Kroes F, Chai I. Automated analysis of bauxite exploration drill hole samples by diffuse reflectance Fourier transform infrared (FTIR) spectroscopy. In: *Proceedings of the 7th International Alumina Quality Workshop*. Australia, 2005; 187–192.

[2]  Authier-Martin M, Forte G, Ostap S, See J. The mineralogy of bauxite for producing smelter-grade alumina. *JOM* 2001; *53*(12):36–40. https://doi.org/10.1007/s11837-001-0011-1

[3]  Nechitailov A P, Suss AG, Zhilina TI, Belanova E A. New method of analyzing bauxites to determine their main components and impurities. *Metallurgist* 2008; 52(11): 625–632. https://doi.org/10.1007/s11015-009-9104-9

[4]  Blagojevic D, Lazic D, Keselj D, Skundrić B, Dugic P, Ostojic G. Determining the content of silicon dioxide in bauxites using X-ray fluorescence spectrometry. *Iran. J. Chem. Chem. Eng* 2019; 38(4). https://doi.org/10.30492/IJCCE.2019.34231

[5]  Ostojic G, Lazic D, Zeljkovic S. Determination of the iron oxide content in bauxite: comparing ICP-OES with UV-VIS and volumetric analysis. *Chem. Pap.* 2020; 75(1): 389-396. https://doi.org/10.1007/s11696-020-01305-z

[6]  Idris N, Lahna K, Syamsuddin F, Ramli M. Study on Emission Spectral Lines of Iron, Fe in LaserInduced Breakdown Spectroscopy (LIBS) on Soil Samples. *J. Phys. Conf. Ser* 2017; 846(012020). https://doi.org/10.1088/1742-6596/846/1/012020

[7]  Carvalho AAC, Alves VC, Silvestre DM, Leme FO, Oliveira PV, Nomura CS. Comparison of FusedGlass Beads and Pressed Powder Pellets for the Quantitative Measurement of Al, Fe, Si and Ti in Bauxite by Laser Induced Breakdown Spectrometry (LIBS). *Geostand*. *Geoanal. Res.* 2017; 41(4): 585–592. https://doi.org/https://doi.org/10.1111/ggr.12173

[8]    Fahad M, Sajjad A, Shah KH, Shahzad A, Abrar M. Quantitative elemental analysis of high silica bauxite using calibration-free laser-induced breakdown spectroscopy. *Appl. Opt.* 2019; 58(27): 7588-7596. /https://doi.org/https://doi.org/10.1364/AQ.58.007588

[9]    Upendra S, Mishra RS. Simultaneous multielemental analysis of alumina process samples using inductively coupled plasma spectrometry (ICP-AES*). Anal. Chem.: Indian J.* 2012; 11(1). https://www.tsijournals.com/articles/simultanious-multielemental-analysis-of-alumina-process-samples-using-inductively-coupled-plasma-spectrometry.pdf

[10]   Murray RW, Miller DJ, Krys KA. Analysis of major and trace elements in rocks, sediments, and interstitial waters by inductively coupled plasma-atomic emission spectrometry (ICP-AES). *ODP Tech. Note*, 2000; 29. https://doi.org/10.2973/ODP.TN.29.2000

[11]   Spectro Analytical Instruments GmbH. Smart Analyzer Vision vers. 5.01.09XX; 01. 10. 2012.

[12]   Giavarina D. Understanding Bland Altman analysis. *Biochem. Medica* 2015; *25*(2), 141–151. https://doi.org/10.11613/BM.2015.015

[13]   Bilić-Zulle L. Comparison of methods: Passing and Bablok regression. *Biochem. Medica* 2011; 21 (1): 49–52. https://doi.org/10.11613/bm.2011.010

[14]   Medcalc manual, https://www.medcalc.org/manual/mountain-plot.php, Accessed May 23rd 2020

[15]   Linsinger T. Comparison of a measurement result with the certified value. Application Note 1, European Reference Materials. 2010; 1–2.

[16]   Certificate of Analysis, Standard Reference Material 697, bauxite Dominican, National Institute of Standards and Technology. 1991

[17]   Liberatore PA. Determination of Majors in Geological Samples by ICP-OES*:* Vol. ICP-AES Inst. 1993; 12 https://www.colby.edu/chemistry/CH332/laboratory/Geo-ICP-protocol2.pdf

[18]   Hauptkorn S, Pavel J, Seltner H. Determination of silicon in biological samples by ICP-OES after non-oxidative decomposition under alkaline conditions. *Fresenius. J. Anal. Chem* 2001; 370**:** 246–250. https://doi.org/10.1007/s002160100759

[19]   US. EPA Method 6010D (SW-846): Inductively coupled plasma-atomic emission spectrometry. Washington, DC, USA, 2014. https://www.epa.gov/esam/epa-method-6010d-sw-846-inductively-coupled-plasma-atomic-emission-spectrometry

[20]   Simundic AM. Statistical analysis in method comparison studies-Part one. 2016; www.acutecaretesting.org

[21]   AOAC (American Association Of Official Analytical Chemists), *Appendix F : Guidelines for Standard Method Performance Requirements.* 2016. https://www.aoac.org/resources/guidelines-for-standard-method-performance-requirements/

[22]   Taftazani A, Roto R, Ananda NR, Murniasih S. Comparison of NAA XRF and ICP-OES Methods on Analysis of Heavy Metals in Coals and Combustion Residues. *Indones. J. Chem.* 2017; 17(2): 228–237. https://doi.org/10.22146/ijc.17686

[23]   Rüdel H, Kösters J, Schörmann J. *Determination of the Elemental Content of Environment Sample using ICP-OES, Guidelines for Chemical Analysis*, Fraunhofer Institute for Molecular Biology and Applied Ecology, Schmallenberg, 2007. https://www.ime.fraunhofer.de/content/dam/ime/en/documents/AE/SOP_ICP-OES_en.pdf

[24]   Amorin A, *Determination of major and minor elements in HF-digested soil samples using an Agilent 5110 ICP-OES*, application note, Agilent Technologies.Inc. 2019. https://www.agilent.com/cs/library/applications/application_inert_sample_chamber_icp-oes_5110_5994-1213en_us_agilent.pdf

[25]   Krishna AK, Murthy NN, Govil PK. Multielement Analysis of Soils by Wavelength-Dispersive X-ray Fluorescence Spectrometry. *At.* Spectrosc 2007; 28(6): 202–214. https://www.researchgate.net/profile/Keshav-Krishna/publication/233786687_Multielement_Analysis_of_Soils_by_Wavelength-Dispersive_X-ray_Fluorescence_Spectrometry/links/57ecd91a08aebb1961ffc510/Multielement-Analysis-of-Soils-by-Wavelength-Dispersive-X-ray-Fluorescence-Spectrometry.pdf

# Određivanje sadržaja silicijum-dioksida u boksitu: poređenje metode ICP-OES sa metodom UV-VIS

**Gordana S. Ostojić[1], Dragica Z. Lazić[2] i Saša M. Zeljković[3]**

[1]*Fabrika glinice ⬜Alumina⬜, Karakaj bb, 75 400 Zvornik, Bosna i Hercegovina*
[2]*Univerzitet u Istočnom Sarajevu, Tehnološki fakultet Zvornik, Karakaj bb, 75 400 Zvornik, Bosna i Hercegovina*
[3]*Univerzitet u Banjoj Luci, Prirodno matematički fakultet, SP Hemija, Mladena Stojanovića 2, 78 000 Banja Luka, Bosna i Hercegovina*

(Naučni rad)

*Izvod*

U ovom radu metoda optičke emisione spektrometrije sa induktivno spregnutom plazmom (engl. inductively coupled plasma - optical emission spectrometry, ICP-OES) korištena je za određivanje sadržaja silicijum-dioksida u boksitu, kao važne primese koja utiče na kvalitet i primenu boksita u proizvodnji glinice po Bajerovom (Bayer) postupku. Analizirano je dvadeset uzoraka boksita iz sedam različitih ležišta. Rezultati su upoređivani sa referentnom metodom UV-vidljive spektroskopije. Srednja relativna razlika između sadržaja silicijum-dioksida određenog pomoću ICP-OES metode i referentne metode je 4.88 %. Za procenu usporedivosti metoda korišteni su statistički testovi, zatim grafikon raspršenosti (engl. scatter plot), te Bland - Altman, „Passing-Bablok" i "Mountain" grafikoni. Grafičke komparacije uglavnom ne pokazuju statistički značajne razlike između metoda. Tačnost i preciznost ICP-OES metode proverena je pomoću standardnog referentnog materijala SRM NIST 697, boksit Dominikan. Vrednosti iskorištenja (engl. recovery) i ponovljivost, izražena kao relativna standardna devijacija (RSD), su u okviru kriterijuma prihvatljivosti. Na snovu t-testa postoji statistički značajna razlika između srednje vrednosti ICP-OES merenja i sertifikovane vrednosti sadržaja silicijum-dioksida, što se može pripisati efektu sistematske greške ICP-OES analize.

# Шеме испитивања оспособљености лабораторија у организацији СХИ Србије - обележавање Светског дана вода, 22. марта 2022. године

**Ненад Костић**[1] **и Марија Ракићевић**[2]

*[1]Завод за јавно здравље Крушевац, Србија*
*[2]Завод за јавно здравље Чачак, Србија*

*Извод*

Савез хемијских инжењера Србије је 22. марта 2022. године у Крушевцу организовао 11. шему испитивања оспособљености лабораторија. Овом стручном скупу одазвале су се 33 лабораторије за испитивање вода из целог региона, са преко 100 стручњака из области вода. Овај дан се обележава као Светски дан вода, а у доба пандемије Ковид-19 били смо једни од ретких који су на овом нивоу желели да подсете на овај дан. Домаћин скупа је био ЈП Водовод Крушевац са својом Фабриком воде у Мајдеву, постројењем недалеко од Крушевца, крај језера Ћелије, одакле се град и околне општине снабдевају водом за пиће. Ово предузеће се последњих година убрзано развија и шири своју дистрибутивну мрежу. Учесници су оценили шему испитивања оспособљености као одличну и као једну од ретких прилика да се упознају са колегама и размене искуства у лабораторијским праксама. Локални медији, као и екипа Радио телевизије Србије. пропратили су овај догађај и о њему известили у својим информативним емисијама (https://krusevacgrad.rs/57157-2/)

*Кључне речи:* узорковања воде; адекватни транспорт узорака; испитивања параметара квалитета воде; ISO 5667 .

*Available on-line at the Journal web address: http://www.ache.org.rs/HI/*

Савез хемијских инжењера (СХИ) Србије од 2017. године организује шеме испитивања оспособљености лабораторија, под називом *PT Sampling SHI*, за област узорковања вода ради хемијског испитивања. Ови стручни скупови су организовани већ 11 пута у више градова Србије:

1. Ниш, март 2017. Вода за пиће;
2. Нови Београд, јун 2017. река Сава;
3. Ниш, Студена, мај 2018. изворска вода из постројења НИВОС;
4. Београд, јул 2018. река Дунав
5. Горњи Милановац, септембар 2018. отпадна вода;
6. Атомска бања, мај 2019. изворска вода;
7. Међуврше, октобар 2019. језерска вода;
8. Нови Београд, мај 2020. река Сава;
9. Крушевац, мај 2021. отпадна вода;
10. Београд, септембар 2021. река Сава;
11. Крушевац, март 2022. вода за пиће;

У ових 11 шема, учествовале су лабораторије из Северне Македоније, Црне Горе, Босне и Херцеговине и Србије. Ово су били једини скупови у региону, који су окупили на истом месту и са истим циљем, како приватне тако и државне лабораторије које се баве испитивањима вода.

Главни циљ ових шема испитивања оспособљености је потврда компетентности лабораторија за процес који се састоји из:

- правилног узорковања воде,
- адекватног транспорта и
- испитивања одабраних параметара.

*Уводно предавање током шеме испитивања оспособљености лабораторија, под називом PT Sampling SHI 11. организованог у Крушевцу 22. марта 2022. године, на Светски дан вода*

Познато је да ни најбоља лабораторијска анализа не може да исправи грешке начињене приликом узорковања, тј. резултат испитивања не може бити бољи од узорка на коме је испитивање изведено.

Методе узорковања прописане су, стандардизоване су и опште прихваћене. Дате су у стандардима у серији ISO 5667, у форми захтева које лабораторије морају да испуне у погледу обучености особља, техничких захтева и записа који се морају водити. Такође, стандарди прописују и под којим се условима узорковани узорци вода морају транспортовати и у ком временском року до лабораторија, до почетка испитивања.

Велики значај ових скупова је и у томе што особље лабораторија током узорковања, гледа и међусобно размењује искуства о сопственим процедурама узорковања, опремом за узорковања и мерења на терену и сличним темама. То је и можда најинтересантнији део дана. Лабораторије једна по једна врше узорковање и мерења оних својстава која су могуће испитати на самом мерном месту, као што су pH воде, резидуални хлор, растворни кисеоник... Лабораторије користе опрему од различитих произвођача, коју калибришу својим пуферима и референтним стандардима. Ово изводе док их колеге из других лабораторија гледају, често и запитају о карактеристикама опреме и техникама мерења. Део дана, који личи на презентацију опреме и демонстрацију методе, чак и личних вештина које показују аналитичари, умногоме води ка могућностима у побољшавању процеса свих лабораторија.

Током ових 5-6 година и понављања шема узорковања вода и мерењима, уочена су значајна побољшања у лабораторијском раду на терену. Та побољшања се одсликавају у мањим међулабораторијским стандардним девијацијама резултата мерења лабораторија. Ово значи да су резултати лабораторија све приближнији једни другима, тј. да су све мање разлике између лабораторијских резултата.

Ове стандардне девијације зависе од следећих чинилаца и сваки од њих има свој већи или мањи удео:
- временске разлике узорковања и мерења међу лабораторијама,
- доприноса стандардне несигурности од природе тест материјала,
- доприноса стандардне несигурности од хомогености,
- доприноса стандардне несигурности од транспорта,
- доприноса стандардне несигурности од стабилности тест материјала и
- доприноса стандардне несигурности од методе/технике испитивања.

*Припрема опреме за узорковање пијаће воде из фабрике воде Мајдево у Крушевцу једне од лабораторија, током шеме испитивања оспособљености лабораторија коју је организовао Савез хемијских инжењера Србије на Светски дан вода 22. марта 2022. године*

Параметри који су се међулабораторијски поредили у ових 11 шема били су:
- температура амбијента и температура воде,
- pH вредност, мерена на терену и поново у лабораторијама,
- концентрација слободног резидуалног хлора,
- електропроводљивост, мерена на терену и поново у лабораторијама,
- концентрације нитрата и укупног азота
- концентрације хлорида и сулфата
- концентрације растворних фосфата и укупног фосфора,
- концентрације растворног кисеоника мерене на терену и у лабораторијама,
- хемијска потрошња кисеоника (ХПК) и биолошка потрошња кисеоника (БПК5)
- мутноћа,
- утрошак KMnO4
- концентрација суспендованих материја,
- алкалитет и концентрација бикарбоната
- концентрације калијума, натријума, магнезијума и калцијума и укупна тврдоћа

**Повратне информације**

Све лабораторије су изразиле веома позитивна мишљења о скуповима на којима се демонстрирају и нумерички и графички вреднују њихови резултати мерења. Извештаји о међулабораторијским поређењима лабораторијама служе у следећем кораку као потврда њихове компетентности приликом акредитације лабораторије. Акредитациона тела (Акредитационо тело Србије (АТС), Институт за акредитирање Босне и

Херцеговине (БАТА), Институт за акредитацију Републике Северне Македоније (ИАРСМ) и Акредитационо тело Црне Горе (АТЦГ)) их прихватају као меродавна, а усаглашеност лабораторијских резултата им обезбеђује додатни доказ о компетенцијама за овлашћења код ресорних министарстава.

Такође, више лабораторија нам се похвалило, како је на тендеру добило значајне уговоре, захваљујући доказима о својим тачним мерењима, који су дати у Извештају о међулабораторијским поређењима.

Сами учесници су више пута изразили своја задовољства што су били тог дана ван својих рутинских послова у својим лабораторијама. За неке од њих, ово су једини скупови, на којима се могу сусрести са својим колегама и разменити искуства. Није реткост да своје слике са ових догађаја постављају и на друштвеним мрежама, уз коментаре о честиткама организатору.



*Узорковање пијаће воде из фабрике воде Мајдево у Крушевцу, током шеме испитивања оспособљености лабораторија коју је организовао Савез хемијских инжењера Србије на Светски дан вода, 22. марта 2022. године.*

Најскорије одржана шема испитивања оспособљености лабораторија коју је организовао СХИ Србије била је 22. марта 2022. године, у Крушевцу. Овом стручном скупу одазвале су се 33 лабораторије за испитивање вода из целог региона, са преко 100 стручњака из области вода. Овај дан се обележава као Светски дан вода, а у доба пандемије Ковид-19 били смо једни од ретких који су на овом нивоу желели да подсете на овај дан.

Домаћин скупа је био ЈП Водовод Крушевац са својом Фабриком воде у Мајдеву, постројењем недалеко од Крушевца, крај језера Ћелије, одакле се град и околне општине снабдевају водом за пиће. Ово предузеће се последњих година убрзано развија и шири своју дистрибутивну мрежу. Нарочито су поносни на своје постројење за прераду отпадних и комуналних вода, које се прикупљају из целог града и пречишћавају пре улива у Западну Мораву. Локални медији, као и екипа Радио телевизија Србије, пропратили су овај догађај и о њему известили у својим информативним емисијама (https://www.youtube.com/watch?v=p75a_VF5CKU)

На крају, овакав одзив лабораторија и експерета на овом догађају у Крушевцу, потврда нам је да организација ових скупова представља значајан допринос побољшавању лабораторијских услуга у домену испитивања вода у региону.

# PT schemes organized by the Association of Chemical Engineers of Serbia - Acknowledging the World Water Day on March 22, 2022

**Nenad Kostić[1] and Marija Rakićević[2]**

[1]*Institute of Public Health Kruševac, Serbia*
[2]*Institute of Public Health Čačak, Serbia*

*Abstract*
The Association of the Chemical Engineers of Serbia has organized the 11th proficiency testing (PT) scheme for laboratories on March 22, 2022, in Kruševac, in which 33 laboratories from the region took part with more than 100 experts in water quality analysis. March 22 is celebrated each year as the World Water Day and in the present time of COVID-19 pandemic the scheme was one of the rare events that aimed to draw attention to this important day. The host was the Public Utility Company "Vodovod-Kruševac" and its water factory in Majdevo near the city of Kruševac at the lake Ćelije, which supplies the city and the surroundings with drinking water. This company has been rapidly growing in recent years and expanding its distribution network. The participants rated the PT scheme as excellent and as one of the rare occasions for them to meet the colleagues and exchange experiences in laboratory practices. The event was covered by the local media and the Radio Television of Serbia.

*Keywords:* water sampling; adequate transport of samples; testing of water quality parameters; ISO 5667.

*Keywords:* water sampling; adequate transport of samples; testing of water quality parameters; ISO 5667.

129

**Izjava autora Pisma uredniku**
# Izazovi i dileme elektrohemijske konverzije i skladištenja energije

**Aleksandar Dekanski**

*Univerzitet u Beogradu, Institut za hemiju, tehnologiju i metalurgiju, Centar za elektrohemiju, Njegoševa 12, Beograd, Srbija*

Ovim putem želim da se javno izvinim kolegi i prijatelju dr Branimiru Grguru, profesoru Tehnološko-metalurškog fakulteta u Beogradu, zbog nesmotrenosti učinjene korišćenjem njegove slike kao ideje za izradi slike 2 u radu *Izazovi i dileme elektrohemijske konverzije i skladištenja energije*, objavljenom u volumenu 76, broju 1 (2022) ovog časopisa [1]. Imao sam privatan pristup njegovoj originalnoj slici, a nepažnjom se nisam informisao da je ta slika publikovana u monografiji pod nazivom *Alternativni izvori energije: principi konverzije i skladištenja*, koju je objavilo Inženjersko društvo za koroziju, Beograd, 2015, ISBN 978-86-91303-6-1, slika 3.1 na stranici 47 [2]. Time sam neetički propustio da naznačim autorstvo kolege Grgura za ovu sliku i da citiram navedenu monigrafiju.

Nakon što je dr Grgur redakciji časopisa skrenuo pažnju na moj propust i nakon što sam mu ja, uz izvinjenje, izneo da propust nije učinjen namerno, već mojom nepažnjim, kolega Grgur je imao puno razumevanje za moje obrazloženje propusta, na čemu sam mu izuzetno zahvalan.

Redakcija časopisa je odlučila da u ovom broju časopisa objavi Corrigendum [3], a da u Online verziji članka [1] izvrši neophodne izmene, kojima se naznačava da je slika 2 nastala modifikacijom originalne slike dr Grgura.

Aleksandar Dekanski

**REFERENCE**

[1] Dekanski A, Izazovi i dileme elektrohemijske konverzije i skladištenja energije, *Hem. Ind.* 2022;76(1):43-54. https://doi.org/10.2298/HEMIND220201002D

[2] Grgur B, *Alternativni izvori energije: principi konverzije i skladištenja*, Inženjersko društvo za koroziju, Beograd, 2015, ISBN 978-86-91303-6-1, 47

[3] Corrigendum, *Hem. Ind.* 2022; 76(2): 133. https://doi.org/10.2298/HEMIND220406006D

# Statement of the author of the Letter to Editor
# Challenges and doubts of electrochemical energy conversion and storage

**Aleksandar Dekanski**

*University of Belgrade, Institute of Chemistry, Technology and Metallurgy, Department of Electrochemistry, Njegoševa 12, Belgrade, Serbia*

I would like to publicly apologize to my colleague and friend Dr. Branimir Grgur, professor at the Faculty of Technology and Metallurgy in Belgrade, for the recklessness of using his Figure as an idea to create Figure 2 in the paper Challenges and dilemmas of electrochemical conversion and energy storage, published in volume 76, No. 1 (2022) of this journal [1]. I had a private approach to his original Figure, and I inadvertently did not inform that this figure was published in a monograph entitled *Alternative Energy Sources: Principles of Conversion and Storage*, published by the Corrosion Engineering Society, Belgrade, 2015, ISBN 978-86-91303 -6-1, Figure 3.1 on page 47 [2]. Thus, I unethically failed to indicate the authorship of my colleague Grgur for this Figure and to cite monograph.

After Dr. Grgur drew the attention of the Journal's Editorial Office to my mistake and after I apologized to him that the mistake was not made intentionally, but by my carelessness, my colleague Grgur had much understanding for my explanation of the mistake, for which I am extremely grateful.

The Editor of the journal decided to publish the Corrigendum in this issue of the journal [3], and to make the necessary changes in the Online version of the article [1], which indicate that Figure 2 was created by modifying the original image of Dr. Grgur.

Aleksandar Dekanski

**REFERENCE**

[1]  A, Challenges and doubts of electrochemical energy conversion and storage, *Hem. Ind.* 2022;76(1):43-54. https://doi.org/10.2298/HEMIND220201002D

[2]  Grgur B, *Alternativni izvori energije: principi konverzije i skladištenja*, Inženjersko društvo za koroziju, Beograd, 2015, ISBN 978-86-91303-6-1, 47 – in Serbian

[3]  Corrigendum, *Hem. Ind.* 2022;Articles in Press. https://doi.org/10.2298/HEMIND220406006D

# CORRIGENDUM

**U ČLANKU**

## Izazovi i dileme elektrohemijske konverzije i skladištenja energije

**Aleksandar Dekanski**

*Univerzitet u Beogradu, Institut za hemiju, tehnologiju i metalurgiju, Centar za elektrohemiju, Njegoševa 12, Beograd, Srbija*

**Samo štampana verzija**

*Dostupno na web stranici časipisa: http://www.ache.org.rs/HI/*

|  | Stoji | Treba da stoji |
|---|---|---|
| Stranica 48 Naslov Slike 2 | Održivo i za životnu sredinu optimalno korišćenje elektrohemijskih sistema za konverziju i skladištenje energije | Održivo i za životnu sredinu optimalno korišćenje elektrohemijskih sistema za konverziju i skladištenje energije (Slika je kreirana modifikacijom Slike 3.1 na strani 47 monografije B. Grgura: *Alternativni izvori energije: principi konverzije i skladištenja* [48]) |
| Page 48 Figure 2 caption | Sustainable and environmentally optimal use of electrochemical systems for energy conversion and storage | Sustainable and environmentally optimal use of electrochemical systems for energy conversion and storage (The figure was created by modifying Figure 3.1 on page 47 of B. Grgur's monograph: *Alternative energy sources: principles of conversion and storage* [48]) |
| Stranica 49 8 red odgore | …i/ili recikliranje [48]. | …i/ili recikliranje [49]. |
| Stranica 49 14 red odgore | …mnogih morskih vrsta [49]. | …mnogih morskih vrsta [50]. |
| Stranica 49 14 red odgore | …ogromne količine vode za hlađenje [50]. | …ogromne količine vode za hlađenje [51]. |

Stranica 51. Iza reference [47], dodaje se referenca:
[48] Grgur B, *Alternativni izvori energije: principi konverzije i skladištenja*, Inženjersko društvo za koroziju, Beograd, 2015, ISBN 978-86-91303-6-1, 47
Reference [48], [49] i [50] menjaju brojeve u [49], [50] i [51], respektivno.

Autor se izvinjava za grešku i sve eventualne nedoumice i neprijatnosti koje su time izazvane.
The author would like to apologize for the oversight and any inconvenience it may have caused.